

**Study of In-situ Intercalation of Organic Molecules
and Electrodeposition of Copper into
Transition Metal Dichalcogenides**
by
Scanning Probe Techniques



Dissertation
zur Erlangung des Doktorgrades
der Mathematisch-Naturwissenschaftlichen Fakultät
der Christian-Albrechts-Universität
zu Kiel

vorgelegt
von

Sujit Kumar Dora

Kiel 2008

Referent : Prof. Dr. O. M. Magnussen

Korreferent : Prof. Dr. R. Adlung

Tag der mündlichen Prüfung :

Zum Druck genehmigt :

Prof. Dr. J. Grotemeyer
Dekan

Contents

1	Introduction	1
2	Transition Metal Dichalcogenides	5
2.1	Crystal Structure	6
2.1.1	TiSe ₂	6
2.1.2	NbSe ₂	6
2.1.3	TaS ₂	7
3	Intercalation	10
3.1	Host	10
3.2	Guest	12
3.3	Product	13
3.4	Process	15
3.5	Electrochemical Intercalation	16
3.5.1	Thermodynamics of Electrochemical Intercalation	16
3.5.2	Specific Electrochemical Intercalation Methods	19
3.6	Previous In-situ High Resolution Microscopy Intercalation Studies	24
4	Electrodeposition	25
4.1	Basic Concepts of Electrodeposition	26
4.2	Thermodynamics of the Deposition Process	28
4.2.1	Nernst Equation	28
4.3	Electrode Kinetics	28
4.3.1	Electrochemical Double Layer	28
4.3.2	Overpotential Deposition and Butler-Volmer Equation	29
4.4	Mass Transport	29
4.5	Nucleation and Growth	30
4.6	Electrodeposition of Copper	33

5	Experimental Methods	34
5.1	Cyclic Voltammetry (CV)	34
5.2	In-situ Scanning Tunneling Microscopy (STM)	35
5.2.1	Tunneling Effect	36
5.2.2	Electrochemical Scanning Tunneling Microscopy (EC-STM)	38
5.3	Atomic Force Microscopy (AFM)	39
5.3.1	Modes of Operation for the AFM	40
5.4	Scanning Electron Microscope (SEM)	42
5.5	Experimental Conditions	43
5.5.1	Sample Surface Preparation	43
5.5.2	Preparation of Tunneling Tips, Electrolytes and Reference Electrode.	44
6	Results on organic molecule intercalation into TMDCs	48
6.1	1T-TaS ₂ in Air	48
6.2	1T-TaS ₂ in Pure H ₂ SO ₄	49
6.2.1	Literature Review	49
6.2.2	Cyclic Voltammetry	50
6.2.3	STM Study	51
6.3	Amine Intercalation in Transition Metal Dichalcogenides	54
6.3.1	Literature Review	54
6.3.2	Cyclic Voltammetry	58
6.3.3	STM Studies	61
6.3.3.1	TiSe ₂	61
6.3.3.2	NbSe ₂	61
6.3.3.3	TaS ₂	62
6.4	TaS ₂ in Pyridine at pH 3	68
6.4.1	Literature Review	68
6.4.1.1	Orientation of Intercalated Pyridine in TaS ₂	69
6.4.1.2	Bonding	70

6.4.2	Cyclic Voltammetry	71
6.4.3	STM Study	73
6.4.3.1	Surface Etching at Higher Tunneling Current	74
6.4.3.2	Intercalation of Pyridine in TaS ₂	75
6.4.3.3	Deintercalation	85
7	Summary on organic molecule intercalation into TaS₂	87
8	Results on Cu deposition onto TaS₂	89
8.1	Literature Review	89
8.2	Electrochemical Characterization of TaS ₂ in 0.01 M CuSO ₄ /H ₂ SO ₄ Electrolyte	91
8.3	Microscopic Characterization of TaS ₂ after Cu Deposition	96
8.3.1	Surface Topography of TaS ₂ for Lower Cu Coverage (10 ML)	96
8.3.2	Medium Surface Coverage (>20 ML)	97
8.3.3	Higher Surface Coverage (≥ 50 ML)	102
8.3.4	Potentiostatic Bulk Cu Deposition	104
8.3.5	Galvanostatic Deposition at Different Deposition Rates	107
8.4	Discussion	110
9	Summary on Cu deposition onto TaS₂	115
10	Conclusion	116

Abstract

Transition metal dichalcogenides (TMDCs) are ideal host materials for the intercalation of organic molecules, resulting in large change of structural (e.g. cracking, layer bending) and electronic properties (e.g. charge density wave, superconductivity). On the other hand metal deposition onto transition metal dichalcogenides under vacuum conditions has been shown to result in the formation of nanostructures (e.g. nanotunnels, nanowires) for a number of TMDCs. In this work, we have investigated the electrochemical intercalation / deintercalation of organic molecules (e.g. octylamine, pyridine) as well as the formation of different nanostructures by electrodeposition of Cu onto TaS₂. A number of surface science techniques e.g. cyclic voltammetry (CV), electrochemical scanning tunneling microscopy (EC-STM), atomic force microscopy (AFM) as well as scanning electron microscopy (SEM) were employed in our investigation.

The atomic-scale mechanisms of the electrochemical intercalation/deintercalation of octylamine and pyridine (both 0.01 M solution pH 3) in 1T - TaS₂ were investigated by in-situ electrochemical STM and cyclic voltammetry indicating a step flow etching at -0.44 V vs. SCE in both 0.01 M octylamine and pyridine electrolyte at pH 3. At potentials negative of -0.6 V, except for a step flow etching, no intercalation was observed for octylamine. Ex-situ measurement after keeping the sample at -0.75 V showed a step height increase of 0.5 nm indicating parallel orientation of octylamine within the TaS₂ layer. Pyridine intercalation into TaS₂ at potentials negative of -0.6 V, resulted a slow increase in step height from 0.6 nm to 0.9 nm indicating the parallel orientation (Phase I) of pyridine within van der Waals gap. For longer intercalation times a first-order phase transition to a phase with pyridine molecules arranged in perpendicular orientation (phase II) was found. Deintercalation of pyridine occurred by the accumulation of pyridine molecule within the TaS₂ layers at - 0.44 V followed by dissolution at 0.1 V. A step height decrease from 0.9 to 0.6 was also observed.

Electrochemical Cu deposition onto TaS₂ results in the formation of different nanostructures, in particular, networks of nanotunnels. The morphology of these wires and of the TaS₂ substrate was characterized as a function of coverage and deposition rate. These observations indicate characteristic differences to Cu nanotunnels formed by vacuum deposition and provide details on the growth process.

Abstract

Übergangsdichalcogenide (TMDCs) sind ideale Wirtsmaterialien für die Interkalation organischer Moleküle, was sowohl zu einer großen Änderung der strukturellen Eigenschaften (z.B. Verbiegen von Schichten, Rissbildung) als auch der elektronischen Eigenschaften (z.B. Ladungsdichtewellen, Supraleitung) führt. Andererseits ist unter Vakuumbedingungen gezeigt worden, dass Metallabscheidung für eine Reihe von Übergangsdichalcogeniden zur Bildung von Nanostrukturen führt (z.B. Nanotunnel, Nanodrähte). In dieser Arbeit wurde sowohl die elektrochemische Interkalation / Deinterkalation von organischen Molekülen (z.B. Octylamin, Pyridin) als auch die Bildung verschiedener Nanostrukturen durch electrochemischeabscheidung von Cu auf TaS₂ untersucht. Dabei wurde eine Reihe von verschiedenen Techniken wie Zyklovoltammetrie (CV), elektrochemische Rastertunnelmikroskopie (EC-STM), Rasterkraftmikroskopie (AFM) und Rasterelektronenmikroskopie (SEM) eingesetzt.

Die auf atomarer Ebene Mechanismen ablaufenden der elektrochemischen Interkalation / Deinterkalation von Octylamin und Pyridin (beide in 0,01 M Lösung, PH 3) in 1T - TaS₂, die mittels Zyklovoltammetrie und in-situ elektrochemischem STM untersucht wurden, zeigen eine Auflösung an stufen bei -0,44 V vs. SCE. Bei Potentialen unterhalb -0,6 V wurde abgesehen vom Schrittflussradierung bei Octylamin keine Interkalation beobachtet. Ex-situ Messungen, bei denen das Potential der Probe zuvor bei -0,75 V gehalten wurde, zeigten, da die Stufenhöhe sich um 0,5 nm erhöhte. Dies deutet auf eine parallele Orientierung des Octylamins innerhalb der TaS₂ Schicht hin. Im Gegensatz dazu führte die Interkalation von Pyridin in TaS₂ bei Potentialen unter -0,6 V zu einer langsam Erhöhung der Stufenhöhe von 0,6 nm auf 0,9 nm, was auf eine parallele Ausrichtung (Phase I) des Pyridin in der van der Waals Lücke hindeutet. Mit zunehmender Interkalationszeit erfolgt ein Phasenübergang 1. Ordnung zu einer Phase, in der die Moleküle senkrecht orientiert sind(Phase II). Die Deinterkalation des Pyridins beinhaltet die Agglomeration von Pyridinmolekülen innerhalb der TaS₂ Schicht bei -0,44 V auf, die eine Auflösung bei 0,1 V. folgte. Eine Erhöhung der Stufenhöhe bei der Erniedrigung von 0,9 auf 0,6 V wurde ebenfalls beobachtet.

Die elektrochemische Abscheidung von Cu auf TaS₂ führt zur Bildung verschiedener Nanostrukturen, speziell zu Netzwerken aus Nanotunneln. Diese Beobachtungen weisen charakteristische Unterschiede zu Nanodrähten auf, die unter Vakuumabscheidung gebildet wurden, und liefern Details über den Wachstumsprozess.

1 Introduction

The intercalation reaction has fascinated researchers of several areas (physics, chemistry, materials science etc.) over the past 40 years [1, 2]. It involves two species, one playing the role of the host (e.g. transition metal dichalcogenides), the other of the guest (e.g. metals, organic molecules). Typically host and guest interact weakly, and they give rise to a compound where they can still be considered as two distinct entities. In many cases, the amount of guest species in a host can be arbitrarily varied, so that the change to the environment of both host and guest can be controlled in a defined manner. Structural changes due to intercalation leads to the changes of physical properties for both the entities and also for the resulting complex (e.g. critical temperature of superconductivity) [1]. The properties of the intercalated materials can be fine tuned because the host can often be prepared in a wide range of compositions by intermixing of different related elements. Electrochemical techniques have advantages over conventional techniques (e.g. thermal methods), because they allow selective intercalation / deintercalation of the mobile species and a topotactic control of reaction. The degree of intercalation / deintercalation is precisely controlled by monitoring the charge and the measured cell voltage which ultimately gives hints on thermodynamic and kinetic features of the investigated system. By this way mixed valence compounds can be synthesised and changes in their properties can be observed.

Electrodeposition is an age old phenomena that has been recently applied towards the creation of nanostructures. In electrodeposition of metals, generally metal ions (M^+) are transferred from the solution to the metal lattice. The reaction is accompanied by transfer of 'z' electrons from an external electron source (e.g. power supply) to the electron gas in the metal M. The driving force for such processes is the potential difference between the electrodes in the electrochemical cell. Electrochemical deposition has proven to be a powerful and versatile tool for the formation of structures e.g nanowires, with lateral dimensions below 100 nm on planar substrates. Examples cover a broad range, starting from industrial applications, the arguably most important of which is Cu plating in ultrascale intergrated microchips (ULSI), to current research , where nanoscale templates (e.g. pores, nanoparticles, biological and supramolecular structures) are employed to create ordered patterns with dimensions down to a few nanometers [3].

Transition metal dichalcogenides (TMDCs) studied in this thesis, form a class of compounds known

for their layered structure. The term "layered" refers to the existence of parallel planes, where van der Waals interaction between the layers is much weaker in comparison to the interactions within a single layer. Such feature makes these materials highly anisotropic and two-dimensional (i.e. the physical properties associated with them are confined to 2 dimensions). A large variety of properties arise from this peculiarity, rendering TMDCs interesting not only from the theoretical point of view (e.g. charge density waves [4, 5], superconductivity [6, 7]), but also for various practical applications. Due to their low shear resistance TMDCs are used as solid-state lubricants [8, 9]. TMDCs can readily exhibit saturated, chemically inert surfaces, which are an ideal substrate for surface science studies. Tributsch and coworkers demonstrated in 1977 that highly efficient and relatively stable photoelectrochemical cells can be based on TMDCs [10]. Due to the reactivity of the plane edges TMDCs proved to be very efficient in heterogeneous catalysis. MoS₂ hydrodesulfurization catalysis is one of the most widely used catalytic systems worldwide [11]. Recently, there has been renewed interest in such two dimensional materials after the discovery of graphene in which charge carriers can travel thousands of interatomic distances without scattering [12]. From the large family of TMDCs, three materials i.e. TiSe₂, NbSe₂ and TaS₂ were chosen for our study. However, experimental difficulties associated with TiSe₂ (surface oxidation in organic electrolyte) and NbSe₂ (small crystal size) prevented further work with these crystals. Therefore, most of the studies of organic molecules (pyridine, octylamine) intercalation and electrodeposition of Cu in this thesis only focussed on TaS₂ single crystals.

In the last two decades the significant improvements of scientific equipment for the investigation of solid structures has brought about decisive factors to the understanding and development of new materials. Several diffraction techniques have been applied to determine atomic arrangements of guests inside the host with great accuracy. These techniques also focussed on the structure and phase behavior as well as the remarkable physical properties (e.g. superconductivity) of the bulk compounds. However, the effect of intercalation on the nanometer scale surface structure has largely not been studied up to now. In particular, high-resolution in situ studies of electrochemical intercalation processes in TMDCs have not been reported, apart from an atomic force microscopy study in air, where nanostructuring by local electrochemical metal intercalation/deintercalation via the electric field of a conducting tip was demonstrated [12]. Even for other layered materials only a few in situ studies of electrochemical intercalation

by surface sensitive techniques, such as scanning tunneling (STM) or atomic force (AFM) microscopy, have been reported up to now. These concentrated on small inorganic ions, (e.g. Li^+ [13, 14], SO_4 [15], HClO_4 [15]) where the lattice expansion is comparably small, and revealed changes in the height of multilayer steps due to layer expansion as well as the formation of blisters and surface films. Similar studies on the intercalation of organic molecules do not exist, but are highly interesting due to the larger changes in interlayer spacing that accompanies the intercalation (as well as the deintercalation) in these compounds. The latter results in higher stress, which may assist the formation of nanostructures, as well as cause pronounced electronic decoupling between the layers, i.e. quasi-2D behavior. Furthermore, organic intercalation compounds exhibit a much richer phase behavior, which potentially may be employed to form organic-inorganic nanostructures of different molecular architecture. Scanning tunneling microscopy is the perfect tool to study the surface morphology on the nm scale.

Nanowires are of fundamental as well as technological interest e.g. for nanoelectronics and sensor applications. In studies of metal deposition on the cleaved plane of layered transition metal dichalcogenide surfaces under ultrahigh vacuum (UHV) conditions, the formation of self assembled nanowire networks as well as larger tunnels for a variety of metal species and substrates has been reported [16–21]. These structures often are oriented along the close-packed directions of the substrate lattice and were originally attributed to admetal-induced cracking of the dichalcogenide surface layer, followed by metal nucleation and growth in the resulting linear defects [16, 17]. More recently, it was shown by electron microscopy that all these linear nanostructures corresponds to tunnels formed by folding of the substrate surface lattice [19, 21]. The main aim of the present work can be distinguished into two parts.

- To demonstrate the nm scale surface morphological changes during the electrochemical intercalation of organic molecules (e.g. pyridine, octylamine) into TaS_2 .
- To demonstrate that electrodeposition of Cu onto TaS_2 , leads to the formation of similar nanostructures observed during Cu deposition onto TaS_2 in vacuum and to compare them with those formed under vacuum conditions.

A description of all the single crystals employed for intercalation and electrodeposition are given in chapter 1. In chapter 2 and 3, the basics of intercalation and electrodeposition are described. Details

of experimental realization and theoretical background of experimental techniques (STM, AFM , SEM, Cyclic Voltammetry) are given in chapter 4. A short review of literature as well as results of electrochemical characterization and microscopic studies of organic molecule intercalation and electrodeposition of Cu onto TaS₂ are discussed in chapter 5 and 6, respectively.

2 Transition Metal Dichalcogenides

Transition metal dichalcogenides (TMDCs) have been intensively studied for the last 40 years [1, 2, 22]. They are layered compounds of MX_2 type where "M" is a transition metal of group IV (Ti, Zr, Hf), V (V, Nb, Ta) or VI (Cr, Mo, W) and "X" is one of the chalcogens (S, Se or Te) (see fig. 2.1). The X-M-X sandwiches are stacked along the hexagonal c-axis to complete the structure. Within each X-M-X layer strong ionic and covalent bonding predominates whereas bonding between adjacent layers is weak and of van der Waals type. The layered transition metal dichalcogenides exhibit fascinating properties due to their van der Waals bonded layered structure. Superconducting behavior [23], nonlinear and anisotropic electrical properties [22], charge density wave (CDW) instabilities [24, 25] as well as intercalation chemistry [1, 2, 23] have been extensively studied.

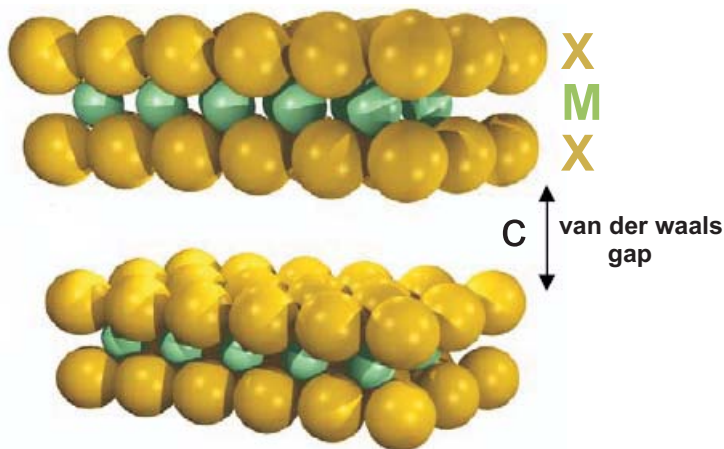


Figure 2.1: Layered structure of transition metal dichalcogenides [2].

The primary objective of the thesis was to investigate the intercalation of organic molecules in transition metal dichalcogenides (TMDCs). A number of dichalcogenides (e.g. TiSe_2 , NbSe_2 , TaS_2) were studied in this work. But experimental difficulties associated with TiSe_2 and NbSe_2 samples prevented further experiments. In particular, TiSe_2 crystals were oxidized in electrochemical environment whereas it was difficult to clamp the NbSe_2 crystals inside the electrochemical STM cell due to their small dimensions (diameter ≈ 2 mm and thickness ≈ 0.1 mm). However, TaS_2 crystals obtained by chemical vapor transport method (CVT) were large enough and suitable for our electrochemical experiments and therefore most of the results described in this thesis were obtained for TaS_2 crystals.

2.1 Crystal Structure

This section describes the crystal structure of different layered materials used in our experiments.

2.1.1 TiSe₂

TiSe₂ crystallize in a simple layer-type structure of the CdI₂-type (fig. 2.2). The structure consists of sandwich slabs, each slab with two layers of Se atoms, and with Ti atoms in octahedral holes. By increasing the Ti content, other stable forms (Ti₃Se₄ [26], Ti₅Se₈ [27], and Ti₈Se₉ [28]), which crystallize as NiAs type can also be prepared. TiSe₂ exists only in the 1T- polytype which crystallizes as brown-violet crystals by chemical vapor transport method at a temperature above 800°C. The terms 1 and T, stands for the number of layers needed to define a unit cell and the symmetry of the unit cell, respectively. The lattice parameters are $\approx 3.5 \text{ \AA}$ (a-axis) and 6 \AA (c-axis) respectively.

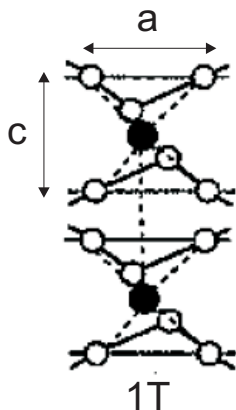


Figure 2.2: TiSe₂ existing as single 1T- polytype (taken from [29]).

2.1.2 NbSe₂

The NbSe₂ crystal is made of stacks of NbSe₂ layers, each layer consisting of a sheet of Nb atoms between two sets of Se atoms. It exists in three different polytypes 2H-, 3R- and 4H-NbSe₂ (see fig. 2.3). Below 910°C, the 2H type, between 910°C and 980°C, the 4H-NbSe₂ type whereas above 980°C, the 3-R type exists as the stable product.

In 2H NbSe₂, the Nb atoms of different stacks lie along a line perpendicular to the surface in a trigonal prismatic manner (fig. 2.3a). The 3R polytype structure has a rhombohedral arrangement where

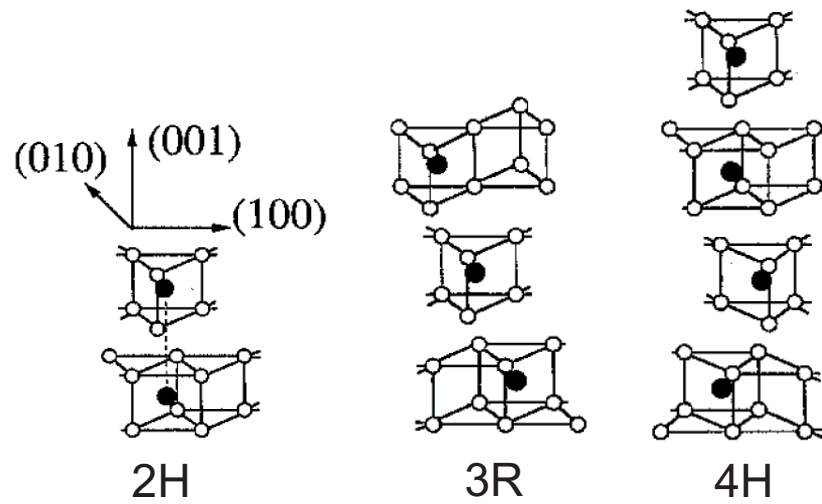


Figure 2.3: Different polytypes of NbSe₂ (a) 2H (b) 3R and (c) 4H type (taken from [29]).

three different layers constitute the unit cell (fig. 2.3b). In 4H-form, the metal atoms exclusively display mixed octahedral and trigonal-prismatic coordination (fig. 2.3c). The lattice constants are $a = 3.443 \text{ \AA}$ and $c = 12.547 \text{ \AA}$, respectively.

2.1.3 TaS₂

Due to the layered structure TaS₂ has a strongly two dimensional character both in its physical and chemical properties. The crystal is built up in sandwich layers shown in fig. 2.1. TaS₂ exists in several structural polytypes, which are made of different stacking sequences of the sandwich layers (see table 1) [2].

Table 1: Different polytypes of TaS₂ (taken from [2])

#Designation	#Space group	#Examples	#Metal coordination
1T	$\bar{p}3m1$	Group IVB, VX ₂ , TaS ₂ , TaSe ₂ , NbS ₂	Octahedral
2H _a	P6 ₃ /mmc	NbX ₂ , TaX ₂	Trigonal prismatic
2H _c	P6 ₃ /mmc	Group VIB	Trigonal prismatic
4H _a	P6 ₃ /mmc	TaS ₂ , TaSe ₂	Trigonal prismatic

The most common polytypes are 1T-TaS₂ and 2H-TaS₂, where 1T is a metastable phase at temperatures below 570 K whereas the 2H form is stable at room temperature. The unit cell is defined by a single layer of TaS₂ in 1T-polytype whereas in the 2H-polytype two TaS₂ layers are needed to define the unit cell. The terms, T and H stands for trigonal and hexagonal geometry of the unit cell respectively. Depending upon the crystal symmetry i.e. octahedral (1T) (see fig. 2.4a) or trigonal prismatic (2H) (see fig. 2.4b), the six sulphur atoms surrounding each tantalum atom are arranged in either octahedral or trigonal prismatic orientation, respectively. The term "a" and "c", denotes the lattice parameters i.e. the distance between adjacent chalcogens within a single layer and the layer perpendicular to each other respectively. For 1T-TaS₂, the values of a and c are 3.363Å and 5.896 Å respectively.

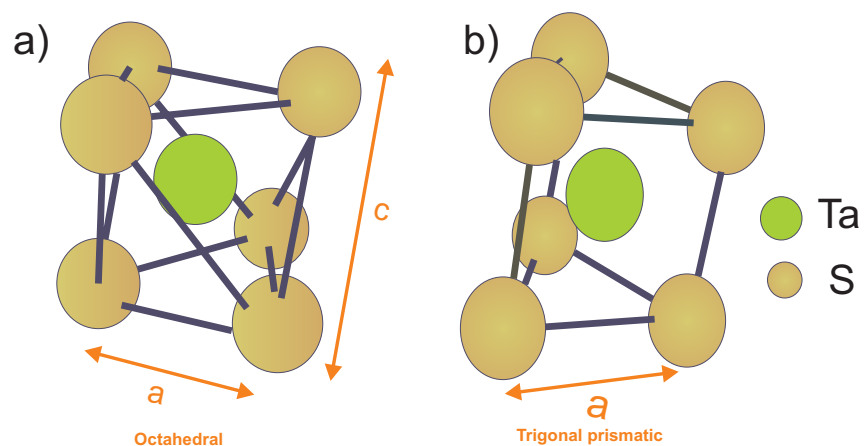


Figure 2.4: Octahedral (1T) and trigonal prismatic (2H) coordination structure of TaS₂. The drawn lines stress the geometry and do not refer to chemical interaction.

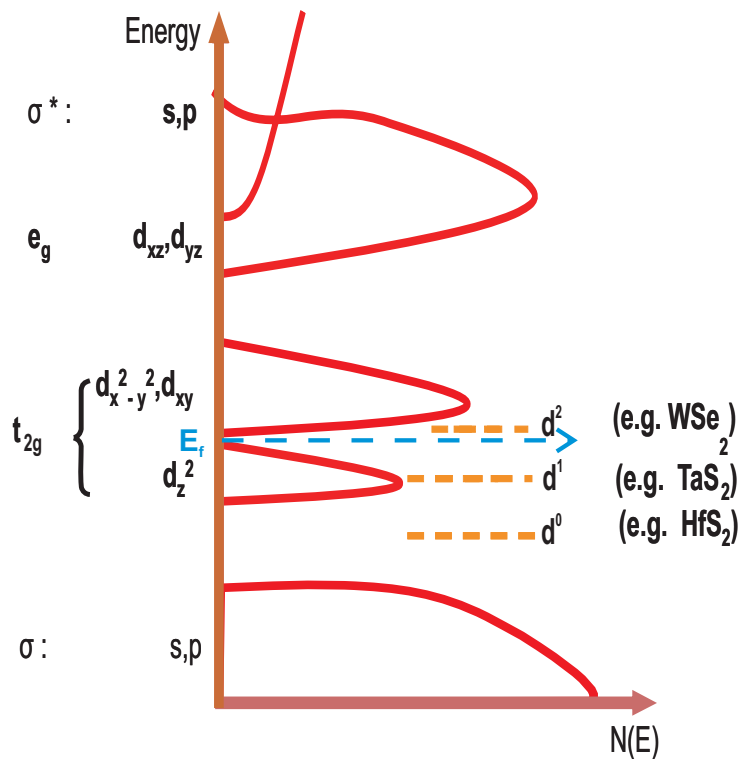


Figure 2.5: Electronic band structure of TaS_2 (taken from [30])

The electronic states of pure 1T- TaS_2 are arranged according to the scheme given by Wilson and Yoffe [22]. The Fermi level is situated in the range of the TaS_2 d bands, which are split into the 3 fold degenerate t_{2g} group and the 2 fold degenerate e_g group. The t_{2g} group is further divided into three sub bands formed from d_{xy} , $d_{x^2-y^2}$ and d_z^2 orbitals where d_z^2 is the lowest of the TaS_2 d states. As tantalum is a group V transition metal, one valence electron per unit cell remains in the Ta-derived states while four other electrons are used to fill the empty p state of two sulphur atoms in TaS_2 . Therefore the d band in TaS_2 is half filled and hence electron donors such as Lewis bases (amines, n-heterocyclic) can be easily intercalated by donating electron to the half filled d band, thus forming charge transfer intercalated complexes.

3 Intercalation

Intercalation is defined as the incorporation of mobile guest species (atoms, ions or molecules) into a crystal lattice containing an appropriate system of accessible empty lattice positions, according to the reaction.



Where

G = Guest species

H = Host lattice

Δ = Empty lattice sites

The process must be reversible and topotactic. The term topotactic means structural integrity of the host must remain unaltered and the guest ions must be mobile within the host lattice. Intercalation is a slow process and can be controlled by external parameters (e.g. potential, pressure, temperature etc.).

3.1 Host

The host must consist of a system of interconnected empty lattice sites. These free lattice sites must be large enough, in order to accommodate the guest species. The guest molecule and the host lattices must have similar electronic characteristics. For transition metal dichalcogenides (TMDCs) this means that only guests who serve as electron donors (metals, Lewis bases etc.) can be intercalated. More recently intercalation of non-donor species (e.g. ferrocene) has been achieved [31, 32]. Intercalation of a few electron acceptors (e.g. ICl, p-benzoquinone, chloranil, and TCNQ) was also attempted [33].

Potential host lattices that undergo intercalation may be divided into three different categories according to their structural characteristics. The geometrical conditions of the host not only limit the mobility of the guest molecules within its empty lattice sites, but also determine electronic properties of its intercalated product. Different categories of host lattices are shown schematically in fig. 3.6.

- **Three dimensional systems** consisting of a frame work host matrix that contains interconnected or isolated empty "channels" of unoccupied lattice sites which share polyhedral faces. There are

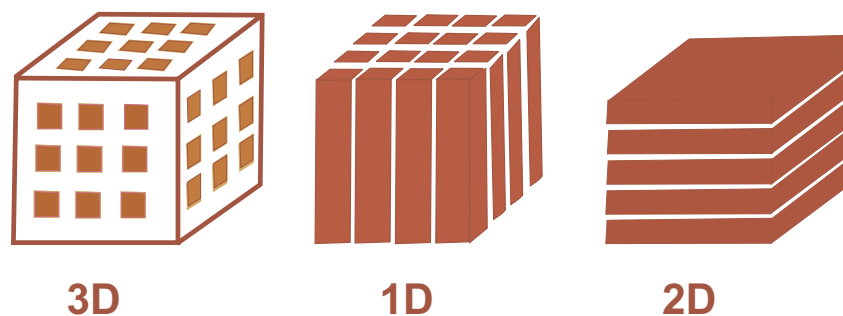


Figure 3.6: Schematics of basic host lattice types with different structural dimensionality.

rigorous restrictions with respect to the dimensions of the guest ions which have to be below the critical radius depending upon the host lattice.

- **One dimensional systems** consisting of chain-type units separated by van der Waals gaps which provide neighboring lattice sites. Their flexibility is higher for intercalation, however, they are rather susceptible to lattice defects, as the large crystal expansion during the intercalation results in the decrease in interaction between adjacent one dimensional units, and hence disintegration of the original crystal structure.
- **Two dimensional systems or layered structures** have always received preferred attention in intercalation chemistry due to the above mentioned difficulties for one and three dimensional lattices. As compared to three or one dimensional systems, host lattices with layered structures are characterized by their ability to intercalate besides metal ions also a large variety of molecular species of different size and geometry by expansion of the lattice, perpendicular to the layer planes. A variety of host lattices e.g. sheet silicates [34], layered cyanides [35], graphite [36], transition metal dichalcogenides [37] etc., have already been investigated.

Three different types of empty lattice sites e.g. tetrahedral, octahedral or trigonal prismatic sites defined by stacking of the chalcogen layers are available for intercalation of guests in TMDCs (see fig. 3.7). The coordination number of transition metals in TMDCs remains constant whereas stacking of the chalcogen layers may change during intercalation. A change in stacking sequence from 1T to 3R is reported during hydrazine intercalation into 1T-TaS₂ [38].

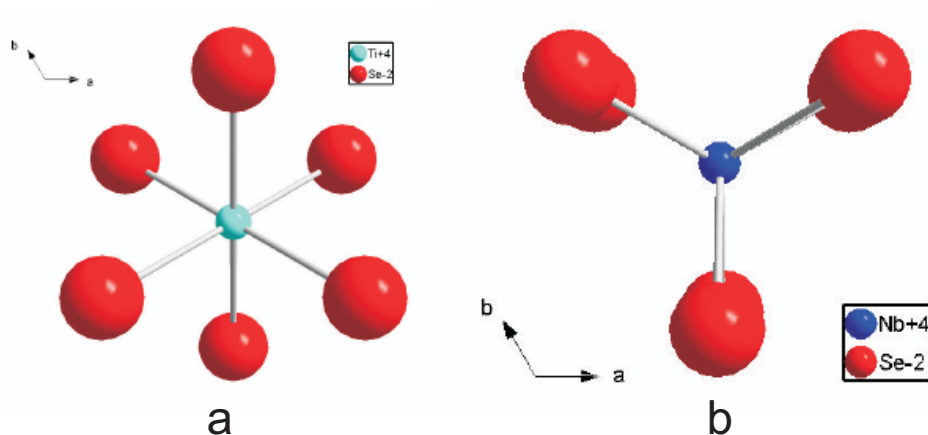


Figure 3.7: Different positions for guest molecules inside TMDC-layers (a) octahedral site (b) trigonal-prismatic site [39].

3.2 Guest

Most of the guest ions intercalated in TMDCs are electron donors [23], however, intercalation of neutral species [31, 32] as well as electron acceptors [33] has also been reported.

A large variety of guest species was found to intercalate into dichalcogenide lattices and were extensively studied. They can be categorized as:

- **Monoatomic species:** Electropositive metals (alkali and alkaline earth, Eu, Yb), post transition metals (e.g. Cu, Ag, Sn etc.)
- **Lewis base molecular compounds:** Inorganic and organic compounds with functional groups of Lewis base character (e.g. amines, heterocyclics such as pyridine etc.)
- **Cation/solvent complexes:** Polar molecular compounds solvating intercalated cations (e.g. main group and transition metal cations, organic and inorganic metal complex cations, organic cations etc.).

Since we are primarily concerned about the intercalation of organic molecules in this thesis, our discussion will be limited to Lewis bases only. Specifically, intercalation of pyridine and amine are discussed in detail. The major classes of organic molecules that form intercalation compounds with TMDCs are summarized in the table 2. In the case of organic intercalation compounds the host-guest

# Generic class	# Examples
Amines	$\text{RNH}_2, \text{R}_2\text{NH}, \text{R}_3\text{N}, \text{H}_2\text{N}(\text{CH})_n\text{NH}_2$
Phosphines	R_3P
Amides	$\text{RCONH}_2, \text{CO}(\text{NH}_2)_2$
Amine oxides	Pyridine N-oxide
Phosphine oxides	R_3PO
N-Heterocycles	Pyridine, Substituted pyridines
Isocyanides	RNC

Table 2: List of organic molecules that intercalate into layered transition metal dichalcogenides (taken from [2])

interaction which is primarily of charge transfer type, determines the rearrangement of the guest species within the layers and ultimately the stability of the intercalated compounds.

3.3 Product

Structural characteristics of intercalated TMDCs can be basically described by a staging model. The term staging indicates that not all the layers are filled at the same time, but that empty as well as intercalated layers can coexist. During intercalation, interlayer interactions slowly disappear and are replaced by interactions between layers and guests. Disulfides easily intercalated at milder conditions (e.g. dilute acidic media) than the diselenides (which intercalates in concentrated acidic media), while the ditellurides have not been reported to intercalate [2]. Staging has the effect of minimizing the energy required to break interlayer interactions. The staging process during intercalation within a single layer occurs in an ordered fashion. The order of the staging is given as the layer number that is fully or partially filled between the host layers. For example in case of 3rd stage compound every 3rd layer must be intercalated leaving two empty layers in between. The schematics for different stage models are shown in fig. 3.8. Pyridine intercalation in disulphides leads to both 1st and 2nd stage compounds whereas in amine intercalation staging has not been observed [2].

During progressive intercalation, the transition from stage 3 to stage 2 can not be explained by staging models alone without eventually emptying the already occupied layers. Assuming that stage changes occur without intercalate hopping or diffusion across TMDC layers inside the crystal, or without migration around TMDC layers at the crystal edge, this behaviour can be explained by a staging domain model

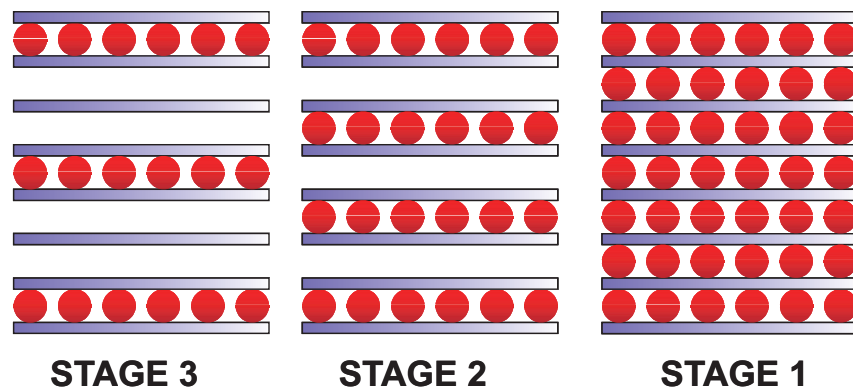


Figure 3.8: Models showing the staging phenomena in layered hosts.

or pleated layer model proposed by Daumas and Herold [40] (fig. 3.9).

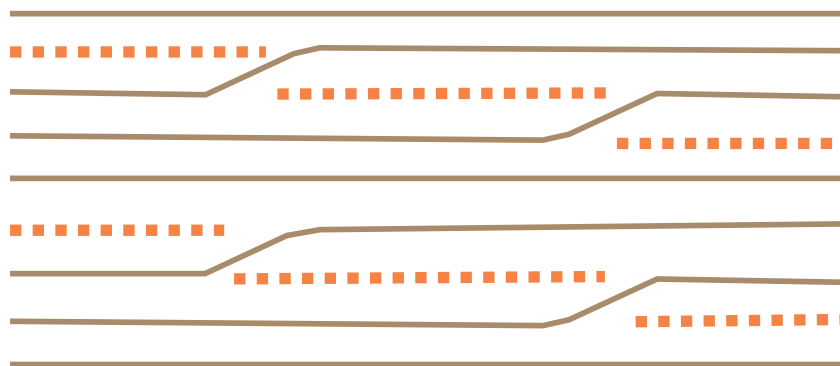


Figure 3.9: Daumas and Herold model showing the phenomenon of staging in layered hosts.

According to the Daumas and Herold model, the intercalated product consists of microscopic domains, such that within any domain the intercalate layers are continuous and together with the host layers form a well ordered (staged) sequence, but in different domains the intercalant atoms can be sandwiched between different pairs of TMDC layers. Thus a macroscopic intercalated crystal can be n -stage ($n =$ staging order) almost everywhere and at the same time globally there can be equal numbers of intercalates within each layer. This allows a phase transition, in which the stage index changes, by the movement of microscopic islands of intercalate atoms between adjacent domains within a single layer rather than the movement of intercalate perpendicular to the layer. Safran [41] and Hamann [42] have demonstrated that development of strain during intercalation is the the driving force for staging to occur. These authors have calculated the strain-induced forces between two intercalate atoms in a layered graphite host material, showing that intercalate atoms between the same two graphite layers are attracted

to one another to form two-dimensional islands, while intercalate atoms on different layers interact repulsively. By forming intercalate islands, the compound lowers its strain energy by ≈ 0.1 eV per intercalate atom, and the free energy is minimized by the formation of a pure stage configuration from a mixed or randomly staged crystal.

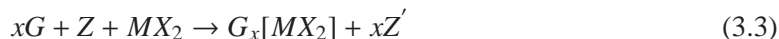
3.4 Process

The intercalation process can be carried out by the following methods.

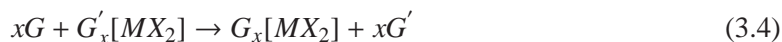
1. Direct thermal reaction of the host lattice "MX₂" with the guest phase "G" either pure or dissolved in an appropriate fluid phase:



2. Chemically assisted intercalation, i.e. when direct molecular intercalation is not possible thermodynamically or is kinetically unacceptably slow, the intercalation of many guest species can be achieved via assisted intercalation. For example, the assisting species may facilitate the redox process needed to form stable ionic species, or provide sufficient guest host attraction to achieve intercalation. This process can be described by the equation (Z and Z' are the assisting species and unintercalated products):



3. Exchange reactions where a guest ion is replaced by another guest ion :



4. Cointercalation where different guests can coexist within the host:



5. Electrochemical intercalation by discharge of guest cations from electrolytes on dichalcogenide cathodes :



Since we exclusively employed the electrochemical intercalation process in this work, only details of electrochemical intercalation are discussed here.

3.5 Electrochemical Intercalation

The electrochemical intercalation is a convenient way to synthesize TMDCs intercalated compounds and has several advantages. For example, it is easy to control the stage structure of the products, the rate and the degree of intercalation by adjusting the electrochemical parameters (e.g. current, potential etc.). The electrical conductivity of the TMDCs is an essential condition for electrochemical intercalation.

Electrochemical intercalation is based upon a classical three electrode (working, counter and reference) system (see fig. 3.10) where the host material acts as the working electrode (WE). The counter electrode (CE) is typically a platinum wire that provides a surface for a electrochemical reaction which provides current for the reaction at the working electrode (WE) to occur. A reference electrode is used to measure the potential of the working electrode at negligible current. All the potentials changes for working electrode (WE) are then refered with respect to the reference electrode. The electrolyte generally contains the intercalate species in aqueous or organic solutions. In addition, a voltmeter (U) and an ammeter (I) connected to the electrochemical cell measure the voltage and current, respectively. Electrochemical intercalation processes are generally carried out either by applying either a constant/pulsed current (galvanostatic) or voltage (potentiostatic) for different time periods (for details see section 3.5.2). In our in situ STM studies a constant potential was applied for different time periods.

3.5.1 Thermodynamics of Electrochemical Intercalation

The most important aspect of thermodynamics of intercalation is that the concentration of the guest can change. Consequently, we are interested in changes in gibbs free energy G with the number n of intercalated guest atoms. The thermodynamic quantity describing these changes is the chemical potential

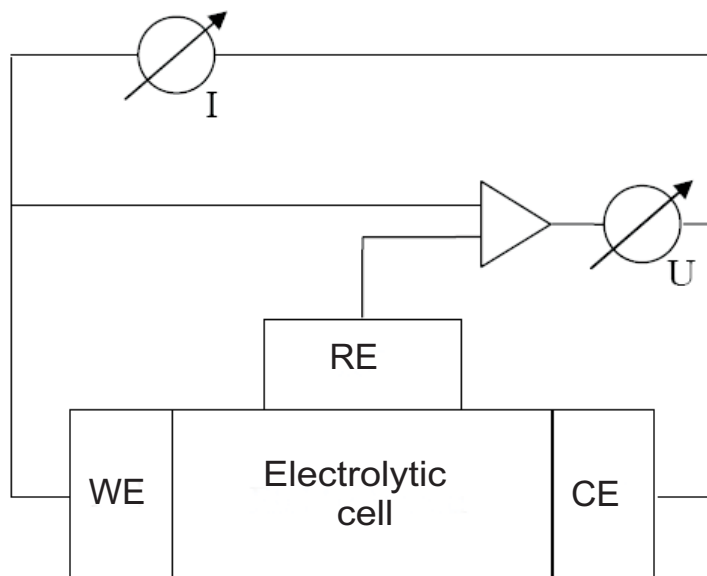


Figure 3.10: Schematics of a cell for electrochemical intercalation.

μ , which is related to the free energy change as

$$dG = \sum_i \frac{\mu_i}{dn_i} \quad (3.7)$$

where " μ " is the chemical potential, "G" the Gibb's free energy and "n" the number of molecules of the guest species. The advantage of studying intercalation with electrochemical cells is that μ can be measured directly from voltage E between the electrodes of such cells.

Consider a cell with Host (MX_2) as one electrode and an inert material (Pt) as other electrode in an electrolyte containing the intercalated ions. Denote the chemical potentials of intercalate (G) in the host and in electrolyte as μ and μ_0 , respectively. If the intercalate has charge ze in the electrolyte of the cell, one ion is intercalated for every z electrons passed through the external circuit. Since the electrons move through the potential difference E, the work done on the cell per ion intercalated is $-zeE$. This work must be equal to the change in free energy of the intercalate in host and electrolyte, which in other words equivalent to $\mu - \mu_0$, so

$$-zeE = \mu - \mu_0 \quad (3.8)$$

Thus measuring the cell potential at equilibrium vs charge passed between the electrodes is equiva-

lent to measuring the chemical potential as a function of x , the intercalate content in the host. Thermodynamics requires that μ increase with the concentration of the intercalates, and so E decreases as more and more intercalates are added to the host.

During the intercalation process, however the decrease in cell potential usually is not continuous. In most of the intercalation processes the decrease in cell potential is accompanied by formation of plateaus or regions of smaller inclinations indicating a first order phase transition between two different phases (see fig. 3.11). Since the compositions of the coexisting phases do not change, the chemical potential is constant in this two-phase region.

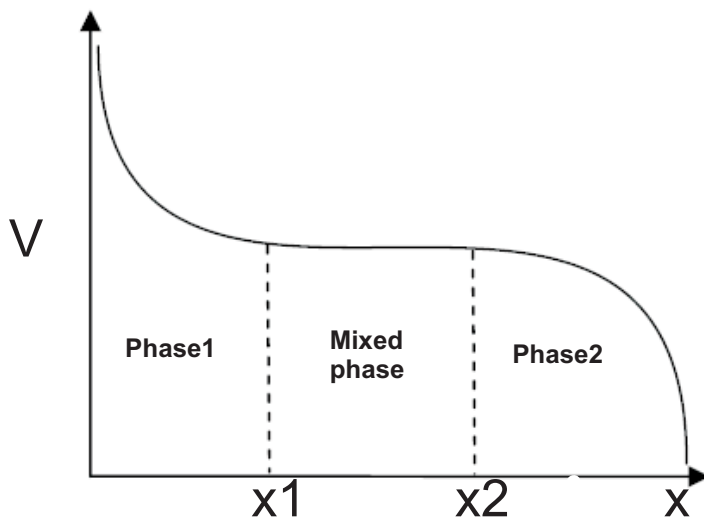


Figure 3.11: Plot of potential vs. increase in degree of intercalation showing different phase regions [39].

Other thermodynamic properties (enthalpy, entropy) which are related to the chemical potential or Gibb's free energy within a plateau can also be derived from the following relationships.

$$\mu = \frac{\partial G}{\partial n} = \left(\frac{\partial H}{\partial n} \right) - T \left(\frac{\partial S}{\partial n} \right) \quad (3.9)$$

where ∂H and ∂S are the partial enthalpy and entropy changes of the system respectively. According to a Maxwell equation, the change in entropy can be determined from the chemical potential of the system

by the following relationship.

$$\left(\frac{\partial\mu}{\partial T}\right)_n = \left(\frac{\partial S}{\partial n}\right)_T \quad (3.10)$$

Combining equation 9 and 10, we get

$$\mu = \left(\frac{\partial H}{\partial n}\right) - T \left(\frac{\partial\mu}{\partial T}\right) \quad (3.11)$$

Thus at a constant temperature, the enthalpy of the system can be determined from the chemical potential value.

3.5.2 Specific Electrochemical Intercalation Methods

Electrochemical intercalation processes generally occur by electron transfer between the electrodes when current or voltage is applied through the external circuit. Different electrochemical methods which either uses a constant/pulsed current or potential for intercalation are as follows :

- **CC** : Constant Current Method
- **CP** : Constant Potential Method
- **GITT** : Galvanostatic Intermitted Titration Technique.
- **PITT** : Potentiostatic Intermitted Titration Technique

These methods are developed and described by Weppner and Huggins [43–46]. A small description of these processes is given here. In the CC and CP method, the host material is kept under a constant current or potential whereas pulsed current or potential is applied in the case of GITT and PITT. The change in current and potential as a function of the degree of intercalation for different methods is shown schematically in fig. 3.12. In all the methods the degree of intercalation in the host can be determined by the following formula assuming no competing electrochemical reactions (e.g. H_2 -evolution, deposition) occurs :

$$x = \frac{I_o \cdot \tau \cdot M_{host}}{z_i \cdot m_{host} \cdot F} \quad (3.12)$$

where

x = Degree of intercalation

I_o = Current

τ = Intercalation time

F = Faraday's constant

M_{host} = Molecular weight of the host

m_{host} = Mass of the host

z_i = Number of transferred charges

In the CC method a constant current flows through the electrochemical cell. In this method the degree of intercalation (x) is directly proportional to the applied current. A constant current from external source e.g. potentiostat, facilitates the formation of guest ions (cations), which ultimately migrate towards the host electrode (behaves as cathode), resulting in the formation of intercalated product. The termination of intercalation is generally characterized by interrupting the current. Typically this leads to the formation of a new equilibrium state. Once the host lattice reaches the maximum degree of intercalation, further application of current results in host lattice disintegration.

In the CP method, the potential is kept constant in the range of intercalation resulting in the polarisation of the host lattice. The polarisation is dependent on the chemical potential and hence on the degree of intercalation of the host lattice. Consequently, the current density will also decrease during progressive intercalation. The intercalation will be terminated when the degree of intercalation of the host lattice reaches equilibrium with the applied potential and no further current will flow through the cell.

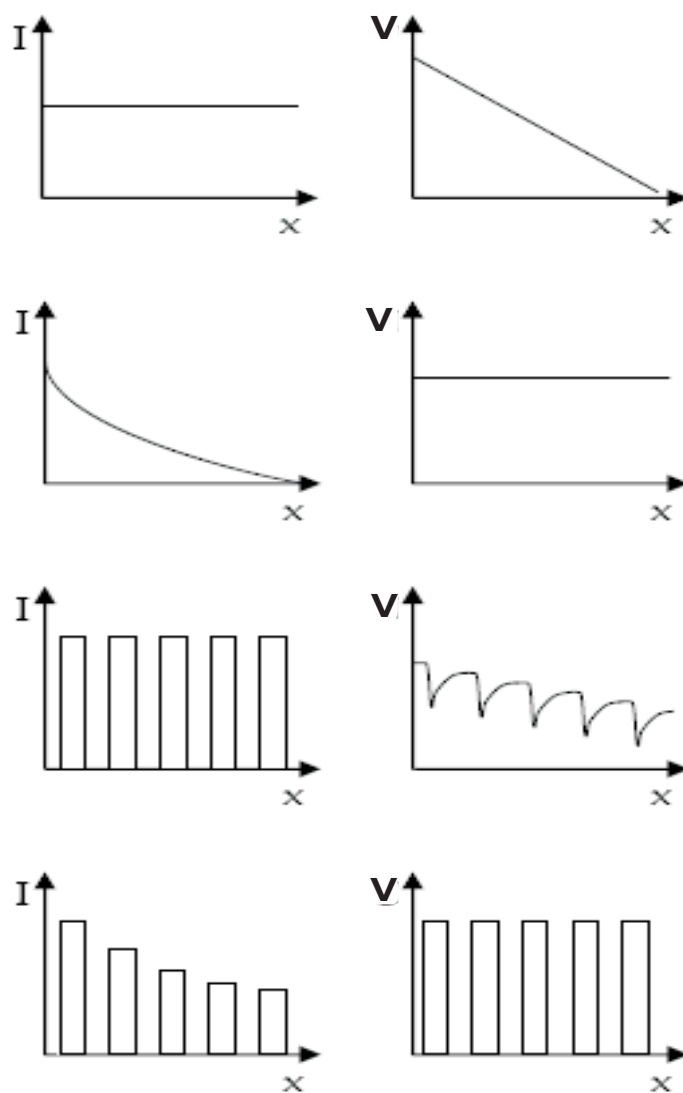


Figure 3.12: Schematics of the change of current (I), potential (V) vs. degree of intercalation (x) for different electrochemical intercalation methods. From top to bottom : CC, CP, GITT, and PITT, respectively (taken from [39]).

In both CC and CP method, the host lattice undergoes an expansion in order to accommodate the guest molecules. The current/ potential step is continuous and hence leaves practically no time for the host lattice to undergo any kind of relaxation to relieve stress during intercalation, which ultimately results in a lot of stress inside the intercalated host. If the stress during intercalation is too large, host disintegration can also occur. The CC method has an advantage over CP method of making products of different stoichiometry by interrupting the applied current during intercalation. During an intercalation process by

CC method, the plot of potential vs. degree of intercalation indicates phase transitions between different phases inside the host layers (see fig. 3.11). Generally, intercalated guest molecules with a similar type of arrangement within the host layer constitute a single phase with well-defined free energy. However, depending upon the arrangement of intercalates in different phases, the free energy associated with them also differs. Consequently phases having higher free energy try to minimize the energy by rearrangement of the intercalates. Mixed phases i.e. both stable as well as less stable phases can also coexist, where less stable phase that form during intercalation rearranges slowly into the more stable phase.

In the galvanostatic and potentiostatic intermitted titration technique, the host lattice is intercalated by applying pulses of constant current CC (GITT) or constant potential CP (PITT). After every pulse the host lattice has time to relax and come to equilibrium before the next pulse is applied. The advantage of these methods is that, the intercalate has ample time to reach equilibrium which results in lesser originated defects during intercalation. Thermodynamic data for the degree of intercalation x can also be determined from the applied pulses. For example the diffusion coefficient (D) of guest ions in an intercalation reaction can be determined by the GITT method using Fick's law, which describes the time dependent change in concentration at the guest/host interface as reported by Weppner et al. [44].

During an intercalation process the guest and host undergo the following structural changes:

1. Chemisorption of the guest species at the active reaction sites of the host.
2. Intercalation of guest species along defect site of the host along with deformation of host layers.
3. Diffusion and ordering of islands (staging) within the host layers.
4. Saturation of host-guest intercalation leading to the formation of a stable intercalated product.
5. As a competing reaction, nucleation of the guest species and island growth on the host surface also occurs.

Chemisorption occurs only at the reactive sites of the hosts. In the case of TMDCs, the layer edges as well as the defects on the surface are the active sites for chemisorption. Studies by Acrivos [48, 123] et al. have shown that intercalation in single crystals occurs by the adsorption of guest species on the outer basal plane of the host and proceeds from the basal plane towards the centre of the crystal resulting in the successive intercalation of the adjoining layers.

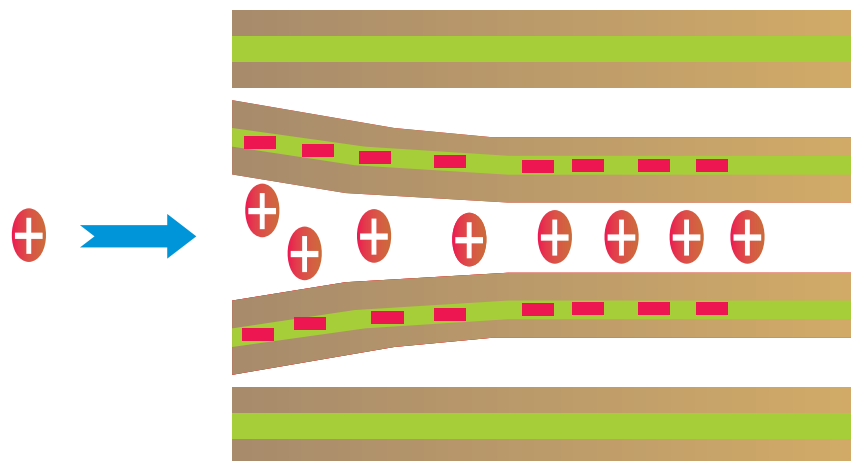


Figure 3.13: Increased repulsion of the layers at the edges by localized charges (taken from [39]).

In TMDCs, bending of the layers often occurs during intercalation of guest species. Such layer bending during electrochemical Li intercalation into TiS_2 has already been reported [49] and attributed to the lifting of edges of TiS_2 caused by interdiffusion of intercalated Li ions in unintercalated layer. In addition, cracking and rifting of the crystals were also observed and attributed to the relaxation of strain produced during bending of layers. Layer bending in HOPG (so called ashtray effect) by intercalation of large polymer ions is also reported [50]. Bending which occurs by elastic deformation of the host layers is due to electron transfer from the guest to the host lattice [49]. In the beginning of the intercalation process, the transferred electrons from the guest i.e. the electrons produced by ionisation of guests under the influence of applied potential, remain at the edges of the host layers which subsequently leads to the repulsion between the layers and finally its bending (fig. 3.13). Enough electrons have to be transferred to the host lattice for layer bending and subsequent accommodation of guests which forms islands within the layers. Once the islands are formed they can also cause further bending of the host layers due to their bulkier sizes as well as rearrangement within the host, in order to minimize the surface energy and to attain a stable configuration within the host. The diffusion of the islands leads to the formation of different domains which ultimately results in giving rise to different staging structures. An ordering of the domains results in thermodynamical stability of the intercalated host. An intercalation process is complete when both steric and electronic saturation occurs within the host lattice [39].

3.6 Previous In-situ High Resolution Microscopy Intercalation Studies

In situ high resolution microscopic studies of the intercalation of ions in transition metal dichalcogenides do not exist. However, intercalation of some small inorganic ions, e.g. Li^+ [13, 14], SO_4^{-2} [15], HClO_4^- [15]) into highly ordered pyrolytic graphite (HOPG) were already reported. The first in situ STM evidence of step height increase during intercalation of Li^+ from 1 M LiClO_4 /ethylene carbonate-diethylcarbonate into HOPG was reported by Inaba et al. [13]. A step height increase from 30\AA (equivalent to 9 graphite layers) to 40\AA was found and attributed to the intercalation of solvated Li^+ ions in every HOPG layer. In addition, two different types of hill like structures or islands were also observed at the surface grain boundaries and at steps on the surface, which they attributed to islands of the solvated intercalated Li^+ ions formed within the HOPG layers. In situ AFM studies by Chu [51] et al. for Li^+ intercalation from different electrolytes (1 M LiClO_4 /ethylene carbonate-dimethylcarbonate and LiPF_5 /ethylene carbonate-dimethylcarbonate) into HOPG, indicated similar blister formation over an area of several μm . They indicated that these blisters formed due to the electrolyte reduction and deposition of organic species from the electrolyte rather than solvent cointercalation as reported by Inaba et al. [13]. Alliata et al. first demonstrated in situ STM studies of anion (SO_4^{-2} , HClO_4^-) intercalation into HOPG. Step height increase as well as occasional blister formation during intercalation was also observed. In addition, formation/dissolution of blisters by changing the potential to the cathodic/anodic regime were also demonstrated. During HClO_4 ion intercalation, formation of different stage products at different cathodic potential regimes were also reported.

4 Electrodeposition

Electrodeposition is one of the principal application of classical electrochemistry since the discovery Faraday's law of electrodeposition in 1834 [52]. Huntington was the first to show the electrodeposition under a microscope [53]. Kossel and Stranski made the connection to concepts of crystal growth of the deposited adions [54], while Erdey-Gruz and Volmer suggested that the diffusion to growth sites occurred in the double layer [55]. Kohlschutter and Toricelli first demonstrated the formation of islands during electrodeposition [56]. Fischer was the first to attempt an interpretation of the complex effects of industrial electrodeposition at molecular level [57].

In today's world electrodeposition is emerging as a uniquely capable method for making materials and structures needed for a nanotechnology- and nanobiotechnology based future. It also provides some unique opportunities for directly depositing materials onto a surface without going through the difficult steps that are used in conventional techniques.

Electrodeposition has three main attributes that make it so well suited for current and future nano-, and microtechnologies research [58].

- It can be used to grow functional material through complex 3D masks (mask electrodeposition).
- It can be performed near room temperature from water-based electrolytes.
- It can be scaled down to the deposition of a few atoms or up to large dimensions.

The first attribute is based on the key concept that electrodeposited materials grow from the conductive substrate outward, and the geometry of the growth can be controlled using an insulating mask. This process is also called mask electrodeposition. It has been used extensively to pattern metal, semiconductors and polymers on conducting surfaces [59].

The second attribute has several advantages. Being a water based process it is environmental friendly. But, perhaps the most exciting implication of room temperature, water-based processing is that electrodeposition is compatible with proteins. Using proteins to control the growth of electrodeposited materials is truly a frontier area where biology meets nanotechnology [60].

The final attribute of electrodeposition is its ability to be scaled down (by the down scaling of conventional techniques) and scaled up (using new techniques that assemble structures atom by atom or

nano fabrication). This versatility means electrodeposition is being explored for a wide array of unconventional micro- and nanofabrication methods, ranging from nanopatterning with a scanning tunneling microscope as well as patterning large substrates using a process called electrochemical printing (ECP) [61, 62].

4.1 Basic Concepts of Electrodeposition

Electrodeposition or electrochemical deposition of metals involves the reduction of metal ions from aqueous, organic or fused salt electrolytes. In its simplest form the reaction in aqueous medium at the cathode follows the equation



with a corresponding anodic reaction. The anode material can either be the metal to be deposited (in this case the electrode reaction is electrodisolution that continuously supplies the metal ions) or the anode can be an inert material and the anodic reaction is oxygen evolution (in this case the plating solution is eventually depleted of metal ions). The deposition reaction presented in equation 4.13 is a reaction of charged particles at the interface between a solid (metal) electrode and a liquid solution. The two types of charged particles that can cross the interface are metal ions " M^{+n} " and electrons " e^{-} ".

Electrodeposition is carried out in a three electrode electrochemical cell that contains a "working electrode", a "reference electrode", and a "counter electrode". For electrodeposition to occur the working electrode must be conducting.

The reduction of a metal, which occurs during the deposition process, has been generalized in equation 4.13 for single metallic ions. Obviously, to reduce one mole of a given metal " n " moles of electrons are required. That is, the total cathodic charge " Q " (coulomb) used in the deposition, is the product of the number of gram moles of the metal deposited " m ", the number of electrons taking part in the reduction " n ", Avogadro's number " N_a " (the number of atoms in a mole), and the electrical charge per electron " Q_e " (coulomb). Thus, the following equation gives the charge required to reduce " m " mole of metal:

$$Q = mnN_aQ_e \quad (4.14)$$

Now, the product of the last two terms in this equation is the "Faraday constant" "F". Therefore, the number of moles of metal reduced by charge "Q" can be obtained as:

$$m = \frac{Q}{nF} \quad (4.15)$$

On the other hand, the total charge used in the deposition can be obtained as the product of the current "I" (ampere) and the time of deposition "t" (second), if the deposition current is held constant. Or, if the current varies during the deposition:

$$Q = \int I \cdot dt \quad (4.16)$$

So, the number of moles deposited can be calculated as:

$$m = \frac{1}{nF} \int I \cdot dt \quad (4.17)$$

The weight of the deposit "w" (gram) can now be obtained by multiplying equation 4.17 with the atomic weight "M_w" of the deposited metal. Finally, to calculate the thickness of the deposit, we have to use the density of the metal "ρ" (gram · cm⁻³):

$$\rho = \frac{w}{V} = \frac{w}{AT} \quad (4.18)$$

where "V" is the volume of the deposited metal in cm³, "A" is the area of the deposit in cm², and "T" is its thickness in cm. Solving for thickness, using equations 4.17 and 4.18 we have the useful practical expression:

$$T = \frac{w}{A\rho} = \frac{M_w}{nFA\rho} \int I \cdot dt \quad (4.19)$$

As mentioned above, if the current was held constant during the deposition, the integral in equation 4.19, can be replaced by the simple product of current and time "It".

The deposition reaction involves four types of issues. They are:

- Thermodynamics of the deposition process.
- Electron transfer at the metal-solution interface (electrode kinetics).
- Mass transport involved in the deposition.

- Nucleation and growth process of the metal lattice (M lattice).

4.2 Thermodynamics of the Deposition Process

The thermodynamics of the deposition process determines the limit of the applied potential needed to initiate a reaction. It is dependent upon the Gibbs free energy (ΔG) of the reaction, which is a function of applied potential, given by equation 4.20:

$$\Delta G = -nF\Delta E \quad (4.20)$$

where F is the Faraday's constant equivalent to 96485 C, ΔE is the electromotive force (EMF) and n is the number of electrons.

4.2.1 Nernst Equation

The Nernst equation describes the dependence of the equilibrium potential on the concentration of the involved electroactive species which ultimately correlates the ΔG (Gibb's free energy) and the equilibrium potential of the deposition system at equilibrium. For the standard electrode reaction given in equation 4.13), the Nernst equation is represented as :

$$E = E^o - \frac{RT}{nF} \ln C_M^{n+} \quad (4.21)$$

The notation C_M^{n+} represents the concentration (ML^{-1}) of the species, that undergo reduction during the deposition reaction.

4.3 Electrode Kinetics

4.3.1 Electrochemical Double Layer

The electrochemical reactions occur at the electrolyte-electrode surface where a double layer forms, which is on the order of 1 nm thick. The potential difference across the thin double layer establishes a strong electric field. The field orients the dipoles of the molecules of water in the electrolyte and the excess charge on the electrode surface is compensated by an accumulation of excess ions of the opposite

charge in the electrolyte. The amount of charge is a function of the electrode potential so that the double layer is similar to a simple parallel plate capacitor. The structure of the double layer generally depends upon the concentration as well as composition of the electrolyte at the interface.

4.3.2 Overpotential Deposition and Butler-Volmer Equation

The Nernst potential represents the potential, when the system is at equilibrium. In an electrochemical cell the deposition process is generally carried out by applying a current (galvanostatic) or potential (potentiostatic), from an external source, e.g., a potentiostat. At this point, the equilibrium potential is replaced by so called overpotential which is the difference between Nernst potential and applied potential. The overpotential drives the electrode reactions to proceed at a required rate or its equivalent exchange current density and thus leads to a current flow through the cell. The latter is related to the overpotential via Butler-Volmer-equation (see equation 4.22) (fig. 4.14)

$$i = i_0 \left\{ \exp\left(\frac{\alpha n F}{RT} \eta\right) - \exp\left(-\frac{(1 - \alpha) n F}{RT} \eta\right) \right\} \quad (4.22)$$

where F is the Faraday constant, R the universal gas constant, T the absolute temperature, i is the anodic or cathodic current, α is the charge transfer barrier or symmetry coefficient for the anodic or cathodic reaction, typically close to 0.5, and the overpotential $\eta = E - E^0$ is the difference between the applied potential of the electrode, E , and the equilibrium potential of the electrode couple, E^0 .

4.4 Mass Transport

The Butler-Volmer equation (equation 4.22) indicates that with increasing potential, the current will increase without limit. However, this is not correct as the reaction is limited by the rate at which the reactant arrives at the electrode. This leads to a situation when further changes in the electrode potential do not increase the current density. At this point, the deposition created a concentration gradient near the electrode surface, referred to as the diffusion layer. This phenomenon is known as mass transport and is characterized by a limiting or maximum current density (fig. 4.14). This limiting current establishes the maximum rate of reaction and is given by equation 4.23:

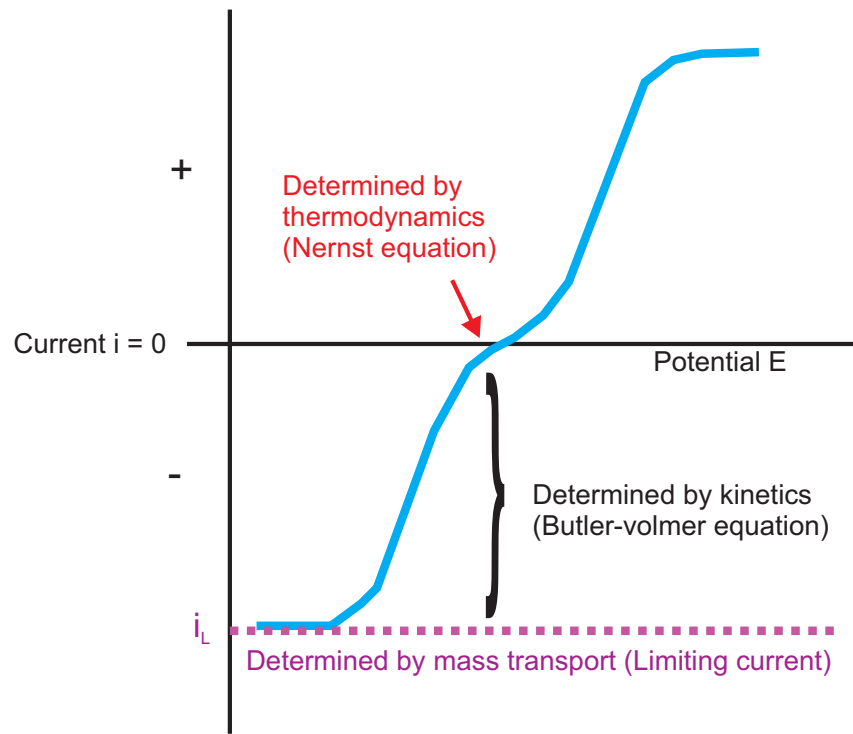


Figure 4.14: Butler volmer function for diffusion limited currents.

$$i_L = \frac{-nFD(C_{bulk} - C_s)}{\delta} \quad (4.23)$$

where, D is the diffusion coefficient of the deposited metal, C_{bulk} is the bulk concentration of the metal ions in the solution, C_s is the surface concentration of the metal ions and δ is the diffusion layer thickness. Ultimately, at the limiting current, $C_s = 0$, the current distribution over the cathode is entirely governed by mass transport and becomes independent of the potential distribution in the bulk electrolyte. A detailed discussion of these issues can be found in the literature [63, 64].

4.5 Nucleation and Growth

Deposition and crystal growth or the formation of adlayers on top of a substrate occurs in principle by the integration of additional atoms or ions/complexes into a characteristic arrangement, be it the substrate lattice or a new, independent lattice structure on top of the substrate. In detail three cases are distinguished: while for homoepitaxial growth both the substrate and the deposited film are of the

same material, heteroepitaxial growth denotes deposition of a different species on top of the substrate. With 'epitaxial' a well defined correlation between substrate and adlayer structure is denoted. If both structures are even identical, they are called pseudomorphic.

According to Kolb et al. [65], it is well known that metal deposition sets in preferentially at surface defects which act as nucleation centers for the new phase' (heterogeneous nucleation). Alternatively, also homogeneous nucleation takes place leading to nucleation of islands. After the saturation density of nucleation centers has reached a saturation value (typically the case for a coverage $\theta > 0.1$ monolayer), all further atoms are attracted. This critical value θ depends, amongst others, on surface diffusion processes, the binding energy of the islands, and the temperature. For further details readers are referred to [66].

If the deposited atom is not directly adsorbed at a defect site, a step edge or so called kink site, but randomly distributed on top of the surface, several transport phenomena to these nucleation centers exist. Fig.4.15 gives an overview of the most important single atom processes on a growing crystal surface. These processes depend as well on system parameters [66] such as material, crystalline order, growth rate, temperature, interface structure, and potential [67]. For further understanding of growth processes the distinction between intralayer and interlayer mass transport is fundamental. The former denotes the diffusion of adatoms on a flat terrace while the latter denotes the diffusion of single atoms across a step edge onto a lower terrace.

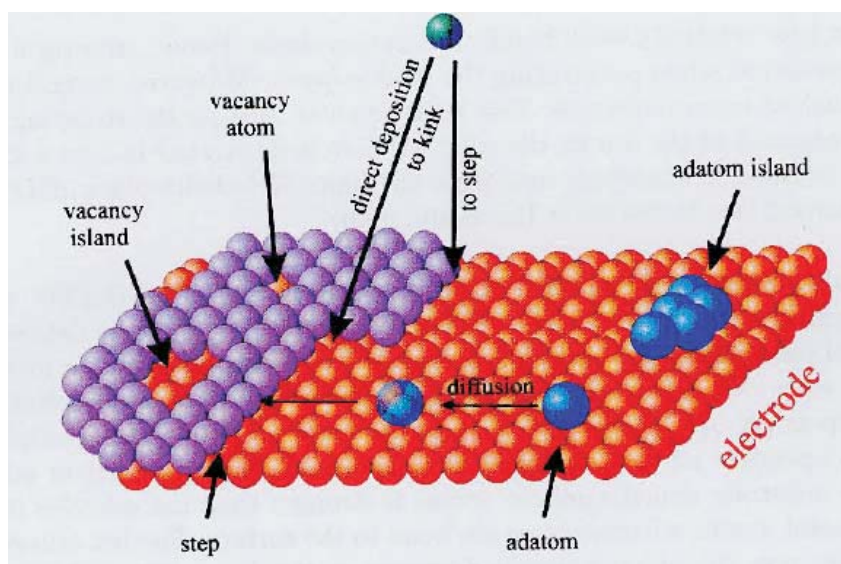


Figure 4.15: Most important deposition processes (taken from [68]).

Metal deposition is influenced by both thermodynamic and kinetic aspects. One relies on the energetics of the substrate, of the deposited metal and of the boundary between the substrate and adlayer (thermodynamic aspects). The other describes the deposition process as a result of the different rates of the individual elementary processes taking place on the atomic scale during deposition (kinetic aspects). Assuming, that the deposition and growth process takes place at almost equilibrium conditions (i.e., almost no kinetic influences), three different thermodynamic growth models can be distinguished in heteroepitaxial growth, as depicted in fig.4.16. These are: (1) Frank van-der-Merwe (FM) or layer by layer growth, (2) Volmer-Weber (VW) or 3D island growth and (3) Stranski-Krastanov (SK) or 3D island-on-wetting-layer growth. In Volmer-Weber (VW) growth, adatom-adatom interactions are stronger than those of the adatom with the surface, leading to the formation of three-dimensional adatom clusters or islands. Growth of these clusters, along with coarsening, will cause rough multi-layer films to grow on the substrate surface. On the other hand, during Frank-van der Merwe (FM) growth, adatoms attach preferentially to surface sites resulting in atomically smooth, fully formed atomic layers. This layer-by-layer growth is two dimensional, indicating that complete films form prior to growth of subsequent layers. Stranski-Krastanov (SK) growth is an intermediary process characterized by both 2D layer and 3D island growth. Transition from the layer-by-layer to island-based growth occurs at a critical layer thickness which is highly dependent on the chemical and physical properties, such as surface energies and lattice parameters, of the substrate and film. Details on these growth models can be found in the literature [69–71].

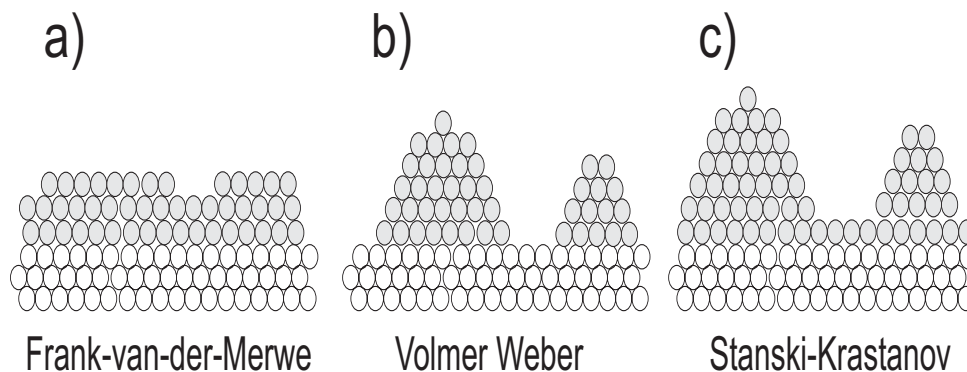


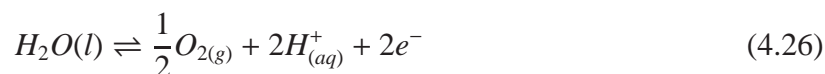
Figure 4.16: The growth modes. a) Frank-van-der Merwe (layer-by-layer) growth, b) Volmer-Weber (3D island) growth and c) Stranski-Krastanov (3D island-on-layer) growth [20]

4.6 Electrodeposition of Copper

In the case of copper electrodeposition from acidic sulphate solutions, the reduction reactions that take place at the working electrode (cathode) surface are :



The total cathodic current is the sum of the contributions due to each of these reactions. While copper is deposited at the working electrode under acidic conditions, the possible anodic reactions taking place at the counter electrode are usually



In $10^{-2}M$ $CuSO_4$ and $10^{-2}M$ H_2SO_4 electrolyte, Cu bulk deposition on TaS_2 starts at a potential of about -0.2 V vs. SCE. The calculated Nernst potential is +0.022 V vs. SCE.

5 Experimental Methods

A short description of the different experimental techniques used in our study is given here. For details readers are referred to the corresponding references.

5.1 Cyclic Voltammetry (CV)

Early contributions to cyclic voltammetry were made by various investigators, including Randles [72], Shain [73] and Nicholson [74]. Cyclic voltammetry is one of the most versatile electroanalytical techniques for the study of electroactive species. It has the capability for rapidly observing redox behavior over a wide potential range. It involves the cycling of the potential of an electrode, which is immersed in an unstirred solution, and measuring the resulting current [75]. The electrode potential is ramped linearly to a more negative potential, and then ramped in reverse back to the starting voltage. The forward scan produces a current peak for any analytes that can be reduced through the range of the potential scan. The current will increase as the potential reaches the reduction potential of the analyte, but then falls off as the concentration of the analyte is depleted close to the electrode surface. As the applied potential is reversed, it will reach a potential that will reoxidize the product formed in the first reduction reaction, and produce a current of reverse polarity from the forward scan. This oxidation peak will usually have a similar shape to the reduction peak. A schematic of a cyclic voltammogram is shown in fig 5.17.

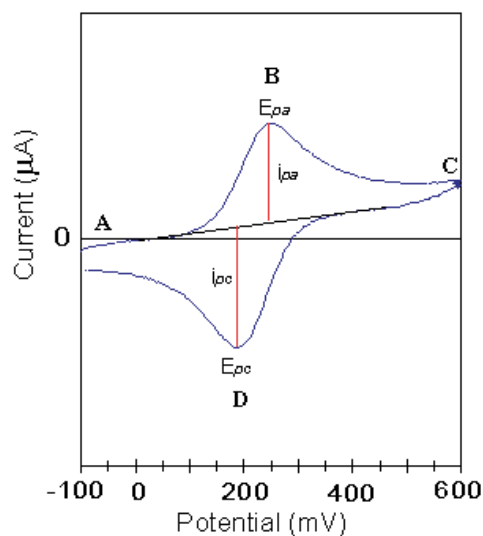


Figure 5.17: Schematic diagram of a cyclic voltammogram (taken from [75]).

The potential difference between the reduction and oxidation peaks is theoretically 59 mV for a reversible reaction. In practice, the difference is typically 70-100 mV. Larger differences, or nonsymmetric reduction and oxidation peaks are an indication of a nonreversible reaction. These parameters of cyclic voltammograms make CV most suitable for characterization and mechanistic studies of redox reactions at electrodes.

Fig. 5.18 shows the stationary current density vs. cell potential for cathodic reduction (intercalation) of TaS_2 (Pt anode) in 0.5 M pyridine hydrochloride electrolyte in aqueous buffer pH = 6.2 [76]. A current of 2 mA at 2.0 V is applied for one hour for the intercalation of pyridine into TaS_2 . Red arrow in the figure indicates the voltage at which hydrogen gas evolution is observed at the cathode. The potential and current scales have reverse sign in fig. 5.18 (old convention) as compared to the data obtained in our experiments (modern convention).

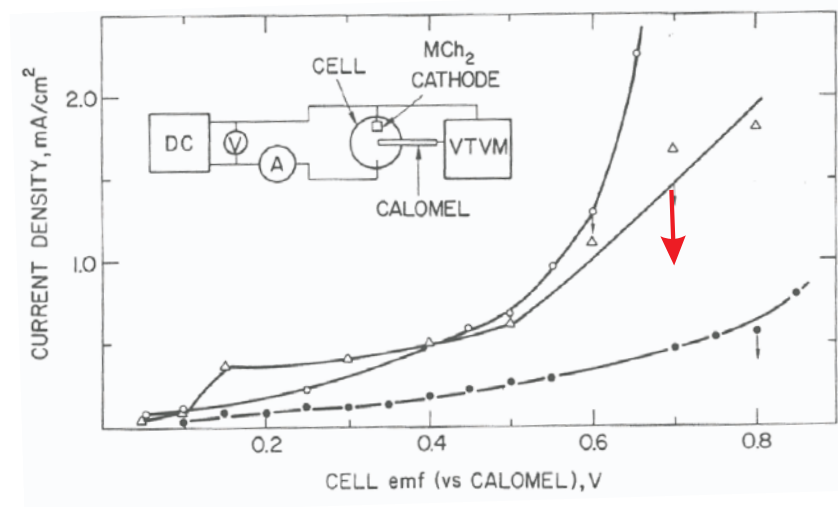


Figure 5.18: Plots of charge density vs. absolute value of cell potential for MX_2 cathode in 0.5 M PyHCl solutions (\circ , NbSe_2 and \triangle , TaS_2 in aqueous buffer pH = 6.2; \bullet , TaS_2 in ethanol). Red arrow indicates the hydrogen evolution potential in aqueous media. The potential and current scale have reverse sign (old convention) as compared to the data obtained in our experiments (modern convention). Insert shows a schematic of the electrolysis circuit (taken from [76]).

5.2 In-situ Scanning Tunneling Microscopy (STM)

In situ scanning tunneling microscopy in electrolyte solutions is described in several reviews [77, 78]. A small overview of the important aspects of in situ STM will be given here.

5.2.1 Tunneling Effect

Quantum mechanical tunneling is a direct consequence of the wave like properties of particles. According to classical mechanics, passage through a potential barrier higher than the kinetic energy of the particle is practically impossible. However in quantum theory the wave nature of the particle allows the electron to traverse the barrier by the so called tunneling effect.

The tunneling effect is the fundamental basis of the scanning tunneling microscope (STM) used in our experiments. The scanning tunneling microscope was invented in 1982 by Binnig and Rohrer [79]. A conducting sample and a sharp metal tip, which acts as a local probe when brought within a distance of few angstroms results in an overlap of their electronic wave functions. Electrons from the occupied sites of the tip/sample have a finite probability to tunnel through the barrier to empty sites of the sample/tip. If a tunneling voltage ("bias") is applied between tip and sample the Fermi levels shift and the tunneling probability is increased in one direction, leading to a net current ("tunneling current I ") which can be measured.

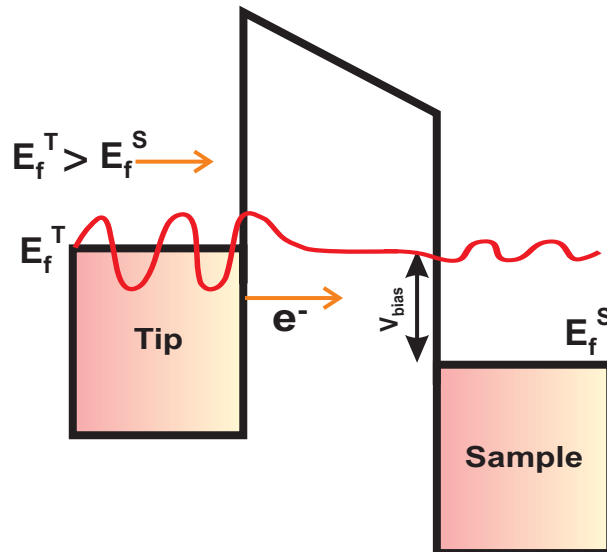


Figure 5.19: Schematic illustration of potential barrier for electron tunneling from the Fermi level of the occupied states of the tip (left side) to the Fermi level of the unoccupied sites in the sample (right side).

The situation is shown in figure 5.19. In a crude approximation, considering two planar metal elec-

trodes separated by a vacuum barrier, the tunneling current can be expressed as:

$$I \propto e^{-A\Phi^{1/2}d} \quad (5.28)$$

where d is the distance between the electrodes (in \AA)

A is a constant ($\approx 1 \text{ \AA}^{-1} \text{ eV}^{-1/2}$)

Φ is height of the vacuum barrier (in eV).

The tunneling current depends exponentially on distance between the tip and the sample. Hence it has a very high sensitivity to any change in the distance (d).

As illustrated in fig. 5.20, an STM image is obtained by scanning the tip parallel to the surface with piezodrives which allow a control in the x and y directions at a sub- \AA scale. The extreme sensitivity of the tunneling current to small variations in the z direction normal to the surface allows the measurement of the surface corrugation on the atomic scale. Two operation modes are possible depending on the settings (see fig. 5.20) :

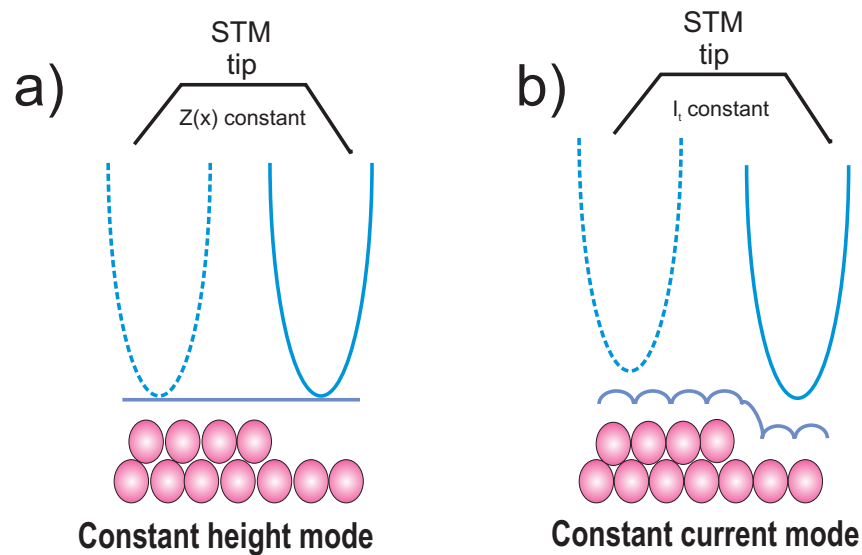


Figure 5.20: Different operating modes of scanning tunneling microscope (a) Constant height mode (CHM) and (b) Constant current mode (CCM).

- **Constant Current Mode (CCM)** i.e. image acquisition at constant current, ($z = f(x, y)$), where z is continuously adjusted over the surface to keep the current constant.

- **Constant Height Mode (CHM)** i.e. image acquisition at constant height ($I = f(x, y)$), where the current is directly recorded at each point on the surface (response time of the feedback > time for scanning lines).

While the former mode is slower and hence slow chemical processes i.e. intercalation, electrodeposition in situ can be studied, the latter mode is quite fast and finds application in the study of fast atomic processes for example atomic diffusion processes etc.

5.2.2 Electrochemical Scanning Tunneling Microscopy (EC-STM)

For in situ STM, both substrate and tip are exposed to the electrolyte and hence are susceptible to electrochemical charge transfer reactions. Unless the potentials of both are controlled properly, this can lead to arbitrary changes in the surface morphology of the surface and the tip. Furthermore, at the tip, the tunneling current can not be separated from superimposed faradaic current, which leads to the noise in the signal at small currents and makes a controlled operation impossible at larger currents. In electrochemistry, the potential control is usually provided potentiostatically by a three electrode set up with the working electrode (WE) potential controlled against a currentless reference electrode (RE) with a fixed potential and a counter electrode (CE) for the current flow. In the electrochemical environment, the STM tip acts as a fourth electrode. Its potential is controlled potentiostatically against the same reference and counter electrode as the working electrode. This setup allows independent control of the tip and sample potentials. The potential of the tip should be maintained within its electrochemical double layer region. However even if the tip potential is maintained within the double layer region, faradaic reactions can still occur which lead to an offset of tunneling current. Additionally, due to the double layer capacity of the tip exposed to the electrolyte, noise in the current signal results. Hence it is essential that most of the tip is insulated leaving only the very end of the tip exposed to the electrolyte.

The in-situ STM used for the experiments described in the following chapters is a home made version. A schematic representation of the instrument is given in fig. 5.21.

In this instrument the approach of the tip to the surface is done with the combination of a micrometer screw (M) and a lever (W). The motor driven screw (M) moves the tip closer to the sample (WE) in the electrochemical cell (C). During the approach the Z-piezo is expanded. As soon as the tunneling current

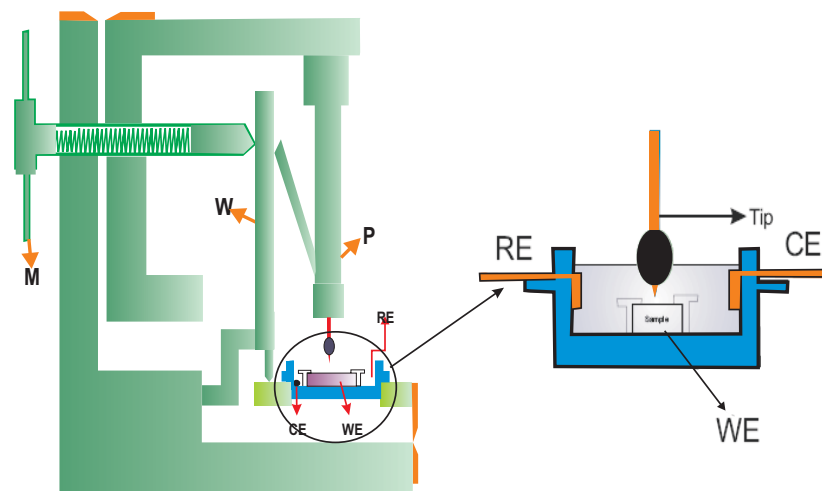


Figure 5.21: Schematic representation of the (a) home made in-situ STM and (b) electrochemical cell used in STM experiments.

flows, the motor is stopped and a feedback loop keeps the distance between the tip and the electrode constant. In the tunneling mode the tip can be precisely moved via a piezoelectric drive (P), which is a single-tube three dimensional scanner. In the experiments described here only imaging in the constant-current mode is performed. The z-motion during scanning is displayed in real time on a monitor, allowing imaging of the surface.

5.3 Atomic Force Microscopy (AFM)

The atomic force microscope (AFM) or scanning force microscope (SFM) was invented in 1986 by Binnig, Quate and Gerber [79]. Similar to other scanning probe microscopes, the AFM raster scans a sharp probe over the surface of a sample and measures the changes in force between the probe tip and the sample. Fig. 5.22 illustrates the principle of operation for an atomic force microscope. A cantilever with a sharp tip is positioned above a surface. Depending on this separation distance, long range or short range forces will dominate the interaction. This force is measured by the bending of the cantilever by an optical lever technique where a laser beam is focused on the back of a cantilever and reflected into a photo detector. Small forces between the tip and sample will cause less deflection than large forces. By raster-scanning the tip across the surface and recording the change in z as a function of position (F kept constant), a map of surface topography and other properties can be generated.

The AFM is useful for obtaining three-dimensional topographic information of insulating and con-

ducting structures with lateral resolution down to 1.5 nm and vertical resolution down to 0.05 nm. These samples include clusters of atoms and molecules [80], individual macromolecules [81], and biological species (cells, DNA, proteins) [82]. Unlike the preparation of samples for STM imaging, there is minimal sample preparation involved for AFM imaging. Similar to STM operation, the AFM can operate in air and fluid environments [83]. It also can measure physical properties including elasticity, adhesion, hardness, friction and chemical functionality [84].

5.3.1 Modes of Operation for the AFM

The three general types of AFM imaging are (1) **Contact mode**, (2) **Tapping mode** and (3) **Noncontact mode**.

1. **Contact mode** is the most common method of operation of the AFM. As the name suggests, the tip and sample remain in close contact as the scanning proceeds. The term "contact" refers to the repulsive regime of the inter- molecular force curve, the part of the curve above the x-axis (fig. 5.22). Most cantilevers have spring constants between 0.01 - 1 N/m, which is less than binding energy of the atoms. One of the drawbacks of the tip remaining in contact with the sample is that large lateral forces can be exerted on the sample as the tip is dragged over the specimen. These large forces can result in deformed images and damaged samples [85, 86].
2. **Tapping mode** is another mode of operation for AFM. Unlike the operation of contact mode, where the tip is in constant contact with the surface, in tapping mode the tip makes intermittent contact with the surface. As the tip is scanned over the surface, the cantilever is driven close to its resonant frequency (hundreds of kHz). Because the contact time is a small fraction of its oscillation period, the lateral forces are reduced dramatically. Tapping mode is usually preferred to image samples with structures that are weakly bound to the surface or samples that are soft (polymers, thin films). There are also two other types of image contrast mechanisms in tapping mode:
 - **Amplitude imaging:** The feedback loop adjusts the z-piezo so that the amplitude of the cantilever oscillation remains (nearly) constant. The voltages needed to keep the amplitude

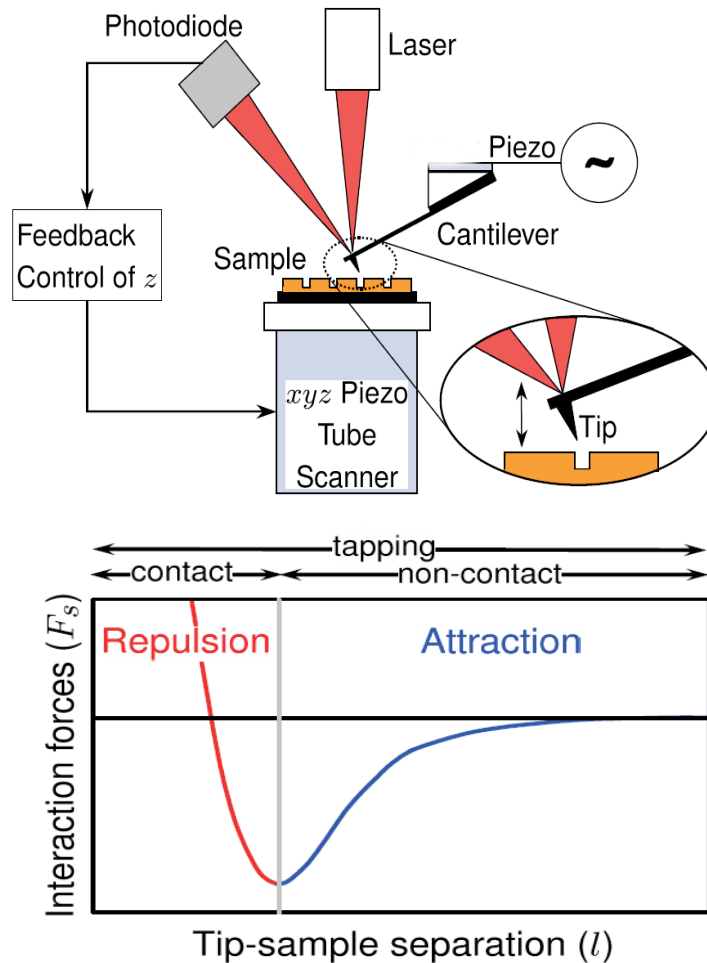


Figure 5.22: Schematics of an atomic force microscope and the force vs. tip-sample distance curve for different modes of operation taken from [86].

constant can be compiled into an (error signal) image, and this imaging can often provide high contrast between features on the surface [85, 86].

- **Phase imaging:** The phase difference between the driven oscillations of the cantilever and the measured oscillations can be attributed to different material properties. For example, the relative amount of phase lag between the freely oscillating cantilever and the detected signal can provide qualitative information about the differences in chemical composition, adhesion, and friction properties [85, 86].

3. **Non-contact mode** is a method where the cantilever is oscillated above the surface of the sample at distances such that it always remains in the attractive regime of the intermolecular force curve. The

operation of non-contact imaging is quite difficult in ambient conditions because of the existing thin layer of water on the tip and the surface. As the tip is brought close to the surface, a small capillary bridge between the tip and the sample cause the tip to "jump-to-contact" [85, 86].

The choice which AFM mode to use is based on the surface characteristics of interest and on the hardness/stickiness of the sample. Contact mode is most useful for hard surfaces; a tip in contact with a surface, however, is subject to contamination from removable material on the surface. Excessive force in contact mode can also damage the surface or blunt the probe tip. Tapping mode is well-suited for imaging soft biological specimen and for samples with poor surface adhesion (DNA and carbon nanotubes). Non-contact mode is another useful mode for imaging soft surfaces, but its sensitivity to external vibrations and the inherent water layer on samples in ambient conditions often causes problems in the engagement and retraction of the tip. Both contact as well as tapping mode AFM was used in all the experimental results presented in this thesis as copper nanowires formed on the surface of TaS₂ are quite stable as already reported by Adelung et al. [16].

5.4 Scanning Electron Microscope (SEM)

The Scanning Electron Microscope (SEM) is one of the most powerful and versatile present day material characterization tools available. It is applied to study a wide range of materials including metals, non-metals, semiconductors and biological specimens. The capabilities of the SEM and its variants extend from high resolution topographic imaging to both qualitative and quantitative chemical analysis. SEM provides a fast and easy way of analyzing a given sample with relatively simple sample preparation techniques. The first scanned electron image was produced by Max Knoll in 1935 [87]. A lateral resolution of 1-5 nm and a depth resolution of 1-10 nm have been achieved in modern SEM [88].

The interaction between the electron beam and the specimen is the basis of electron microscopy. In the scanning electron microscope (SEM), a finely focused electron beam is rastered across the surface of the specimen to form images using electron detectors and cathode ray tubes. For details reader are referred to the review [89].

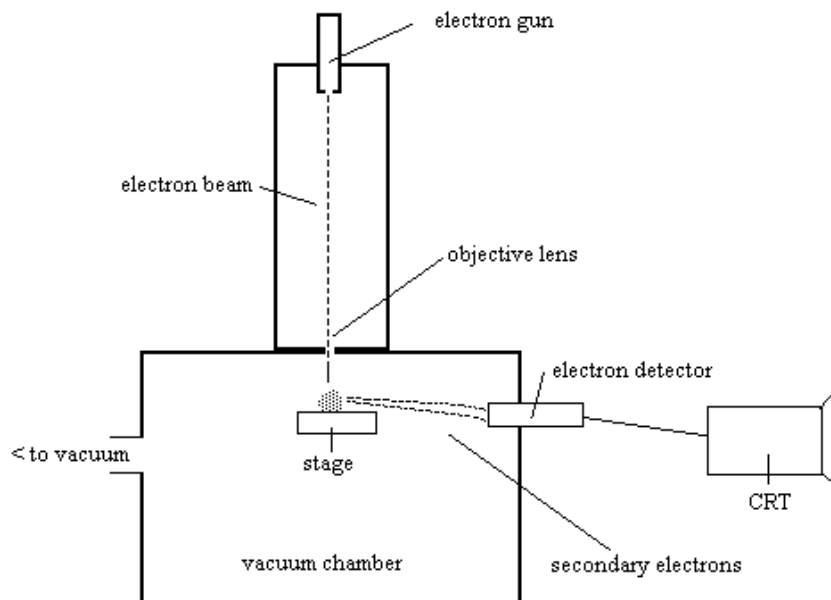


Figure 5.23: Schematic diagram of a scanning electron microscope (taken from [20]).

Fig. 5.23 shows a schematic diagram of a scanning electron microscope (SEM). Electrons from a filament in an electron gun are focused on the specimen in a vacuum chamber. The beam forms a line that continuously sweeps across the specimen at high speed. This beam irradiates the specimen which in turn produces a signal in the form of either x-ray fluorescence, secondary or backscattered electrons.

5.5 Experimental Conditions

5.5.1 Sample Surface Preparation

The TaS_2 crystals used in this work were grown by chemical vapor transport with iodine as transport agent. During the growth period of 25 days a temperature gradient of $>750^\circ\text{C}$ was applied. The metastable 1T-polytype was obtained by rapidly quenching of the quartz ampoules from growth temperatures down to the room temperature.

For electrochemical measurements TaS_2 samples were prepared by connecting a copper wire to the back side of the sample using conducting glue. The sample was then covered from the back side by apiezon wax leaving only the basal (0001) plane of the sample free (see fig. 5.24). TaS_2 crystals undergo spontaneous oxidation in air. Therefore in order to avoid contamination of the crystals, new crystal

surfaces were prepared each time, by the cleavage of some basal layers using scotch tape prior to the cyclic voltammogram measurements.



Figure 5.24: Picture of a TaS_2 sample connected by a copper wire and covered by apiezon wax, used for cyclic voltammetry experiments.

Since the samples used in all our experiments were having very small dimensions (area $\approx 4\text{-}6\text{ nm}^2$ and thickness $\approx 0.02\text{ mm}$), mounting into the electrochemical STM cell was quite difficult and therefore carried out in a specially designed electrochemical cell made of kel-f material. A computer aided design (CAD) of the electrochemical cell is shown in fig. 5.25. The sample, which was clamped by platinum plates and kel-f screws, served as the working electrode. The external connection to the working electrode (WE) was made by a platinum wire. Another platinum wire and a palladium wire loaded with hydrogen served as counter and reference electrode, respectively (see fig. 5.25).

5.5.2 Preparation of Tunneling Tips, Electrolytes and Reference Electrode.

Tunneling tips were electrochemically etched from 0.3 mm diameter polycrystalline tungsten wire (Wolfram Industries). In this method a piece of W-wire is pulled vertically through a gold wire (1 mm dia.) loop of $\approx 12\text{ mm}$ diameter. On this loop an electrolyte film consisting of 2 M NaOH is suspended. Then a DC-voltage of 3.5 V is applied between the W- and Au- wire. The tungsten wire served as anode in the current circuit. Thus, it is etched in the NaOH lamella and a constriction is formed until the lower part drops down (see fig. 5.26). At that moment, the current flow is interrupted within $< 0.1\text{ s}$ to prevent further etching of the hanging tip. Only the upper part of the wire was used, although through the

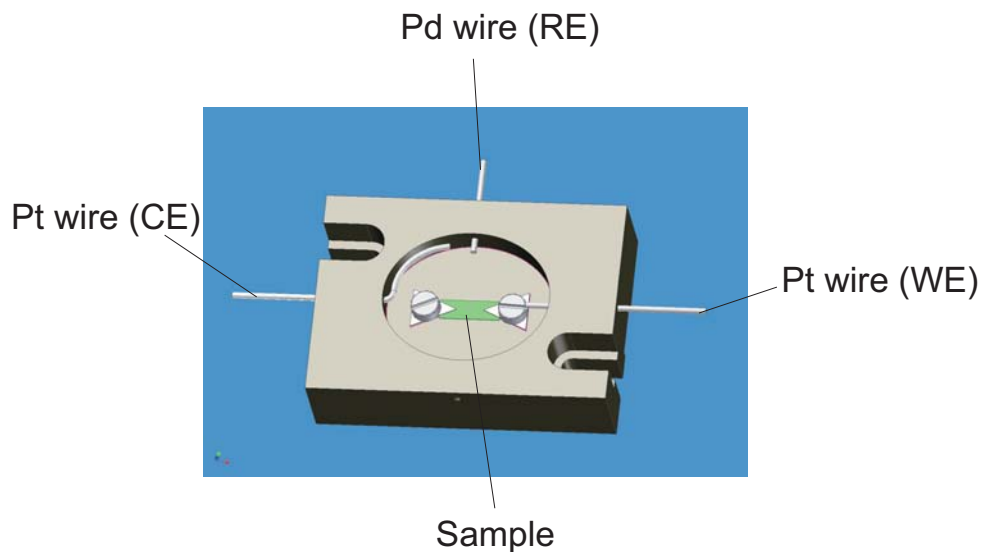


Figure 5.25: Top side view of computer-aided-design drawing of the specially designed electrochemical cell used in our STM experiments.

constriction on the lamella both parts of the wire form tips. Directly after the wire breaks, it is rinsed thoroughly with ultra pure water.

Since in in-situ STM experiments, the tip works as a fourth electrode, electrochemical reactions also occur at the tip, resulting in a higher Faraday current, which ultimately overlap the tunneling current. In order to minimize this current, so that the signal obtained during experiments will only involve that for tunneling currents, isolation of the tips to the maximum is necessary. Therefore, the tips used in all our experiments were isolated by apiezon wax (company Plano). The isolation was done in the following way. The tip was mounted on a movable micrometer screw (capable of moving in 3 dimensions) holder and then moved into the center of a horizontal platinum ring (see fig. 5.27). In order to heat both micrometer screw tip holder and the platinum ring independent of each other, a power supply was connected to both of them. A typically large piece of wax was mounted into the tip by adjusting the power supply to make the wax viscous. By moving the tip in all the three directions using micrometer screw holder within the ring, isolation was carried out until only a very small fraction of the tip ($0.01 \mu\text{m}$) was left uncoated. The tips were then mounted on the STM head and kept there for 2-3 hours in order to reduce the mechanical stress associated with the tip and the tip holder of the STM head. Most of the tips obtained in this way worked fine in our experiments.

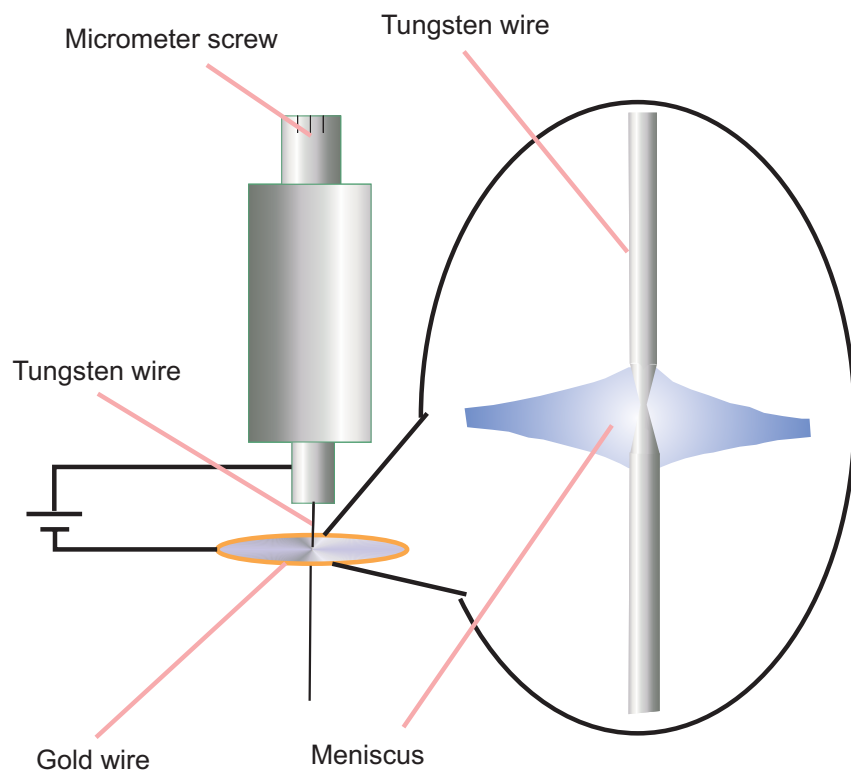


Figure 5.26: Schematics showing preparation of tungsten tips. For description see text.

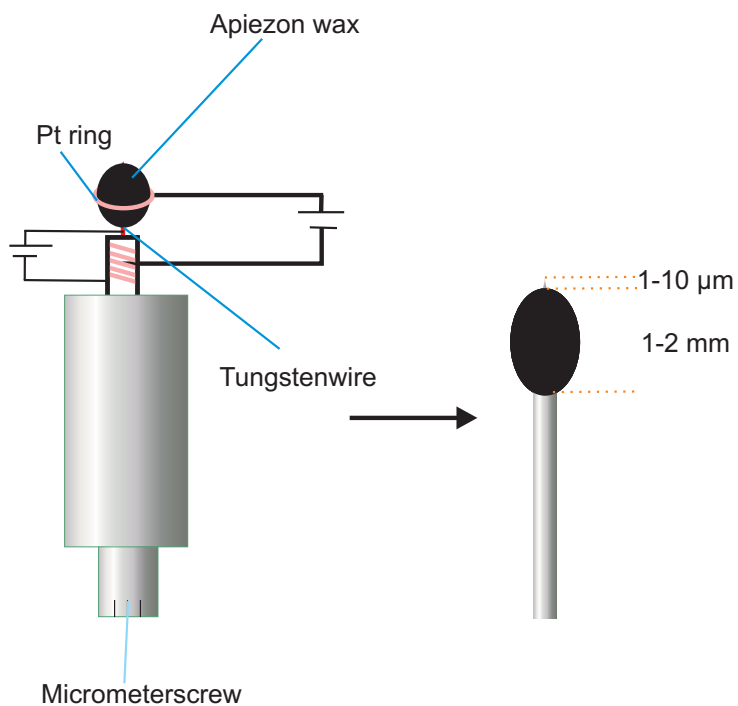


Figure 5.27: Schematics showing coating of tungsten tips. For description see text.

The electrolytes were prepared using the highest grade chemicals commercially available. In detail these are pyridine (fluka $\geq 99.8\%$ purity), octylamine (fluka $\geq 99.5\%$ purity), suprapure H_2SO_4 (Merck) and CuSO_4 (Merck) . Ultra pure water (Elga lab water) was used in all our experiments.

Before use, glassware and STM-cells were soaked overnight in a freshly prepared $\approx 2:1$ mixture of conc. H_2SO_4 and 30% H_2O_2 to oxidize all organic impurities as well as metal contaminants. After this acid bath they were rinsed thoroughly with ultra pure water and finally cooked for a few hours in boiling ultra pure water. The ultra pure water was exchanged several times during the cooking process.

For our measurements different standard reference electrodes were used. In cyclic voltammogram measurements, a standard calomel electrode (SCE) was used. In STM measurements a Pd wire (- 0.3 V vs. SCE) loaded with hydrogen was used. Such a reference electrode can be prepared by applying a voltage of 2 V to the Pd wire (Pd as cathode, Pt as anode) for half an hour in 10 mM H_2SO_4 solution. Nevertheless, all potentials reported here are quoted against the potential of the standard calomel electrode (SCE).

6 Results on organic molecule intercalation into TMDCs

The results of intercalation in different dichalcogenides used in our experiments are discussed in this section. TiSe_2 was used in the beginning of our studies and intercalation of organics e.g. hexylamine was used as intercalate. But due to experimental difficulties e.g. surface oxidation of TiSe_2 in the used electrolyte, electrochemical STM measurements failed. Due to this reason NbSe_2 samples were later employed in our experiments. Most of the NbSe_2 samples obtained by vapor transport method were quite small (diameter ≤ 2 mm, thickness ≈ 0.1 mm) and could not be mounted and contacted by conductive glues in the electrochemical environment due to contamination problems. Hence the primary requirement was to obtain large TMDC single crystals with diameters of at least 3 mm, but these were difficult to obtain. This in particular prevented further systematic studies of NbSe_2 . Nevertheless those preliminary results of electrochemical as well as STM measurements which were carried out, are presented below. Finally single crystals of TaS_2 were employed in our studies. Fortunately, the TaS_2 crystals obtained by chemical vapor transport method were large enough (diameter ≥ 3 mm, thickness ≈ 0.3 mm) to mount in our electrochemical cell for STM studies and hence most of the work that is described below are attributed to single crystals of TaS_2 .

6.1 1T- TaS_2 in Air

The bare surface of TaS_2 single crystal in air exhibit characteristic features like all other transition metal dichalcogenides (TMDCs). Fig. 6.28a shows an STM image ($154 \times 189 \text{ nm}^2$) of a freshly cleaved TaS_2 surface. Atomically flat terraces along with step edges and pits on the surface can be clearly observed. Such defects often observed in TMDCs, are probably due to the cleaving process. Fig. 6.28b shows the height distribution along a scan line in fig. 6.28a. The step height is ≈ 0.56 nm indicating a monolayer step which is in good agreement with the literature (step height ≈ 0.58 nm [90]) within the experimental error. Fig. 6.28 c, d represents the structure of a contaminated surface of the TaS_2 sample after 10 minutes (taken from [91]) and after several days in our experiment, respectively. Extensive surface degradation due to oxidation of TaS_2 can be observed in both cases. The defects on oxidized TaS_2 (fig. 6.28d) extend over large areas of the sample and are several layers deep. Surface oxidations leading to degradation of TMDCs have already been reported [92].

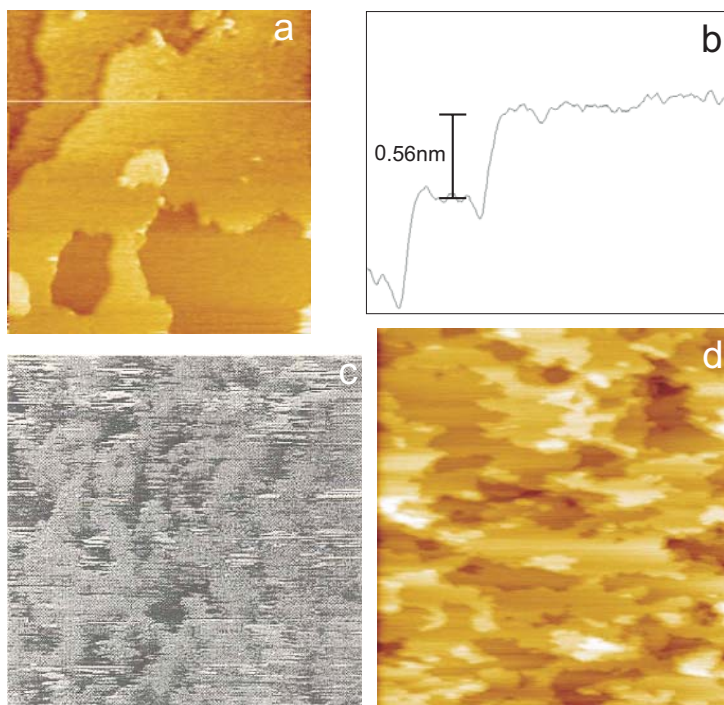


Figure 6.28: STM images of $1T\text{-TaS}_2$ in air (a) freshly prepared surface ($154 \times 189 \text{ nm}^2$), (b) step height along the cross section in fig. 6.28a, (c) 10 minutes after cleaving in air ($250 \times 250 \text{ nm}^2$) (taken from [91]) and (d) after several days ($266 \times 276 \text{ nm}^2$).

6.2 $1T\text{-TaS}_2$ in Pure H_2SO_4

In this section the surface structure of $1T\text{-TaS}_2$ in pure H_2SO_4 is discussed. The surface structure was found to be quite stable in the entire potential range. Before discussing the results, a short review of all the previous work is given. For details, readers are referred to the literature [2, 93–95, 99].

6.2.1 Literature Review

The uptake of hydrogen by layered dichalcogenides was first observed originally during the cathodic reduction of TaS_2 in 0.1 N HCl. The hydrated product $\text{H}_x\text{TaS}_2 \cdot x\text{H}_2\text{O}$ exhibited a larger interlayer spacing of $\approx 5 \text{ nm}$ but was unstable [93]. Later investigations established the existence of the nonhydrated phase of H_xTaS_2 [94, 95], which show interlayer spacing close to the parent lattices. It is important to note that while H^+ ions fails to intercalate by cathodic reduction of $1T\text{-TaS}_2$ in dilute and concentrated H_2SO_4 acids [96–98], it can be readily intercalated by cathodic reduction of $1T\text{-TaS}_2$ to the hydrated alkali phases $\text{A}^+(\text{H}_2\text{O})[\text{TaS}_2]^-$ and subsequent treatment with aqueous HCl/ SO_2 . The layers collapse

instantaneously to an inter layer spacing of $\approx 6 \text{ \AA}$ and hydrogen bronze $\text{H}_{0.2}\text{TaS}_2$ is obtained [2]. High resolution microscopic studies of H_2 intercalation in TMDCs do not exist. However an STM, AFM adsorption study of gaseous atomic H_2 on to the graphite surface demonstrates the formation of defects such as bumps and etch pits during intercalation [99].

Where as all these studies are related to chemistry of preparation and characterization by spectroscopic methods, no real nanoscopic structural investigation has been carried out up to date. In the following section the electrochemical characterization and in situ study of 1T-TaS_2 in pure H_2SO_4 solution are discussed.

6.2.2 Cyclic Voltammetry

Prior to the STM measurements the stability and surface structure of 1T-TaS_2 in supporting electrolyte H_2SO_4 at pH 3 was characterized by cyclic voltammetry. Fig. 6.29 shows a cyclic voltammogram of 1T-TaS_2 in H_2SO_4 at pH 3 with a scan rate of 20 mVs^{-1} . In the potential region between 0.1 V to -0.7 V only a low constant current caused by recharging of the double layer capacity was observed. At potentials below -0.7 V hydrogen evolution indicated by higher current is generally observed. The absence of any oxidation/reduction peak is a clear indication of the absence of any faradic process. X-ray studies by Murphy [94], Riekel [95], Schöllhorn [96], Subba rao [76] already shown that intercalation of H^+ ions in 1T-TaS_2 does not occur by cathodic reduction from concentrated as well as aqueous solution of H_2SO_4 .

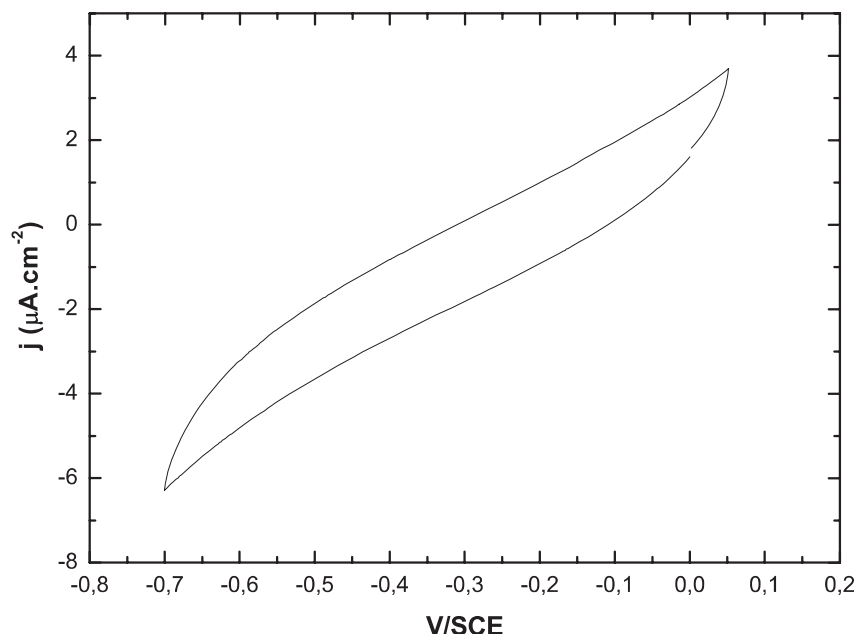


Figure 6.29: Cyclic voltammogram of 1T-TaS₂ in H₂SO₄ solution at pH 3 (scan rate 20 mV/s) showing only a double layer recharging.

6.2.3 STM Study

The series of STM images in fig. 6.30 shows the surface characteristics of 1T-TaS₂ in H₂SO₄ at pH 3 in the entire cathodic potential regime between 0 V to - 0.7 V. As found in cyclic voltammogram, the surface stability in the entire cathodic regime can be clearly observed in STM images. Fig. 6.30a recorded at - 0.22 V shows the characteristic morphology with large atomically flat terraces separated by step edges. Often pits and islands are observed which seems to be caused by the cleaving process. No structural change was observed after keeping the potential at - 0.44 V and at - 0.68 V for 8 and 14 minutes, respectively (see fig. 6.30b, c). No step flow etching, island formation or change in step height was observed during this potential change. Potentials lower than -0.7 V resulted in the hydrogen evolution and hence STM imaging quality also deteriorated (see fig. 6.30d). The absence of step flow etching in 1T-TaS₂ is in contrast to the observation by Yamaguchi et al. [91], where etching was observed under UHV conditions. The latter observation is possibly due to the higher tunneling current (0.7 nA) applied in the experiments. The presence of water also significantly lowers the energy barrier in electron tunneling [100].

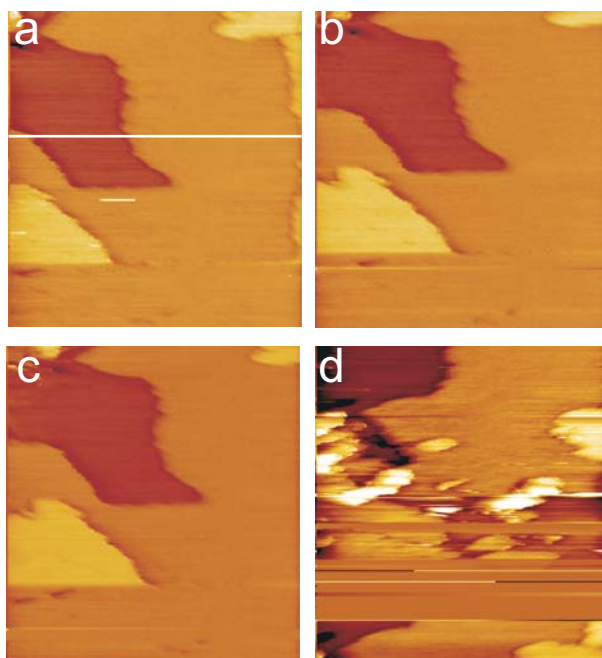


Figure 6.30: Sequences of in-situ STM images showing the morphological stability of 1T-TaS₂ in pure H₂SO₄ solution at pH 3 (a) Showing surface morphology in the double layer region at - 0.22 V and after keeping the potential at (b) - 0.44 V, (c) - 0.68 V for 8 and 14 minutes showing the stable morphology in the entire cathodic potential regime and (d) at - 0.8 V showing surface instability due to hydrogen evolution (270 x 280 nm², I_r = 0.2 nA).

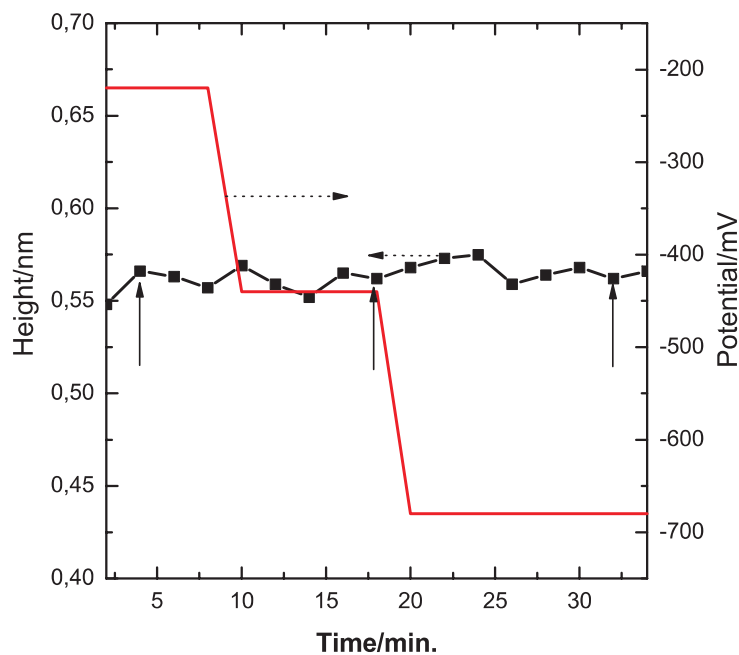


Figure 6.31: A plot of step heights (black line) and potential (red line) vs. time. Step heights were measured along the white line (see fig. 6.30a) for all the images (partially shown in fig. 6.30), showing almost a constant step height over the entire potential regime. Solid black arrows indicate the images (a, b, c) shown in fig. 6.30.

A plot of step height change and potential vs. time for all the images in the above experiment (partially shown in fig. 6.30) is shown in fig. 6.31. Measured step heights across a scan line in all images in the experiment are $\approx 0.56 \pm 0.02$ nm, which is in good agreement with monolayer step height of 1T-TaS₂ [90]. The absence of any morphological change as well as a constant step height over the entire potential regime from - 0.22 V to - 0.7 V is a clear indication that H₂SO₄ does not intercalate in 1T-TaS₂ which is in agreement with literature [76, 94, 95].

6.3 Amine Intercalation in Transition Metal Dichalcogenides

This section describes the surface morphology of different dichalcogenides studied in amine containing H_2SO_4 at pH 3. Before discussing the results, a short review of all previous studies are discussed and for details references are given.

6.3.1 Literature Review

Intercalation in TaS_2 with n-alkylamines, $\text{C}_n\text{H}_{2n+1}\text{NH}_2$ was first reported by Gamble et al. [23] in 1971. A complete series of samples with $n = 1$ to 18 was prepared by direct reaction with amine or amine in benzene solution for $n > 12$ at 25°C for 30 days. Studies on direct thermal intercalation of amines in transition metal dichalcogenides (TaS_2 , TiS_2 , NbS_2 etc.) are also reported [101–103], where aqueous amines are heated with powder samples in glass tubes under a temperature of $150\text{--}200^\circ\text{C}$. The reaction time was around 3–10 days. Indirect methods are also reported where dichalcogenides were preintercalated with ammonia or hydrazine and then reacted with amines with changing lengths up to $n = 9$ or 10 [101–103]. Complete reaction in such cases was observed at temperatures below 100°C within hours. Compounds with chain lengths > 10 were prepared by displacement reactions of amine intercalation compounds of lower carbon numbers. For a complete list of amines intercalated in to TaS_2 readers are referred to the review by Levy [1]. First electrochemical intercalation of amine was reported by Whittingham [93]. Tri-methyl amine was intercalated in TaS_2 on decomposition of a solution of tri-methyl ammonium chloride giving a lattice expansion of 0.963 nm. In addition, electrochemical intercalation of ammonia [93], hydrazine, guanidine, aniline [76], hexylamine [104] into transition metal dichalcogenides have also been reported. Staging in case of amines do not occur whereas stoichiometric phases can be prepared. Stoichiometric phases, prepared by thermal intercalation of octylamine in TaS_2 , leads to the formation of $\text{TaS}_2(\text{octylamine})_{1/2}$ in air with an interlayer expansion to 1.82 nm, corresponding to a bilayer tilted at 48° with respect to the c-axis direction, whereas under vacuum the stoichiometry decreased to $\text{TaS}_2(\text{octylamine})_{1/4}$ with interlayer expansion of 0.407 nm, indicating a parallel orientation of octylamine [33]. Similarly stoichiometric phases of electrochemical intercalated hexylamine amine into NbS_2 , leading to the formation of $\text{A}_x\text{H}_2\text{O}_y\text{NbS}_2$ ($x \approx 0.11$ and 0.14 , $\text{A} = \text{Amine}$), are also reported. Changes in the physical properties, for example the critical temperature of superconductivity [23], as

well as internal friction during intercalation of amines [105] are also reported. Fig. 6.32 shows the changes in superconducting temperature as well as theoretical variation in layer separation for TaS₂ samples intercalated with different alkyl amines.

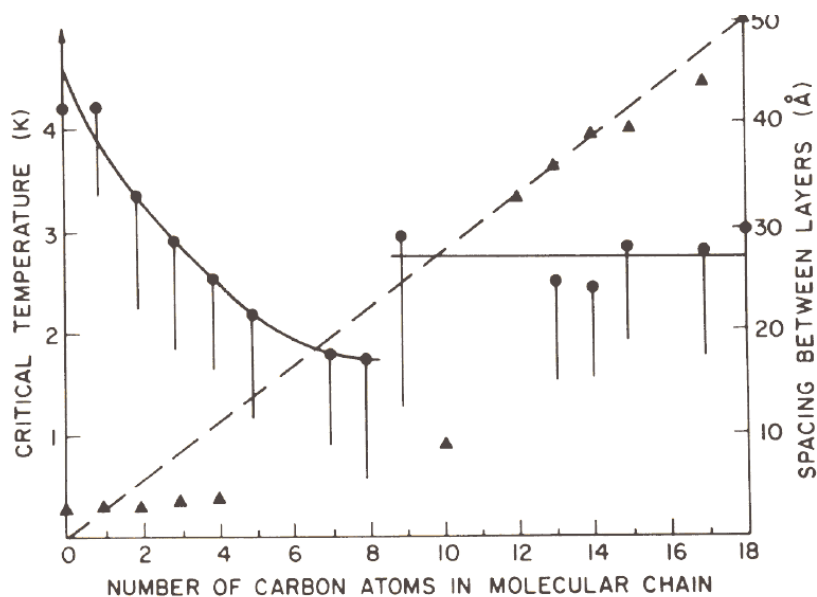


Figure 6.32: Increase in interlayer spacing (▲) and onset of temperature for super conductivity (●) as a function of n in $C_nH_{2n+1}NH_2$ for the n -alkylamine intercalation compounds of TaS₂. (taken from Gamble et al. [23]).

A comparison of theoretical as well as experimental c -axis variation produced by a homologues series of n -alkyl amine complexes in TaS₂ is shown in fig. 6.33 [106]. The observed data (○) are in excellent agreement with the calculated results (●) for chain orientations of 90° and 56°.

Three regions can be distinguished in the plots of interlayer spacing (d) vs. the number of carbon atoms in the alkyl chain (n_c).

- Short chain derivatives ($n_c = 1-5$) where δ (relative increase in d) is almost independent of chain length and amounts to 3.9 Å., corresponding to the van der Waals diameter of carbon oriented with the planes of the C-C bonds parallel to the TaS₂ (shown in fig. 6.32).
- Derivatives with medium chain length ($n_c = 6-11$), the δ value increases nearly linearly with n_c i.e. 2.5 Å/C atom which is explained by the arrangement of alkyl chains in bilayers with the chain axis tilted through an angle of 56° against the TaS₂ layers. In case of octylamine the tilting angle is 48° [33].

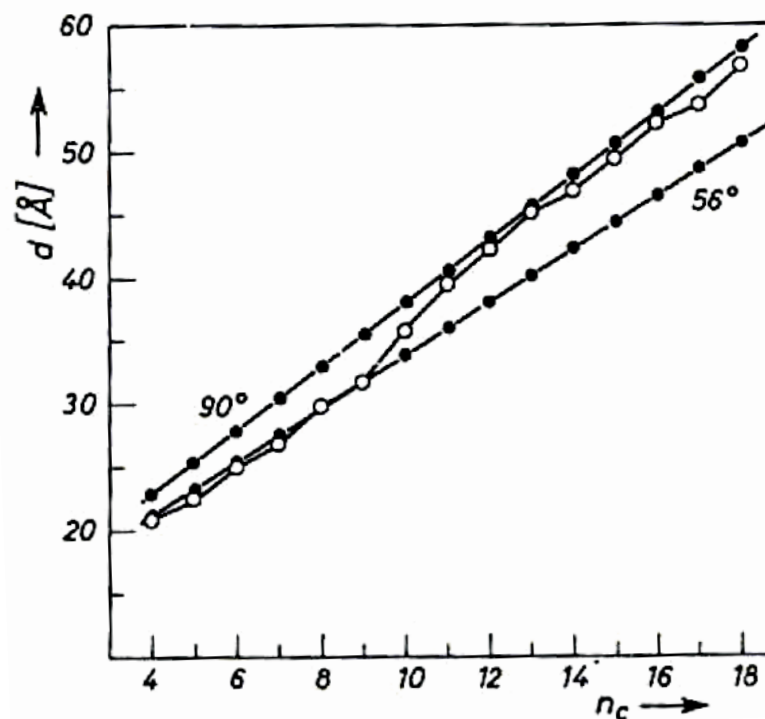


Figure 6.33: Change in interlayer spacing as a function of the number of carbon atoms in the n-alkyl amine intercalation compounds of TaS₂. The observed data (○) are compared with the calculated results (●) for chain orientations of 90° and 56° (for description see text) (taken from Schöllhorn et. al. [106]).

- Long chain derivatives ($n_c \geq 12$) where δ increases by more than 2.5 Å/C atom and the tilting angle slowly increase to 90° indicating an arrangement perpendicular to the TaS₂ layers.

A general formula for determining c axis separation in amine intercalated TaS₂ was given by Schöllhorn [106].

$$d = d_{host} + 2[(n - 1)1.26 + 1.25 + 1.5 + 2.0] \text{Å} \quad (6.29)$$

where d and d_{host} are the c-axis spacing of the intercalation compound and the host lattice, respectively, n is the number of carbon atoms, 1.26 Å is the increase in the chain length per -CH₂-, 1.25 Å accounts for the C-N distance, 1.5 Å and 2 Å are the van der Waals radii of -NH₂ and -CH₃.

Based upon the above discussed orientation of intercalated amines different models are proposed (see fig. 6.34). Alkylamines with carbon number $n < 4$ are arranged in parallel orientation (fig. 6.34a) where as with carbon number > 10 , the arrangement is perpendicular to the TaS₂ layer (fig. 6.34c). The

alkylamine with carbon number $n = 4$ to 9, amines still forms a bilayer but lies tilted at an angle to the c -axis direction (fig. 6.34b).

The nature of interaction between amine and TMDCs has been interpreted in terms of a charge transfer which arise by sigma donation from the lone pair of nitrogen atom of amine molecule to the vacant d orbital (conduction band) of TMDCs [2].

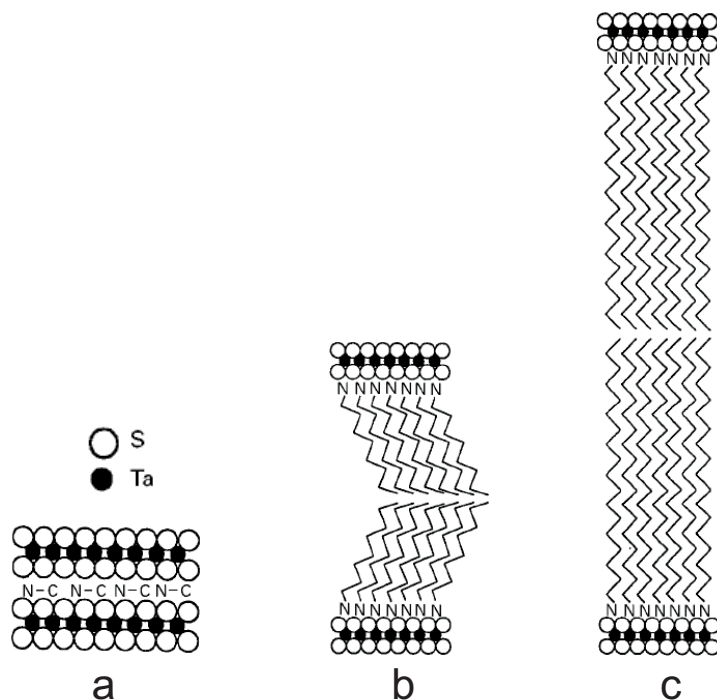


Figure 6.34: Structural models of orientations of different amines in amine intercalated TaS₂ (a) Methylamine laying parallel (b) Octylamine laying as bilayers at an angle 48° and (c) Octadecyl amine laying as bilayers perpendicular to 1T-TaS₂ layer (taken from [105]).

All the studies described above are related to the chemistry of preparation and characterization by spectroscopic methods. The main motivation of the present study comes from the facts that, no real nanoscopic structural investigation of intercalation of TMDCs has been done up to date. In the following section the electrochemical characterization and in situ study of 1T-TaS₂ in H₂SO₄ solution containing octylamine are discussed.

6.3.2 Cyclic Voltammetry

Prior to the STM measurements the stability and surface structure of all the TMDCs studied in this thesis were characterized by cyclic voltammetry. Fig. 6.35a shows continuous cycles of a cyclic voltammogram of TiSe_2 in 0.01 M hexylamine at pH 3 with a scan rate of 20 mVs^{-1} ramped between different potential ranges. Apart from a continuous increase in cathodic current, no clear reduction peaks are observed. The corresponding broad oxidation peaks around -0.35 V were also observed. Absence of any defined reduction peak might be an indication of an intercalation process that coincides with the H_2 evolution whereas sharp defined oxidation peaks might relate to the deintercalation process. The small variation of peak positions as well as current densities associated with different peaks might be related to the defects present inside different samples as reported for MoSe_2 sample [107] as well as failure to measure the exact area of the working electrode due to the unusual shapes of the samples. Similar problems were associated with all the chalcogenides studied in this thesis.

Contrary to the cyclic voltammograms of TiSe_2 in hexylamine, clearly defined reduction as well as oxidation peaks were observed in NbSe_2 (see fig. 6.35b). Various regions of interest in the cyclic voltammogram are

- at potential $> -0.4 \text{ V}$ where only double layer recharging is observed in octylamine-containing H_2SO_4 solution.
- reduction potential peaks at -0.5 V (1c) and -0.67 V (2c) prior to the onset of hydrogen evolution at around -0.7 V .
- oxidation potential peaks at -0.5 V (2a) and -0.25 V (1a) which corresponds to -0.68 V (2c) and -0.5 V (1c) reduction potential peaks respectively.

Clearly defined reduction/oxidation peaks at -0.67 V , -0.5 V and -0.5 V , -0.25 V might be related to the ease of intercalation/deintercalation process contrary to that of TiSe_2 .

Similar peaks were also observed for 1T- TaS_2 in octylamine-containing H_2SO_4 solution. Fig. 6.35c shows continuous cycles of a cyclic voltammogram of 1T- TaS_2 in 0.01 M octylamine at pH 3 with a scan rate of 20 mVs^{-1} ramped between different potential ranges. If the lower potential limit is restricted to values $> -0.4 \text{ V}$ only double layer recharging is observed in octylamine-containing H_2SO_4 solution,

whereas for potential scans to more negative potentials two peaks are found at -0.45 V (1c) and -0.52 V (2c) prior to the onset of hydrogen evolution at around -0.7 V. The corresponding peaks in the potential scan in positive direction are at -0.46 V (2a) and -0.25 V (1a), respectively. However, an enhanced anodic current is found in the entire double layer regime, up to the most positive potentials, indicating a slow kinetics of the anodic reaction. This behavior resembles that of a very similar system, electrochemical intercalation into the structurally related dichalcogenide 2H-NbS₂ [104], and suggests that peaks correspond to octylamine intercalation / deintercalation.

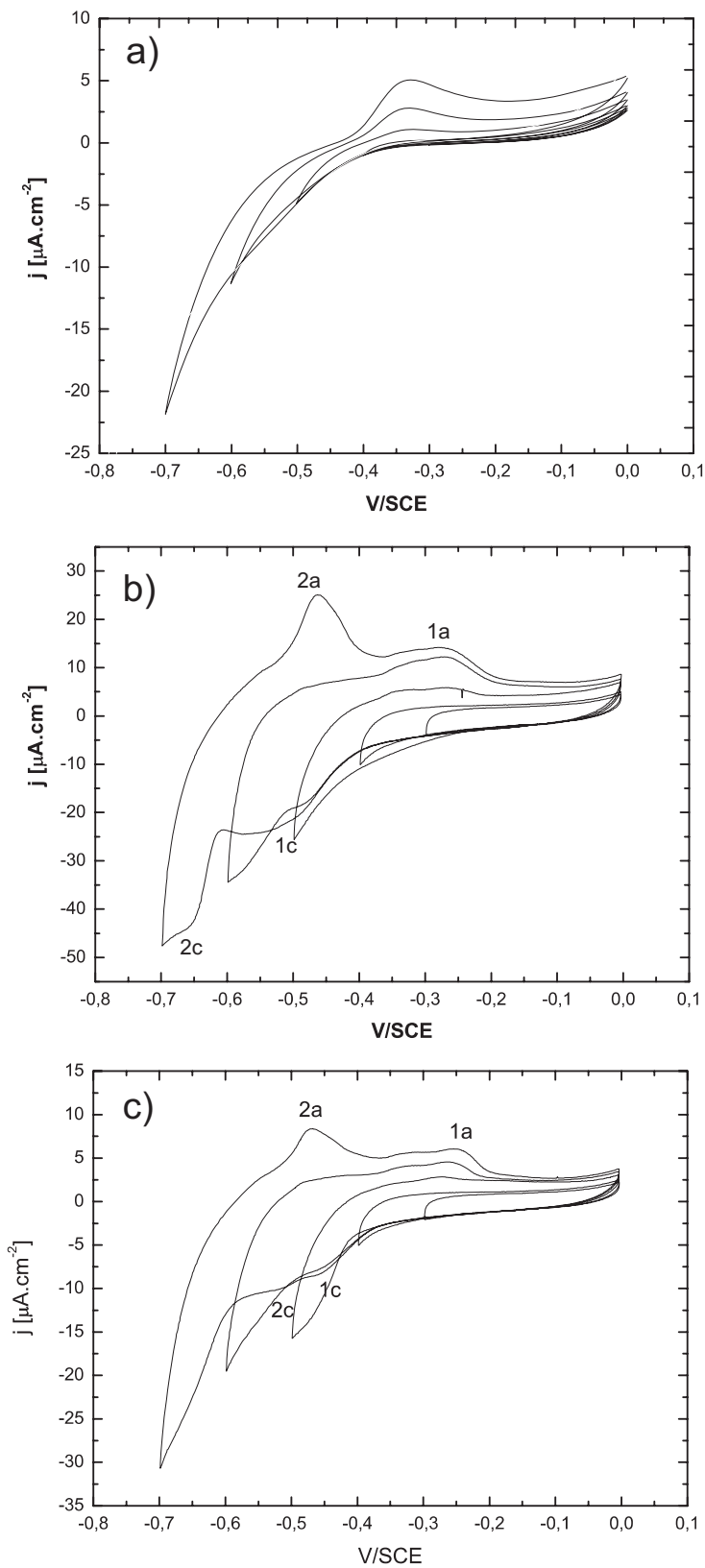


Figure 6.35: Cyclic voltammogramograms of (a) TiSe_2 (b) NbSe_2 in 0.01 M hexylamine solution and (c) TaS_2 in 0.01 M octylamine solution (pH adjusted to 3 in all cases) (scan rate 20 mV/s) (for description see text).

6.3.3 STM Studies

6.3.3.1 TiSe₂

Fig. 6.36 shows a STM image of TiSe₂ in 0.01 M hexylamine solution. Extensive surface degradation due to oxidation of TiSe₂ was observed even in the beginning of our experiments. The defects on oxidized TiSe₂ (fig. 6.36) extends over large areas of the sample and are several layers deep. Surface oxidations leading to degradation of TMDCs have already been reported [92]. This problem associated with the sample prevented further experiments and made it necessary to switch to other samples.

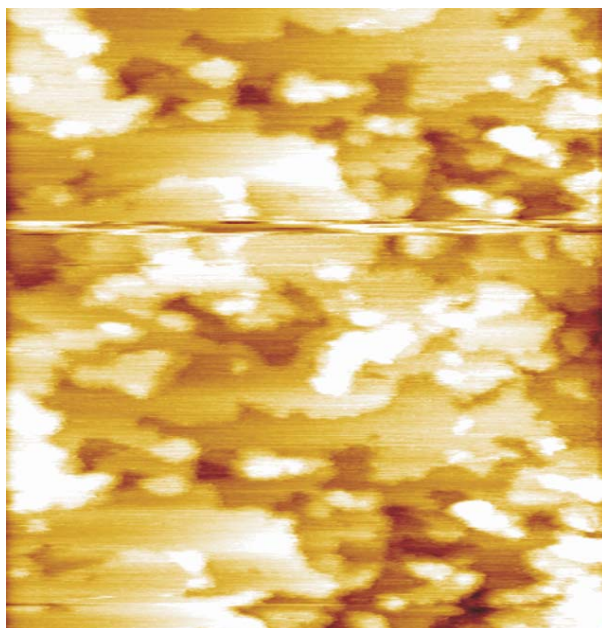


Figure 6.36: STM image showing oxidized surface of TiSe₂ in 0.01 M hexylamine solution at pH 3 (252 x 284 nm²).

6.3.3.2 NbSe₂

Fig. 6.37 shows a sequence of STM image of NbSe₂ in 0.01 M hexylamine at pH 3. Characteristic flat surfaces along with pits as defects can be clearly observed. Before proceeding to the region of any faradaic process as indicated in cyclic voltammogram, imaging of the surface in the double layer region was carried out for a longer period of time in order to check the stability of NbSe₂ surface in hexylamine solution. The substrate structure as can be seen in fig 6.37a, b was found to be stable after 8 mins. Moving on to the more cathodic regime between - 0.44 V to - 0.7 V step flow etching commences on the

basal plane. Apart from etching at defects no other change in surface morphology was observed. Similar etching has been observed in the very few experiments which had been carried out on these samples. This we attribute to the tip induced surface etching similar to that observed by Parkinson et al. under ambient conditions [108], as the applied currents in the beginning of our experiments were much higher (1 nA and higher). Apart from these etching processes, formation of islands or step height change were not observed. But nevertheless it is unwise to make any conclusion regarding intercalation process within the limited available data in our experiments as Wypych et al. [104] has already shown that NbSe₂ do undergo electrochemical intercalation with hexylamine. Failure to get reasonable crystal sizes (3 mm diameter) prevented further experiments.

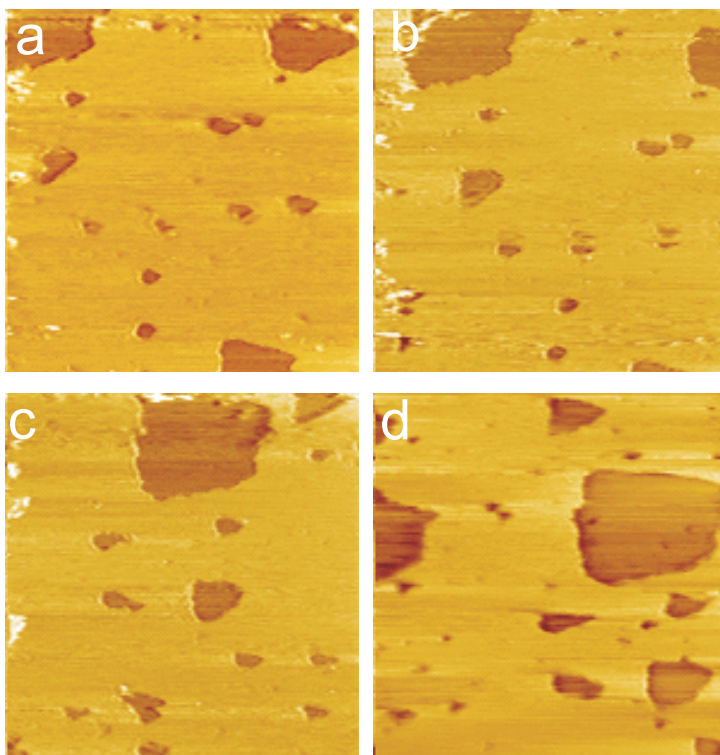


Figure 6.37: Sequences of in-situ STM images of NbSe₂ in 0.01 M hexylamine-containing H₂SO₄ solution (pH 3) showing etching on a surface exhibiting pits. Images were recorded (a) 0 and (b) 8 minutes at -0.22 V and after the potential was kept (c) 10 min. at -0.44 V and (d) 18 min. at -0.68 V (271 x 271 nm², current = 1.2 nA).

6.3.3.3 TaS₂

In studies of TaS₂ at higher tunneling currents (1 nA and higher) surface etching was often observed

even in the double layer region similar to those reported in air and under vacuum conditions [91, 108]. The following sequence of images describes these etching processes. Fig. 6.38 shows a sequence of STM

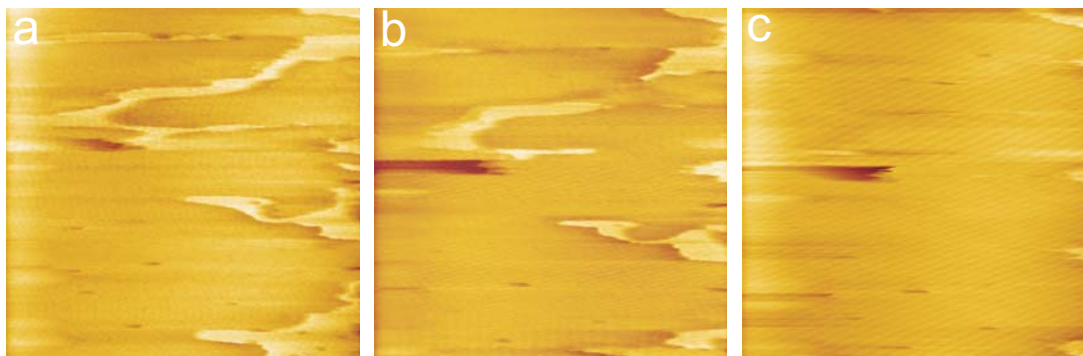


Figure 6.38: Sequences of STM images showing etching at step edges in the double layer regime of the cyclic voltammogram ($264 \times 270 \text{ nm}^2$, $I_t = 1.2 \text{ nA}$).

images of TaS_2 surface in 0.01 M octylamine at pH 3 recorded with a higher tunneling current of 1.2 nA . Large flat areas along with steps which are monolayer high were clearly observed in fig. 6.38a. Fig. 6.38b and c taken 8 and 14 minutes later at -0.22 V , show that the top surface was slowly etched away. This we attribute to the tip induced etching often observed by Parkinson [108] and Yamaguchi [91] in air and under vacuum conditions. In order to avoid this tip induced etching, a lower tunneling current was applied in the subsequent experiments and hence all the results that follow in this section are recorded with a tunneling current of 0.2 nA .

Based upon the preliminary idea we got from the cyclic voltammetry study, the STM studies correspond to the different regions of interest in the cyclic voltammogram (see fig. 6.35c). Before proceeding to the region of any faradaic process as indicated in the cyclic voltammogram, imaging of the surface in the double layer region was carried out for a longer period of time in order to check the stability of 1T-TaS_2 surface in octylamine solution. The substrate structure as can be seen in fig. 6.39a, b was found to be quite stable even after 24 min at a tunneling current of 0.2 nA . No tip induced etching was observed in this region. Moving on to more cathodic regime between -0.44 V to -0.7 V step flow etching commences on the basal plane fig. 6.39c, d. Apart from etching at defects no other changes in the surface morphology were observed. The etching process commences at the first reduction potential peak i.e. at -0.44 V and continues up to the most negative reduction potential (-0.7 V), under which all the experiments were carried out.

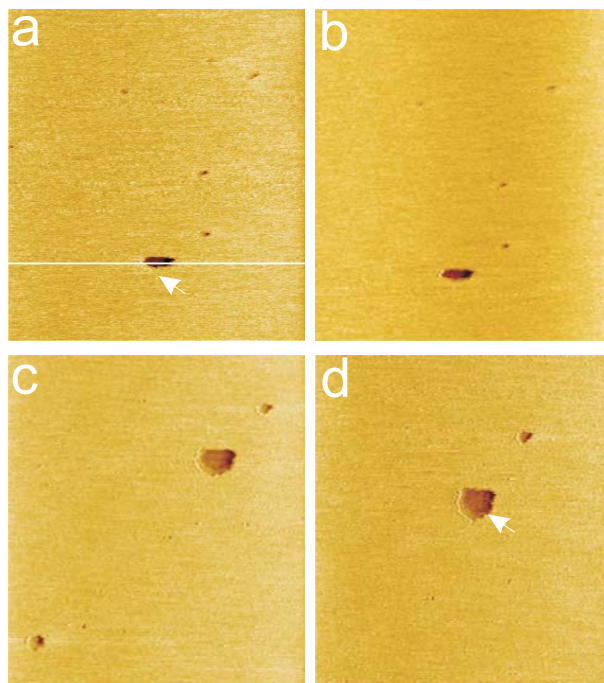


Figure 6.39: Sequence of in-situ STM images of 1T-TaS₂ in 0.01 M octylamine-containing H₂SO₄ solution at pH 3. Fig. (a), (b) showing the double layer morphology at - 0.22 V (t = 0 and 18 min.), (c) after keeping 22 min. at - 0.44 V as well as (d) after keeping the potential 48 min. below -0.6 V showing the step flow etching process (270 x 280 nm², I_t = 0.2 nA).

Similar characteristics are also observed at step edges. Fig. 6.40 shows another sequence of STM images where etching starts at the step edges. At - 0.44 V, slow etching commences which increases at - 0.52 V and lower potentials.

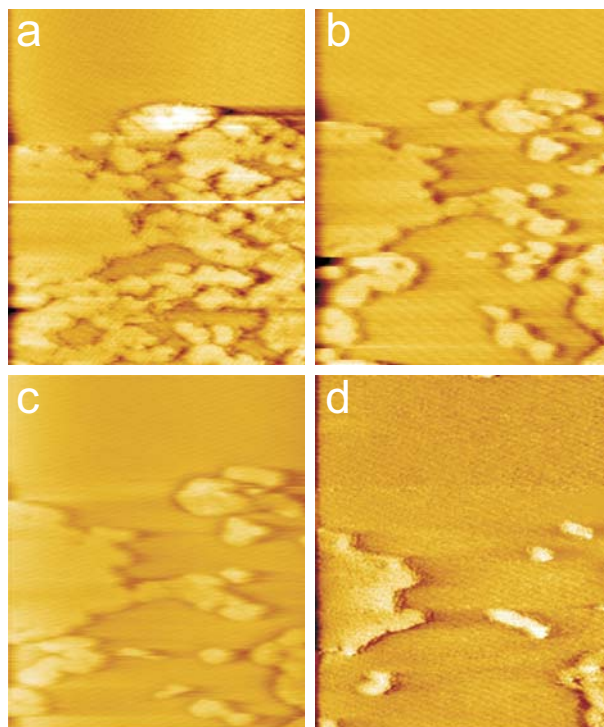


Figure 6.40: Sequence of in-situ STM images of 1T-TaS₂ in 0.01 M octylamine-containing H₂SO₄ solution (pH 3) at (a) -0.22 V, (b) after keeping 24 min. at -0.44 V, as well as after keeping potential (c) 10 min. and (d) 22 min. at -0.68 V. (270 x 298 nm², I_t = 0.2 nA).

Numerous surface etching studies of TMDCs in vacuum and air were reported and attributed to tip induced etching at higher tunneling currents [91, 108]. A perfect TaS₂ surface with threefold coordinated S atoms is a stable configuration. The stability decreases for S atoms which are coordinated in one or two fold manner i.e. at the step edges and hence can be easily etched away. In our study, etching only starts after the potential was shifted to -0.44 V. So the current etching process observed, is somewhat different from the normal tip induced etching processes already reported and is strongly potential dependent.

The plots of step height and potential change vs. time along the corresponding scan lines for fig. 6.39 and 6.40 are shown in fig. 6.41. Measured step height in the all images for fig. 6.39 and 6.40 are $\approx 0.56 \pm 0.04$ nm which is in good agreement with the monolayer step height of 1T-TaS₂ [90], indicating no amine intercalation. It is also important to mention here that at potential ≤ -0.7 V STM imaging was unstable due to the hydrogen evolution resulting in large cathodic current and ultimately tip jumps.

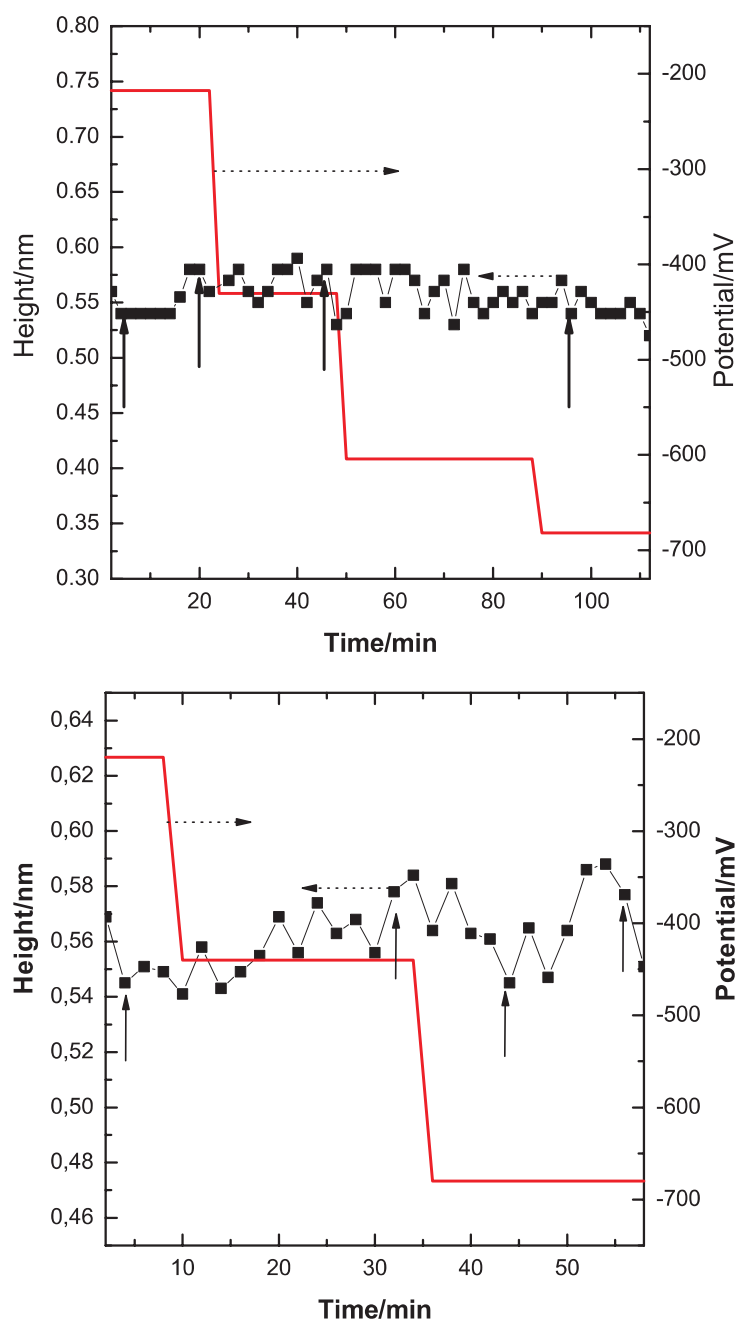


Figure 6.41: A plot of potential (red line) and measured step heights (black line) vs. time along lines (shown in fig. 6.39a and fig. 6.40a) for all the images (partially shown in fig. 6.39 and fig. 6.40) showing almost a constant step height over the entire potential regime. Solid black arrows indicate the images shown in fig. 6.39 and fig. 6.40 where as dotted black arrows directs the potential and step height change for TaS₂.

In order to have a closer look at the large scale morphological changes during intercalation of octylamine, we also performed ex-situ AFM measurements. Non-contact mode was applied due to the soft nature of adsorbed organic molecules. The sample was prepared by dipping it in an electrochemical cell (platinum as counter and calomel as reference electrode) containing 0.01 M octylamine solution at pH 3 and by applying a potential of - 0.75 V lower than the most negative reduction potential (lower than peak 2c in fig. 6.35c) for almost an hour. Then it was removed from the electrolyte and rinsed with water. Ex-situ AFM measurements were performed in air after the sample had dried.

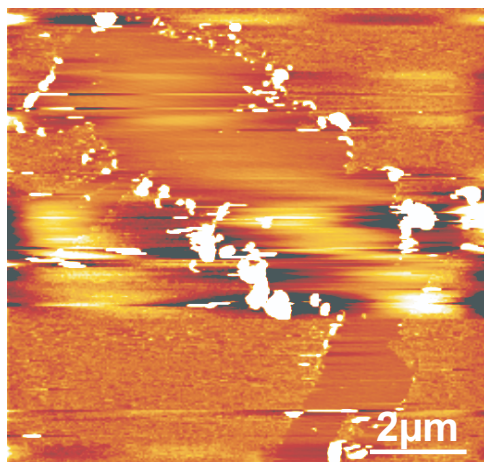


Figure 6.42: Ex-situ Atomic force microscopic image of TaS₂ surface after intercalation with octylamine.

Fig. 6.42 shows a typical AFM image of such a sample. As can be seen surface is quite rough as compared to the bare TaS₂ surface (see fig. 6.28a). The difference in appearance between the top and bottom layer might be an indication of intercalation at steps. In addition, a change in step height of ≈ 0.5 nm is also observed which might relate to the parallel orientation of octylamine. A step height increase of 0.4 nm was observed by Figueroa et al. [33] for thermal intercalation of octylamine which they attributed to parallel orientation of octylamine inside TaS₂ layer. The step edges are also decorated with islands, whose height varies between 0.6 to 1.5 nm. This is probably an indication of intercalation happening at the hydrogen evolution regime where stable STM imaging is practically not possible.

6.4 TaS_2 in Pyridine at pH 3

This section describes the surface morphology of 1T- TaS_2 in pyridine containing H_2SO_4 at pH 3. A short review of previous literature is also given below and for details readers are referred to references.

6.4.1 Literature Review

Intercalation of pyridine in TaS_2 has already been studied since 40 years. The first results on intercalation of pyridine in TaS_2 were reported by Gamble et al. [23] in 1971. The process involved either direct heating of pyridine and powdered TaS_2 in a pyrex tube under 200°C or by stirring a suspension of TaS_2 in an aqueous solution of the pyridine for a single day. Completion of the reaction was indicated by cessation of a quite remarkable swelling of the layered material and by the attainment of a constant limiting weight. The direct reaction with dry pyridine at 200°C gave a mixture of two phases of different c-axes of 1.185 nm and 1.202 nm involving two different intercalated phase products of TaS_2 [23]. However single phases can also be prepared by changing the reaction conditions [110, 111]. An indirect intercalation method of pyridine into TaS_2 was proposed by Schöllhorn et al. [112] which involves an intercalation of ammonia into TaS_2 followed by an exchange with pyridine molecules. First electrochemical intercalation was reported by Whittingham et al. [93]. It involved TaS_2 as cathode and pyridinium hydrochloride in methanol as electrolyte, ultimately leading to the formation of the phase having a layer expansion of 1.185 nm. Similar experiments in ethanol lead to the formation of the higher phase ($c = 1.202$ nm) [76]. Cathodic reduction from aqueous pyridine solutions leads to the formation of $\text{C}_5\text{H}_5\text{NH}^+_{0.25}(\text{C}_5\text{H}_5\text{N})_{0.25}[\text{TaS}_2]^{0.25-}$ as final product. For details about intercalation of pyridine and its derivatives readers are referred to [1, 2].

All the above mentioned intercalated compounds are first stage with 0.5 pyridine per TaS_2 unit in every van der Waals gap. Second stage compounds with pyridine in alternate van der Waals gaps of TaS_2 can also be prepared either by reaction of TaS_2 with a substoichiometric amount of pyridine or by reaction of TaS_2 with $\text{TaS}_2(\text{py})_{0.5}$ [23]. The stoichiometry of the intercalated complex obtained by chemical analysis for both thermal and electrochemical intercalation shows somewhat different values. A pyridine content of 0.2-0.3 mole per mole of TaS_2 [76] was observed in electrochemical intercalation in comparison to thermal intercalation (0.5 mole per mole of TaS_2) [23, 112]. This difference is attributed

to the partial intercalation evidenced by X-ray data [76]. In addition, unit cell dimensions determined by X-ray powder diffraction studies have shown an increase in c-axis spacing of 0.585 nm and 0.602 nm during thermal intercalation of pyridine [2, 23, 113, 114] into TaS_2 . Gamble et al. [23] have reported that the transition temperature of superconductivity can be raised from 1 K to ≈ 3.5 K by intercalation with pyridine. Kim et al. [115] have demonstrated the disappearance of local charge density wave properties of TaS_2 during pyridine intercalation.

Apart from a thermogravimetric study for deintercalation of pyridine in pyridine intercalated TaS_2 , absolutely no other studies have been reported. Loss of pyridine from the lower phase ($c = 0.585$ nm) starts at about 100°C whereas for higher phase ($c = 0.602$ nm), it starts at about 300°C as observed by the weight loss during the experiments [111].

6.4.1.1 Orientation of Intercalated Pyridine in TaS_2

Little is known concerning the detailed structures of pyridine intercalated compounds of TaS_2 . Much of the reported work is concerned primarily with synthesis and determination of lattice parameters [2, 23, 93, 113, 114]. The first microscopic study was reported by Moran et al. [116]. Electron micrograph images of the lattice obtained by Moran show clearly the repeat distances of 0.6, 1.2, 1.8 nm between fringes of dark contrast corresponding to TaS_2 layers and the light contrast from the empty or pyridine layers (see fig. 6.43). The electron micrograph studies also revealed the large number of lattice imperfections such as edge dislocations and stacking faults. A C-axis repeat distance of 1.01 nm was also reported by Thomas et al. [117].

Depending upon the c-axis variation, three distinct models, depending upon the orientation of pyridine molecules within the van der Waal gaps were proposed by different investigators (see fig. 6.44). The model with the CN axis perpendicular to the layers was initially proposed (fig. 6.44a), because this orientation apparently maximizes the interaction of nitrogen lone pair of electrons with tantalum "d" orbitals [96]. However, later work on the lattice expansions of para substituted pyridines gave results incompatible with this model. No regular c-axis increase was observed with ring substitution at the para position as would be expected for the perpendicular orientation [114]. Consequently a bilayer arrangement was proposed (fig. 6.44b). The first definitive evidence of pyridine orientation based on the mobilities of intercalated pyridine molecules within TaS_2 derived from NMR [118] and subsequently

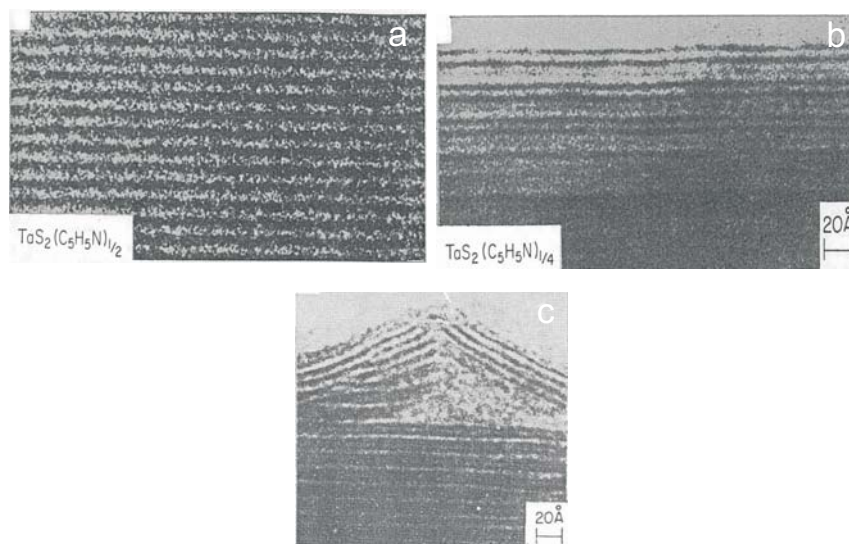


Figure 6.43: Electron micrograph images (200kv) showing highly ordered, atomically thin layered structures of pyridine intercalated TaS_2 ; (a) $(pyridine)_{1/2}$; (b) $(pyridine)_{1/4}$ and (c) crystal lattice imperfections (magnification, X 3,600,000) (taken from [116]).

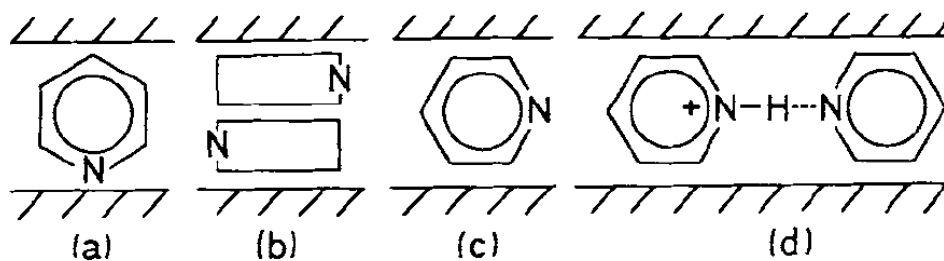


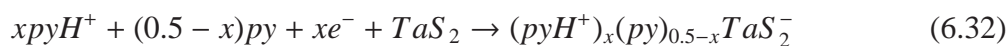
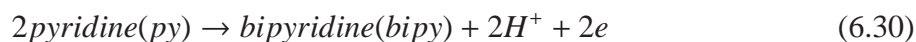
Figure 6.44: Structural models for the position of pyridine in TaS_2 layer (taken from [97])

from X-ray data [119] indicated a parallel orientation of pyridine within TaS_2 layers (fig. 6.44c). Since this situation is obviously most unfavorable for the overlapping of lone pairs on nitrogen with the vacant "d" orbital of tantalum, finally an ionic model was proposed (fig. 6.44d) involving a hydrogen bonding between the lone pairs of nitrogens [97].

6.4.1.2 Bonding

The nature of interaction between TaS_2 and pyridine has been interpreted initially in terms of a charge transfer from the lone pair of nitrogen of the pyridine molecule to the half filled d-orbital of TaS_2 [48]. Optical transmission and x-ray photoelectron spectra gave charge transfer numbers of 0.25-0.3 electron per metal atom [98, 120]. Electrochemical intercalation gave a sharp discontinuity in the voltage

charge curves also at 0.25 electron per TaS_2 [97]. The direct overlap of the σ lone pair of nitrogen from pyridine with the d-orbital of tantalum is difficult due to the large tantalum-nitrogen distance in a parallel configuration and also inconsistent with the data obtained by inelastic neutron scattering [121]. Hence an alternative description of the bonding in pyridine intercalation compound has been proposed [97]. In this model the bonding is described as an electrostatic interaction between negatively charged sulphide layers and pyridinium cations. The reaction scheme that leads to formation of reduced TaS_2 layers and pyridinium cations is given below.



The product is stabilized by ionic bonding between cations and negatively charge layers and by hydrogen bonding between pyridinium cations and solvating pyridine (see fig. 6.44d).

Whereas all the literature described above explains the structure and physical properties of the pyridine intercalated TaS_2 , none of them describes the detailed nano-scale mechanism during pyridine intercalation into TaS_2 . The electrochemical data obtained is also scant and do not involve any high resolution microscopy data. In the following sections we have discussed our results of electrochemical intercalation of pyridine into TaS_2 in detail.

6.4.2 Cyclic Voltammetry

Prior to the STM measurements the stability and surface structure of 1T- TaS_2 in pyridine at pH 3 was characterized by cyclic voltammetry. Fig. 6.45 shows subsequent cycles of a cyclic voltammogram of 1T- TaS_2 in 0.01 M pyridine at pH 3 with a scan rate of 20 mVs^{-1} . The lower potential limit was stepped 100 mV each time between different potential regimes. Various regions of interest in the cyclic voltammogram are

- at potential $> -0.4 \text{ V}$ where only double layer recharging is observed in pyridine-containing H_2SO_4

solution

- reduction potential peaks at - 0.44 V (1c) and - 0.58 V (2c) prior to the onset of hydrogen evolution at around - 0.7 V.
- oxidation potential peaks at - 0.45 V (2a) and - 0.15 V (1a) which correspond to the reduction potential peaks at - 0.58 V (2c) and - 0.45 V (1c), respectively.

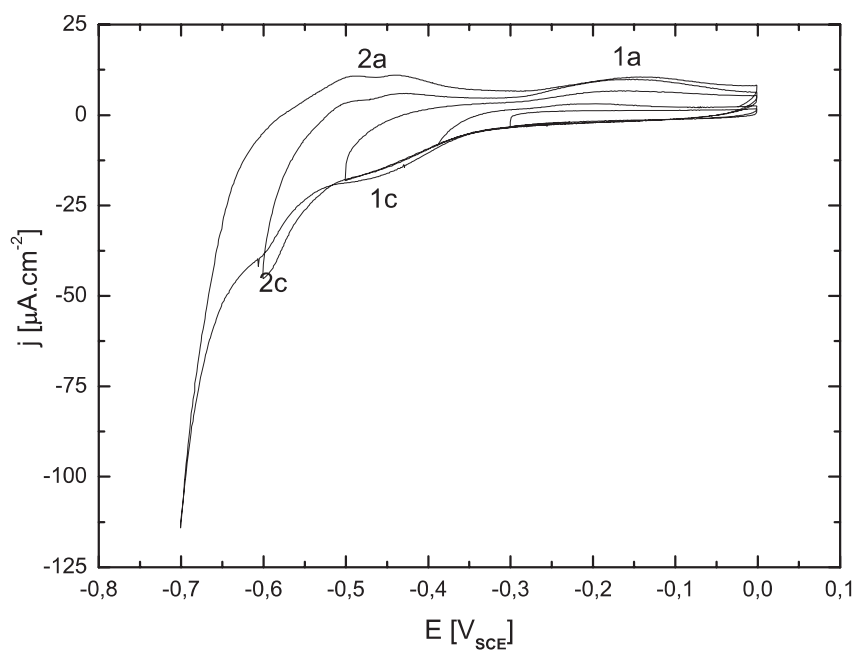


Figure 6.45: Cyclic voltammogram showing subsequent cycles of 1T-TaS_2 in 0.01M pyridine solution at pH 3 (scan rate 20 mV/s) (for description see text).

Once the reduction potential is stepped to -0.5 V, an enhanced anodic current is found in the entire double layer regime, up to the most positive potentials and continues to increase with the subsequent decrease in reduction potential, indicating a slow kinetics of the deintercalation reaction. Furthermore the voltammograms are not stable, but decrease in current in consecutive cycles. The decrease in current between subsequent cycles is less pronounced as compared to octylamine-containing electrolyte.

A plot of charge vs. potential for cyclic voltammograms at variable scan rates (see fig. 6.46) indicates that peaks 1c/1a are pseudo capacitive peaks whereas the features 2c/2a corresponds to a faradaic process, which can be identified with pyridine intercalation/deintercalation (see below). The total charges were obtained by integrating the current at different positions for all cyclic voltammograms and multiplying

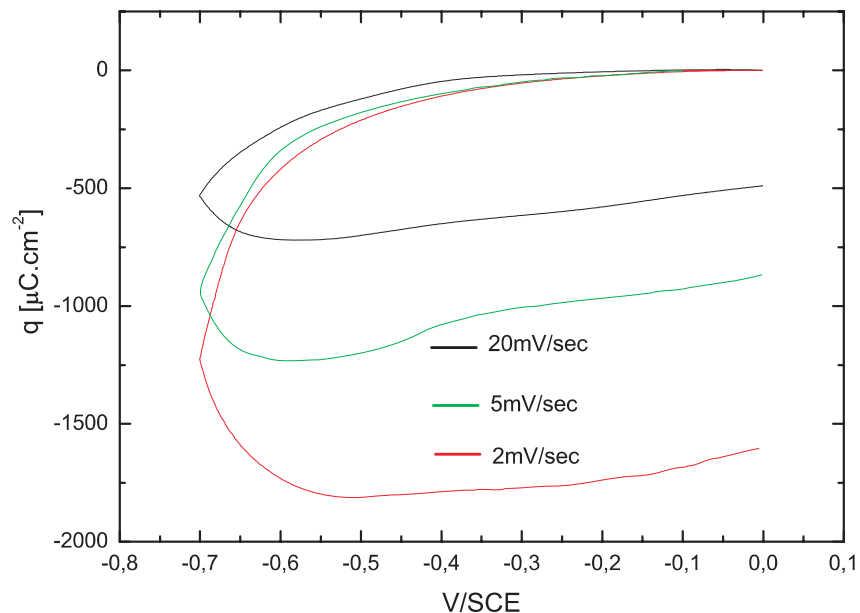


Figure 6.46: Charge vs. Potential curve for cyclic voltammograms with different scan rates showing pseudo capacitive nature (total charge constant $\approx 200 \mu\text{C}\cdot\text{cm}^{-2}$) of the peak 1c in the cyclic voltammogram (see fig. 6.45).

with time. The term pseudo capacitive is applied as the total charges for the corresponding peak i.e. Q are almost constant irrespective of different scan rates. The process at 1c/1a is tentatively assigned to pyridine adsorption/desorption. Assuming an electron transfer of $0.25 e^-$ per pyridine as for intercalated pyridine [2] the peak charge of $\approx 200 \mu\text{C}\cdot\text{cm}^{-2}$ would be in good agreement with a close-packed monolayer of perpendicularly adsorbed pyridine molecules. Adsorption studies of metals (e.g. Li, Na) [122] as well as organics (e.g. NH_3 [1], $\text{NH}_2\text{-NH}_2$ [123]) onto transition metal dichalcogenides adsorption studies has already been reported.

6.4.3 STM Study

Based upon the preliminary idea we got from the CV study, the STM studies in this thesis correspond to the different regions of interest in the cyclic voltammogram (fig. 6.45). Before proceeding to the region of any faradaic process in the CV, imaging of the surface in the double layer region was carried out for a longer period of time in order to check the stability of TaS_2 surface. The stepflow etching was prominent even in the double layer regime (see below) at higher tunneling currents ($> 1 \text{ nA}$) whereas surface morphology was found to be quite stable at lower tunneling current (0.2 nA) and no stepflow etching was observed, similar to the TaS_2 surface morphology observed in octylamine electrolyte. In the

beginning of this section etching process observed at higher tunneling currents are presented followed by the processes that occur at reduction/oxidation peaks of the cyclic voltammogram.

6.4.3.1 Surface Etching at Higher Tunneling Current

At higher tunneling currents (≥ 1 nA), tip induced surface etching in the double layer regime was often observed. In particular, growth of pits as well as etching at step edges were observed. The following figures (see below) will illustrate this phenomenon.

Fig. 6.47 shows a sequence of STM images of the TaS₂ surface in 0.01 M pyridine at pH 3 recorded with a tunneling current of 1 nA. Characteristic pits of monolayer step heights can be clearly observed in fig. 6.47a. Fig. 6.47b, c, d taken at times 6, 10 and 14 minutes shows clearly the growth of pits. Such tip induced growth of pits is common in TMDs [91, 109].

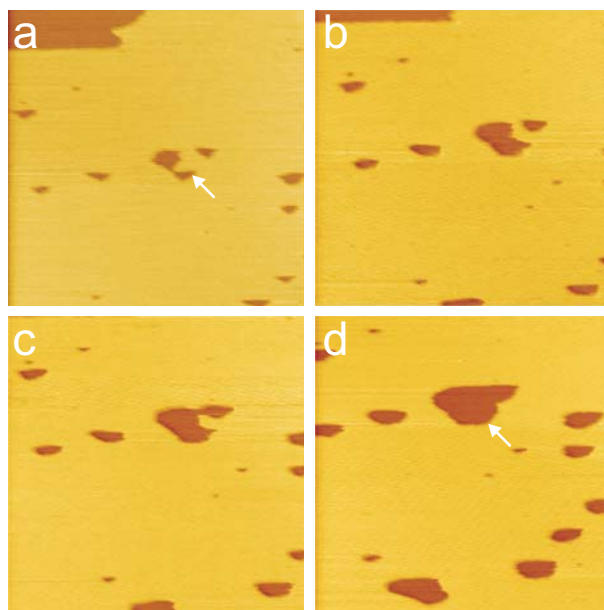


Figure 6.47: Sequences of STM images showing etching at pits in the double layer regime of the cyclic voltammogram ($228 \times 234 \text{ nm}^2$, $I_t = 1 \text{ nA}$).

Similar experiments at steps (see fig. 6.48) also shows a rapid tip induced etching process at higher tunneling currents (1.2 nA). Fig. 6.48a, b, c taken at times of 2, 4 and 8 min. shows this step flow etching (see white arrow) process. The etching rate seems to be faster than in the first case, which might be due to the higher tunneling current applied in this case.

At higher tunneling currents, the tip sample distance for tunneling is much lower, thereby effectively

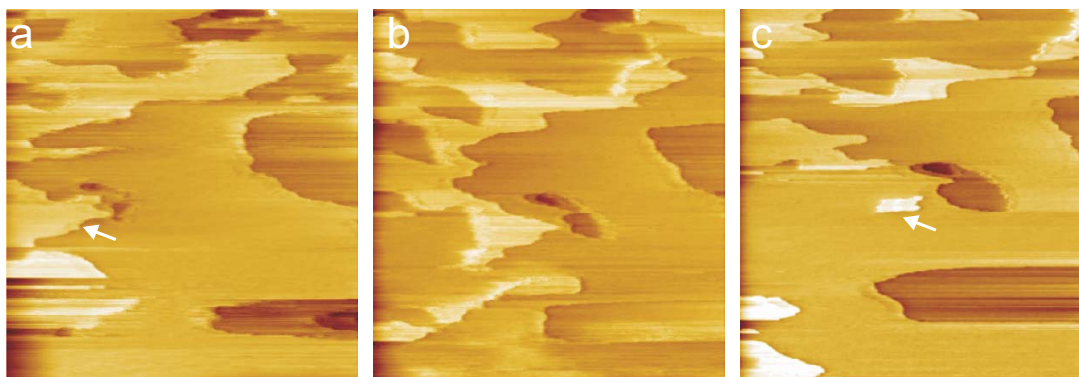


Figure 6.48: Sequences of STM images showing etching at step edges in the double layer regime of the cyclic voltammogram ($264 \times 270 \text{ nm}^2$, $I_t = 1.2 \text{ nA}$).

increasing the interaction energy between tip and sample surface layer. Knowing a perfect TaS_2 surface with threefold coordinated S-atoms is a stable configuration, step edges having S-atoms which are either bound in a two-fold or one-fold configuration are less stable and thus may be removed more easily by the interaction with the tip. The formation of different types of surface modifications on MX_2 using scanning tunneling microscopy (STM) have been already reported in literature [91, 108, 109]. The mechanisms suggested are controversial. Parkinson [108] presented four different models which all may contribute to the etching process: (i) the production of reactive species caused by the current flow between tip and sample; (ii) the etching by power and heat dissipation also located between tip and sample and caused by the current flow; (iii) a field assisted evaporation as known in field ion microscopy; and (iv) a mechanical abrasion of the top-most layers. Enss et al. [109] and Yamaguchi et al. [91] described the tip induced etching at higher tunneling currents. In order to avoid this tip induced etching in the subsequent studies, the tunneling current was set to a lower value of 0.2 nA.

6.4.3.2 Intercalation of Pyridine in TaS_2

The structural changes in TaS_2 in the cathodic potential regime between - 0.44 V to - 0.7 V are as follows.

- Pyridine adsorption and roughening of the TaS_2 surface along with formation of islands.
- Step height increase during pyridine intercalation.

The fact that defects are the preferential position for intercalation are shown by the results of inter-

calation of pyridine into TaS_2 in the following figures.

The initial stages of pyridine intercalation in $1T-TaS_2$ are illustrated by the series of images in fig. 6.49, which were recorded on a large atomically flat terrace exhibiting a few pits with a depth of 0.58 nm (i.e. the height of one TaS_2 layer). Starting from the double layer potential regime (fig. 6.49a), the potential was gradually decreased until slow step flow etching commenced in the potential regime of peak 1c (see fig. 6.45). Upon further decreasing the potential to - 0.68 V (fig. 6.49c-e) sudden drastical changes were observed. Specifically, the STM imaging became less stable and small island-like structures with a height of 0.3 nm emerged on the upper terrace (see e.g. fig. 6.51f). Interestingly, these structures were not observed on the lower terrace, indicating that these changes are not merely caused by adsorption or deposition onto the TaS_2 surface. As visible in the cross sections in fig. 6.49a and 6.49e the height of the step changes by ≈ 0.3 nm, parallel to this change in appearance of the upper terrace. Based on these observations the structural changes at - 0.68 V i.e. at peak 2c in the voltammogram, can be clearly assigned to the pyridine intercalation. In many images of our experiments, we have found a lot of white strips which we attribute to the rapid movement of molecules on the surface as is reported previously [124]. At potentials $\leq - 0.7$ V, imaging of the surface topography was quite unstable as observed in a lot of our experiments. This we attribute to the bulk intercalation as well as hydrogen evolution by water electrolysis resulting in a large cathodic current (higher than the tunneling current applied) which ultimately results in a tip jump and bad imaging quality.

A plot of height change and potential vs. time during the intercalation process for all the images (partially shown in fig. 6.49) is shown in fig. 6.50. The change in step height from the nominal monolayer step height value ≈ 0.6 nm to ≈ 0.9 nm is a clear indication of intercalation with the pyridine molecules lying parallel to the TaS_2 layer.

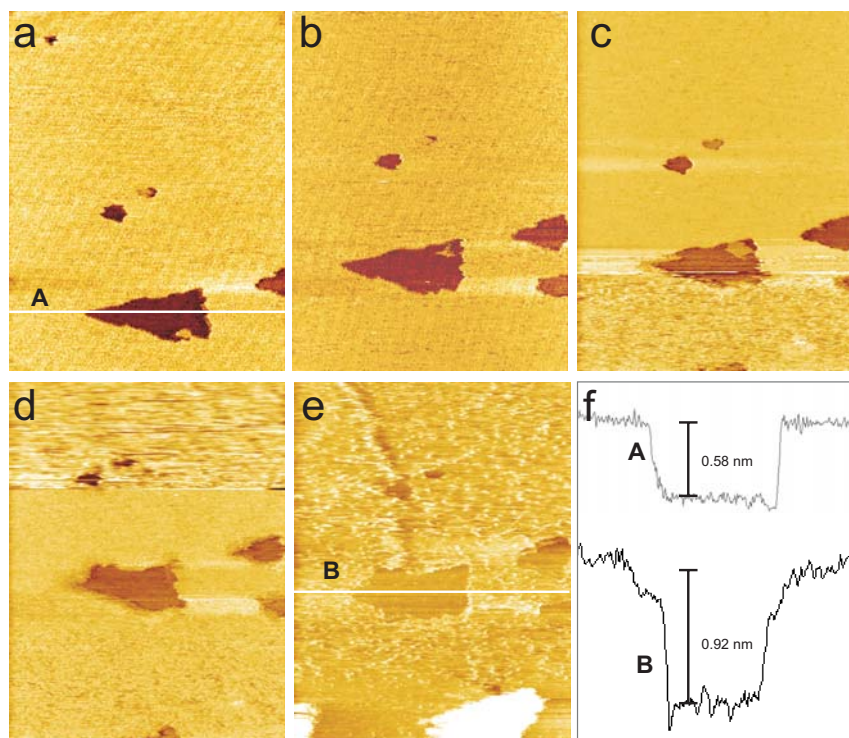


Figure 6.49: Sequences of in-situ STM images of 1T-TaS_2 ($270 \times 298 \text{ nm}^2$) in 0.01 M pyridine-containing H_2SO_4 solution (pH 3) showing pyridine intercalation on a surface exhibiting pits. Images were recorded (a) at -0.22 V , (b) after the potential was kept 8 min. at -0.44 V and after the potential was kept (c) 12 min., (d) 14 min. and (e) 22 min. at -0.68 V . (f) Cross section along scan lines across the holes in fig. A and B.

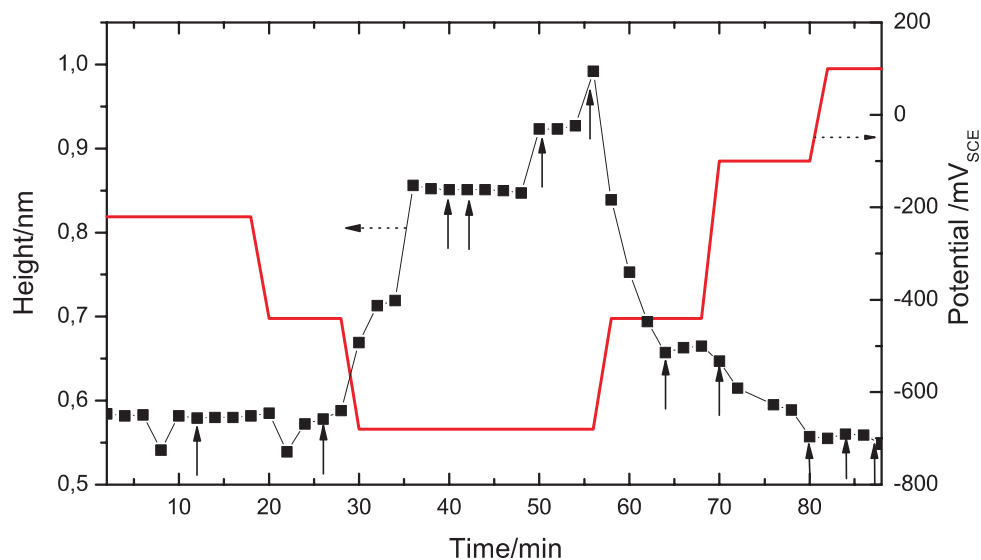


Figure 6.50: TaS_2 interlayer spacing (solid line with black rectangles), obtained from step height measurements in the STM sequence partially shown in fig. 6.49 and 6.56. Times of displayed images are indicated by solid arrows. In addition, the applied potential (red line) is shown.

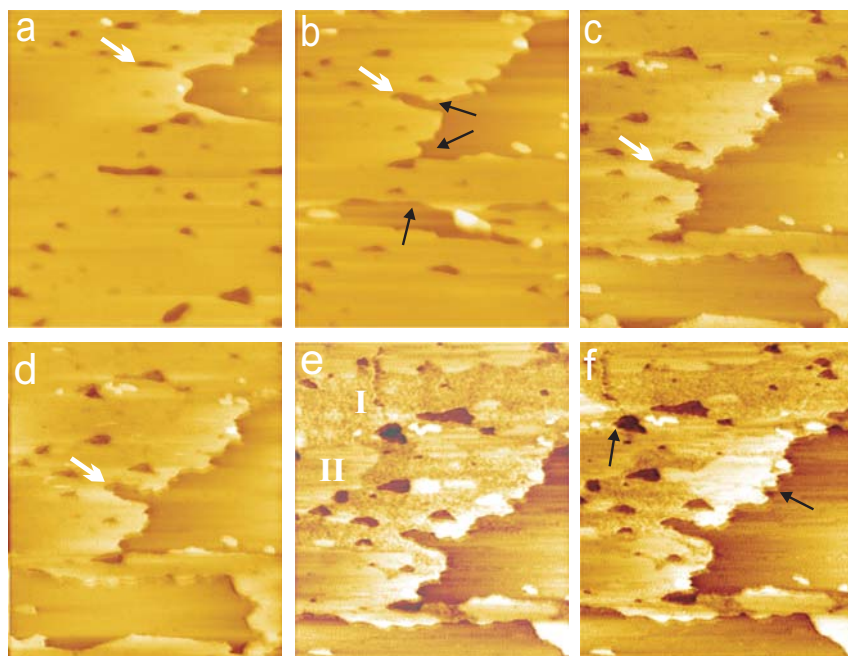


Figure 6.51: Sequences of in-situ STM images ($413 \times 510 \text{ nm}^2$) of 1T-TaS₂ in 0.01 M pyridine-containing H₂SO₄ solution at (a) - 0.22 V, (b) 6 min. after changing the potential to - 0.44 V, and (c) 12 min., (d) 18 min., (e) 24 min., (f) 30 min. after changing the potential to - 0.68 V, resulting in pyridine-induced step flow etching and island formation during intercalation near a TaS₂ step edge. The white arrow marks identical positions in the images.

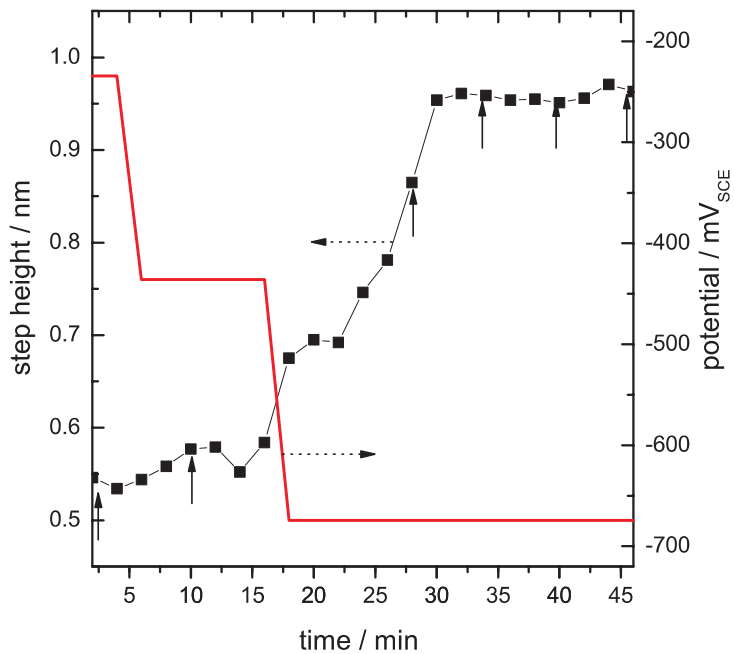


Figure 6.52: A plot of step height and potential vs. time for all the images in fig. 6.49 showing the step height increase during intercalation.

A second experiment showing the progressive pyridine intercalation is presented in fig. 6.51. Again the step flow etching is observed after a change from the double layer regime (fig. 6.51a) to - 0.44 V (fig. 6.51b), as e.g. visible at the positions marked by arrows in fig. 6.51b. After further decreasing the potential to - 0.68 V (fig. 6.51c-f) a similar behavior as in the experiment in fig. 6.49, i.e., the emergence of irregular features on the upper terrace and a lower STM imaging stability was observed. The average step height increases within the first 15 minutes after the potential step to 0.96 ± 0.04 nm and then maintains this value (fig. 6.51d). Subsequently, islands of a new phase are forming on the surface (fig. 6.51e). In contrast to the first more irregular appearing intercalation phase (designated as phase I in the latter discussion), this new phase (phase II) appears 0.3 nm higher and much smoother. Furthermore the island of phase II are observed predominantly close to the steps of the TaS_2 substrate. With time the islands of phase II grow into the areas formerly covered by phase I (fig. 6.51f, see arrows). Formation of different phases by cathodic reduction of TaS_2 from aqueous pyridinium salt solution has already reported by Zagefka [2, 125]. Three different biphasic products in the lower reduction range have been identified : (a) TaS_2 second stage intermediate with pyridine ring planes parallel to the TaS_2 layers ($d = 2 \times 6 + 3 = 15 \text{ \AA}$), (b) second- stage phase/first-stage phase with parallel orientation of the aromatic ring planes ($d = 6 + 3 = 9 \text{ \AA}$), (c) first-stage phase ($d = 9 \text{ \AA}$)/first-stage phase ($d = 12 \text{ \AA}$) with the pyridine ring planes perpendicular to the layer planes [97, 125]. At potentials negative of - 0.7 V a rapid loss in the quality of STM imaging was observed in a large number of experiments, which may be caused by substantial bulk intercalation as well as hydrogen evolution.

A similar plot of step height and potential vs. time for all the images (partially shown in fig. 6.51) results in a step height increase of 0.3 nm (see fig. 6.52) after intercalation.

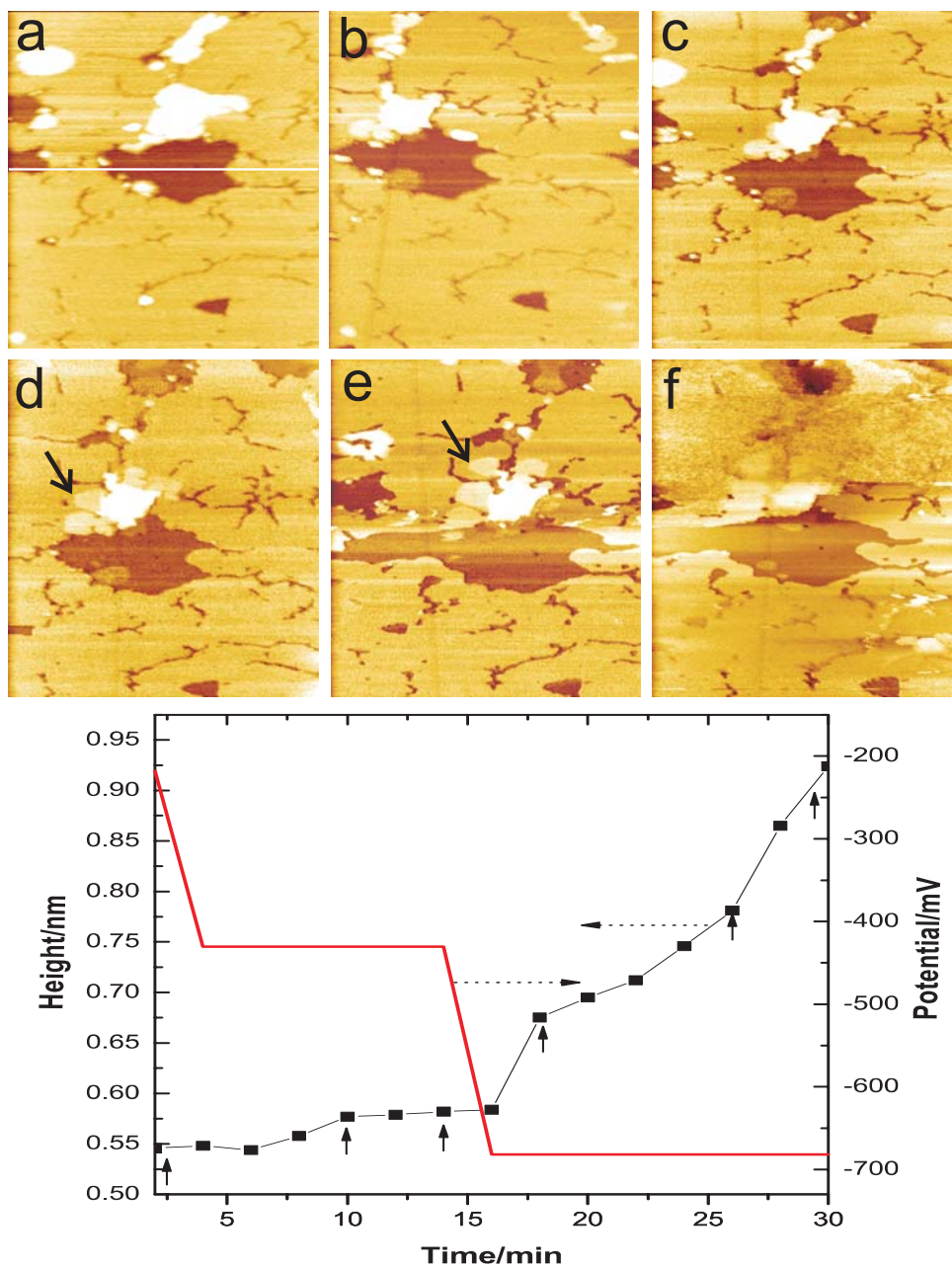


Figure 6.53: Sequences of in-situ STM images ($270 \times 298 \text{ nm}^2$) of $1T\text{-TaS}_2$ in 0.01 M pyridine-containing H_2SO_4 solution at (a) - 0.22 V, (b) 8 min. and (c) 12 min. after changing the potential to - 0.44 V, and (d) 4 min., (e) 12 min., (f) 16 min. after changing the potential to - 0.68 V, resulting in pyridine-induced step flow etching and island formation during intercalation near a TaS_2 pit. The black arrow marks island growth positions in the images.

The sequence of images shown in fig. 6.53 were recorded after the first intercalation /deintercalation cycle (see fig. 6.49 and fig. 6.56). As observed in fig. 6.53a, recorded at -0.22 V, the initial surface has a lot of defects in the form of nanocracks as a result of the first intercalation / deintercalation cycle. In addition large islands of different sizes varying from 0.3 nm to 2.4 nm, which are produced during the deintercalation process, are still observed. Once the potential was changed to -0.44 V and lower, etching at steps started again. The nanocracks slowly started to grow which ultimately results in large surface cracks (see fig. 6.53e). In addition, large islands also started to dissolve in a layer by layer fashion. Once the potential is shifted to -0.7 V, the islands seemed to grow again (shown by arrows in fig. 6.53d, e). The height of these smooth islands is ≈ 0.3 nm with respect to the top layer and hence, are the Phase II complex of intercalated pyridine. After waiting for longer time at -0.7 V (≈ 14 min.), image quality deteriorated (probably related to a tip jump) which can be attributed to the bulk intercalation as well as hydrogen evolution. The plot of step height and potential vs. time (see fig. 6.53) again shows a nominal increase of ≈ 0.3 nm consistent with the parallel orientation of pyridine molecules.

The nano scale in situ STM observations presented here are in good agreement with previous x-ray diffraction results on electrochemically pyridine intercalation into TaS_2 in aqueous electrolyte, which likewise found phases with 0.9 nm and with 1.2 nm layer expansion [2,125]. These phases were attributed to a pyridine-pyridinium complex oriented parallel and perpendicular to the TaS_2 planes, respectively, and which we associate with phase I and phase II observed in this work. The STM data indicates a mechanism of pyridine intercalation into the lattice as shown schematically in the model in fig. 6.54. In the initial stages of this process (fig. 6.54a) adsorbed pyridine molecules interdiffuse into the van-der-Waals gaps between the TaS_2 layers starting from the defects such as steps. This results in the formation of a diluted intercalation phase of parallel oriented molecules. With time the density of intercalated molecules slowly increases resulting in a gradual increase in the average layer spacing (under the conditions of our experiment on time scale of ≈ 10 min) until a close-packed molecular layer of parallel oriented pyridine i.e. of phase I with a defined layer spacing of 0.96 nm is formed in the van-der-Waals gap (fig. 6.54b). Further intercalation of pyridine into the gap is only possible by a change in the molecular orientation, which occurs in the subsequent transition to phase II via an island growth starting apparently at the defects in the substrate (fig. 6.54c)

As shown in fig. 6.51, phase I is of rather uniform appearance on the entire top most terrace and, in particular, does not exhibit any island growth on the initial non intercalated TaS_2 substrate. This suggests a high mobility of the pyridine molecules within the gaps in this phase, i.e., the intercalated molecules form a "2D gas" in between the TaS_2 layers. In contrast the island growth mechanism found in the phase I/phase II coexistence regime seems to indicate a substantially lower molecular mobility, probably due to geometric blocking by neighboring molecules. The much smoother appearance of the areas corresponding to phase II as compared to those of phase I in the STM images is currently not understood, but might indicate a better ordering of the molecular layer in the phase II. Since a perpendicular pyridine orientation allows stronger inter molecular interactions via the Π systems of the molecules, an increased molecular ordering in this intercalation phase is probable.

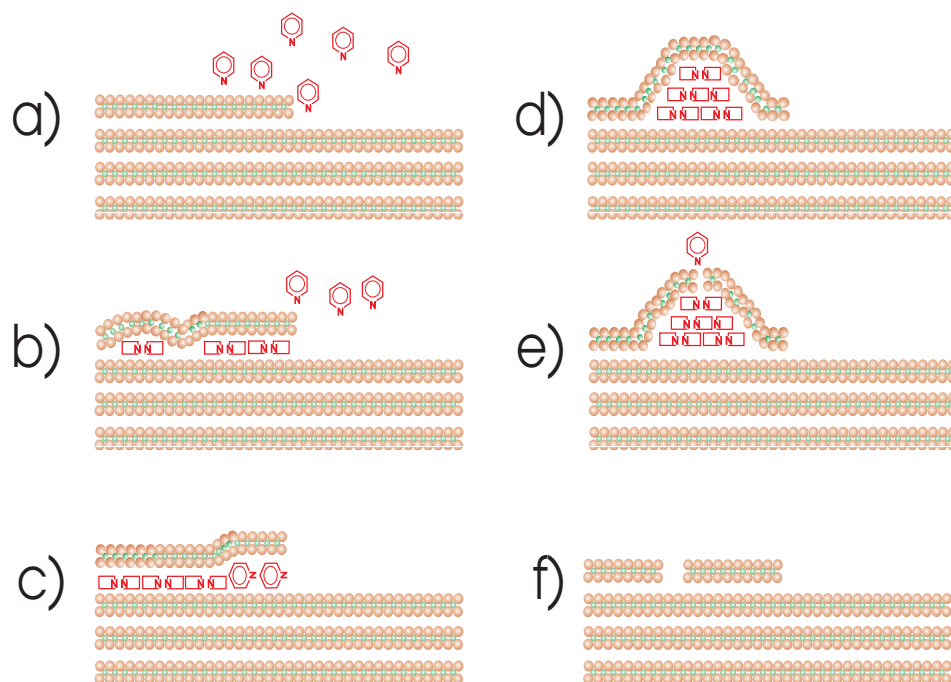


Figure 6.54: A model showing the intercalation (a, b, c) and deintercalation process (d, e) of TaS_2 in 0.01M pyridine (pH 3), with pyridine oriented parallel (rectangles) or perpendicular (hexagons) to the TaS_2 planes.

A currently not completely understood effect is the step-flow etching, found in the potential regime of peak 1 both in pyridine and octylamine containing electrolyte. Since this phenomenon is not observed in pure H_2SO_4 solution and commences in the potential range associated with adsorption of the organic

cations, just positive of the onset of intercalation, it is obviously directly induced by the molecular adsorbates. An experimental artifact, especially a purely tip-induced etching as found in previous STM studies [91,108] as well as in our experiments at tunneling currents ≥ 1 nA, can be ruled out. In particular, the latter could not explain why the etching process is restricted to the potential regime of peak 1c and not (or only at strongly reduced rates) found at more positive or more negative potentials. However, a contribution of tip-induced forces to an existing reduced stability of the TaS_2 layer in the potential regime of peak 1c (see below) cannot be unambiguously excluded.

The observed step-flow etching resembles in situ STM observations of Li intercalation into HOPG, where likewise a partial removal of the host lattice along steps was reported and attributed to exfoliation [13]. Assuming that the same explanation holds true for the etching of the $\text{TaS}_2(001)$ surface in the systems studied in this work, the STM data suggest that pyridine or octylamine adsorption in the potential regime of peak 1c induces exfoliation whereas at more negative potentials (peak 2c) stable intercalation phases are formed. Such a behavior may be rationalized by existing intercalation models [93,123,126], if one considers the direct dependence of the free energies of adsorption and intercalation on the potential. Specifically, adsorption of the cathodic guest species on surface and, in particular, defect sites such as steps should occur at more positive potentials than intercalation into the bulk. This may lead to destabilization of the lattice near the step edges. For example, the concomitant polarization of the host lattice at these sites could induce a local lattice expansion, resulting in high local stress and fracturing of the host lattice. In contrast, these spatial inhomogeneities should be reduced at more negative potentials, where the guest species form uniform, close-packed adsorbate structures on and in between the host layers, lowering the tendency towards exfoliation. Since these considerations should be generally valid for electrochemical intercalation in layered materials, in situ STM studies of other, comparable systems might find similar effects, which would support these hypotheses.

In order to compare the morphology before and after intercalation ex-situ AFM and SEM measurements were performed on the bare and pyridine intercalated TaS_2 . Intercalation was performed potentiostatically by keeping the sample for about an hour at - 0.7 V in 0.01 M pyridine electrolyte. The sample was then removed from the electrolyte and washed with water and kept for drying. The dried sample was then used for ex-situ SEM and AFM measurements. Fig. 6.55a, b shows the surface morphology

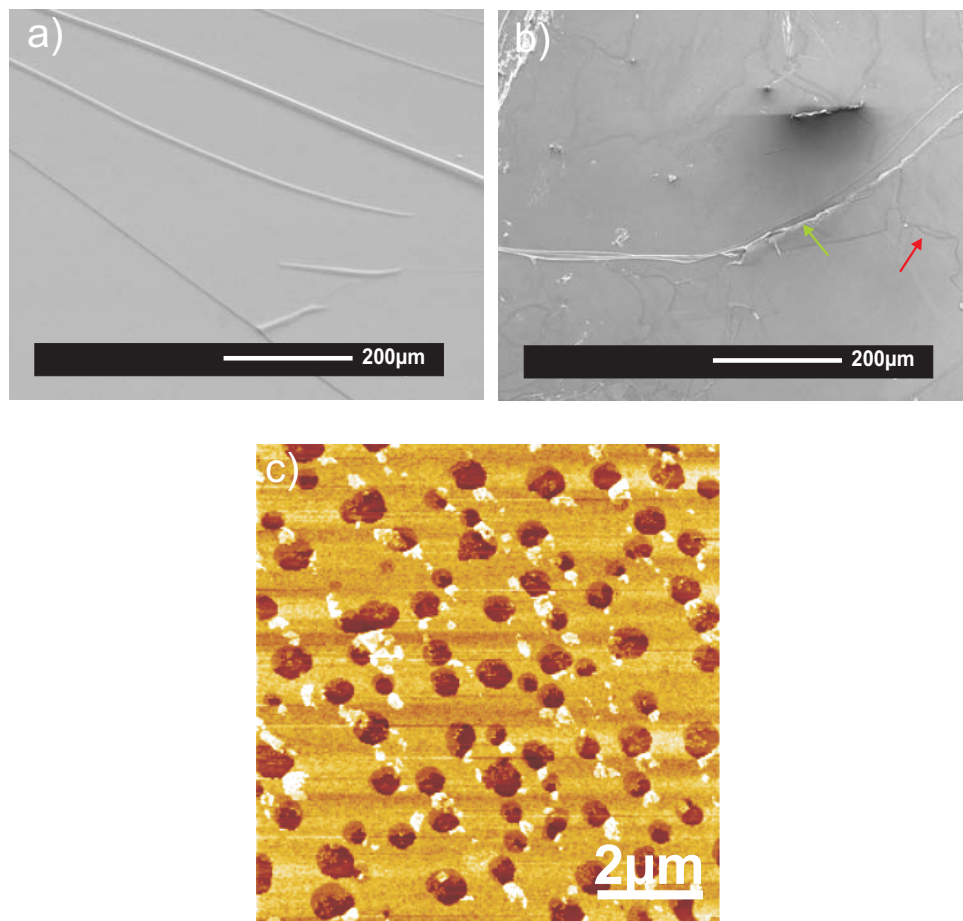


Figure 6.55: Scanning electron microscopic morphology of the TaS_2 surface (a) before and (b) after intercalation with pyridine and (c) a non contact AFM image after intercalation with pyridine.

of TaS_2 before and after intercalation with pyridine. Large flat areas extending over several μm along with some macro step edges can be clearly seen in the pristine sample (fig. 6.55a). Taking a closer look at the macro steps of the intercalated sample, the steps seem to be filled with materials (green arrow, fig. 6.55b). An interesting behavior are the appearance of darker areas at the step edges (red arrow, fig. 6.55b). Such darker areas are an indication of presence of excess sulphur in the surface layer which reacts with pyridine forming such dark areas [111]. In addition, non-contact AFM images of pyridine intercalated TaS_2 shows large islands (heights varies between 0.6 nm to 1.8 nm), in the vicinity of pits (see fig. 6.55c). The step height shows an increase of ≈ 0.4 nm (step height of $\text{TaS}_2 \approx 0.58$ nm). This is a clear indication that pyridine undergoes intercalation at the defects present on the basal plane, which are preferential position of intercalation because the lattice energy associated with intercalation is lower

at such basal defects than inside the bulk and hence bending can easily occur.

6.4.3.3 Deintercalation

Scant studies has been done for deintercalation of pyridine from $\text{TaS}_2(\text{py})$ complex. One such study involving the weight loss during deintercalation process by thermal heating was reported by Thompson [111]. Leaving apart this weight loss study, absolutely no structural and mechanistic study of the deintercalation process has been done up to date. Here we present the first results of a structural and mechanistic study of the deintercalation process in pyridine intercalated TaS_2 .

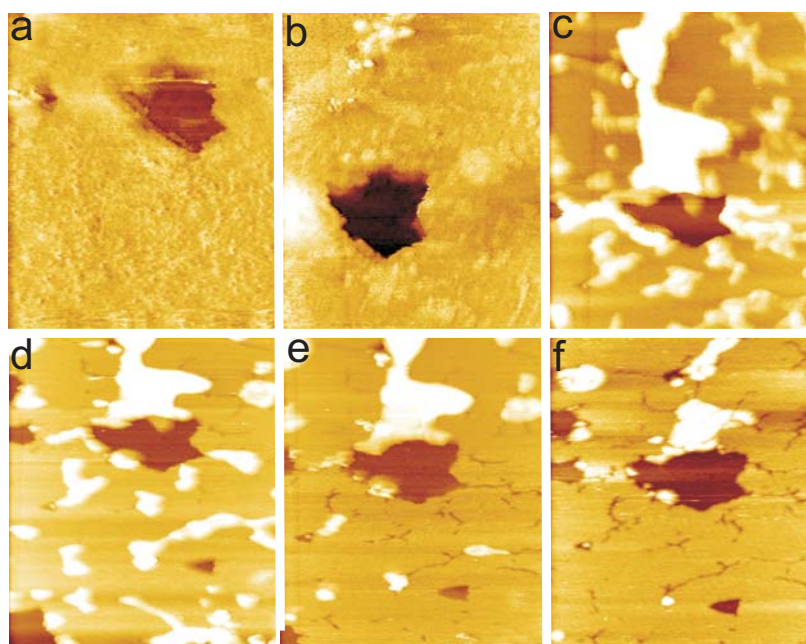


Figure 6.56: Sequences of in-situ STM images ($270 \times 298 \text{ nm}^2$) of 1T-TaS_2 in 0.01 M pyridine containing H_2SO_4 solution (pH 3), showing (a) the surface after 8 min of intercalation at -0.68 V . Subsequently the potential was increased to -0.44 V and 8 min. later to the double layer regime. The displayed images are obtained after (b) 64 min. at -0.44 V , (c) 72 min. at -0.10 , (d) 80 min. at -0.10 V , (e) 84 min at 0.10 V and (f) 88 min. at 0.10 V .

In most of our experiments during intercalation, a tip jump was often observed which ultimately forced us to stop our experiments. This is the primary reason, the reverse cycles i.e. the deintercalation process involving removal of intercalated pyridine from TaS_2 layer, was seldom observed. One such experiment is presented here. The deintercalation process described here is part of the experiment where intercalation was observed in the beginning as shown in fig. 6.49. Upon changing the potential in positive direction deintercalation of pyridine out of the TaS_2 host lattice can be observed (see fig. 6.56).

The image in fig. 6.56a was recorded 8 min. after fig. 6.49e and shows the characteristic rough, but uniform surface in regime of intercalation phase I. In the subsequent images of this series the potential was stepwise increased, resulting in pronounced morphological changes. Specifically, up to 2.4 nm high hills form on the surface. At potentials ≥ -0.1 V (fig. 6.56c-f) a smooth surface, characteristic for TaS_2 in the double layer range, is found between these islands and the island have defined heights of 0.3 nm or multiples thereof. With increasing time the islands are slowly dissolved, but even after 30 min some islands remain on the surface. After complete island dissolution cracks are found at the island positions (see fig 6.49e-f). In parallel to these changes the step height of the bilayer pits starts to revert from 0.9 to 0.6 nm after the potential is increased to - 0.44 V (see fig. 6.50).

To explain the formation and subsequent slow dissolution of these islands, a deintercalation mechanism is suggested. As the potential was shifted to the more positive value, the polarization state of the TaS_2 surface reverses. This reversal of polarization ultimately results in the release of the electrons (acquired by TaS_2 during intercalation) back to the pyridine molecule. At this point, as the pyridine molecules gain electrons, substantial repulsion between the electron rich pyridine molecule and the negatively charge S^{2-} layers of TaS_2 develops. As a result of this repulsive interaction, pyridine will start to accumulate in the form of inclusions within the host lattice (see fig. 6.54d). Formation of such inclusions will subsequently result in stress within the host lattice. In order to release this stress, the inclusions will try to slowly diffuse out of the lattice through the lattice defects, thereby forming islands on the surface (see fig. 6.54e). These defects potentially form due to mechanical stress, induced by the lattice deformation in the vicinity of the inclusions during intercalation. The observed island heights indicate that pyridine is oriented parallel to the TaS_2 planes in these inclusions. Similar heights were observed for physisorbed pyridine multilayer islands in a UHV-STM study [127], where the molecules were adsorbed in parallel orientation. With passage of time in the anodic regime, large islands will slowly start to dissolve in a layer by layer fashion (as observed in fig. 6.56) and ultimately the bare TaS_2 surface with a step height equal to the nominal monolayer step height (≈ 0.58 nm) will remain (see fig. 6.54f).

7 Summary on organic molecule intercalation into TaS₂

The in situ STM observations of the initial stages of electrochemical pyridine and octylamine intercalation into (001) oriented 1T-TaS₂ presented in this study provide a detailed picture on the mechanisms of these processes on the nanoscale. Specifically, the following observations were made:

- In pure H₂SO₄ solution only double layer recharging and no structural changes are found down to the onset of hydrogen evolution.
- Electrochemical measurements in pyridine and octylamine containing electrolytes indicate adsorption of the organic molecules at potentials prior to the onset of intercalation. In this potential regime a step flow etching process is observed, which decreases in the presence of the intercalation phases and which is tentatively attributed to (potential-dependent) exfoliation.
- For pyridine intercalation the phase behavior, found in previous studies [125], could be followed directly by high-resolution STM. It commences at surface defects with the insertion of molecules that are parallel oriented with respect to the TaS₂ layers and highly mobile within the van-der-Waals gaps. The density of the molecules in this intercalation phase gradually increases, resulting in an increase in the average layer spacing from 0.58 to 0.92 nm. After the molecular density in the gaps has reached a saturation value, a slow first order phase transition in the molecular layers to a second intercalation phase occurs, in which the pyridine molecules are assumed to be perpendicularly oriented starting from surface defects.
- Pyridine deintercalation results in the formation of metastable nanoscale blisters with heights that are multiples of 0.3 nm. These blisters are attributed to small inclusions of bulk pyridine and slowly dissolve with time, leaving defects in the surface layer behind.

The data obtained here are the first high-resolution in situ study of an organic electrochemical intercalation process. Furthermore, our observations demonstrate that electrochemical intercalation offers interesting novel possibilities for the nanoscale modification of well-defined dichalcogenide surfaces. For example, the absence of structural changes in the bottom of monolayer pits long after the formation of an intercalation phase on the surrounding surface indicates that such processes may be employed for

the preparation of an intercalate monolayer, i.e. the controlled electronic decoupling of the topmost layer from the dichalcogenide bulk. This may have interesting applications for the preparation of quasi-2D crystals, a currently intensely investigated subject. In a similar way, also the spontaneous formation of nanoscale organic inclusions of surprisingly high stability found by the STM measurements during deintercalation, may be of interest for the formation of organic-inorganic nanostructures on surfaces. Since many of the results are related to the structure and properties of the layered host lattice, similar nanostructure formation processes may occur in the numerous other organic intercalation phases of dichalcogenides as well as other layered materials.

8 Results on Cu deposition onto TaS₂

In this section results of electrochemical deposition of copper onto TaS₂ in 0.01 M CuSO₄ and 0.01 M H₂SO₄ electrolytes are discussed. Before discussing our results, a short review of previous literature of metal deposition onto transition metal dichalcogenides is given.

8.1 Literature Review

Nanowires are of fundamental as well as technological interest e.g. for nanoelectronics and sensor applications. In studies of metal deposition on the cleaved plane of layered transition metal dichalcogenide (TMDC) surfaces under ultrahigh vacuum (UHV) conditions, the formation of self assembled nanowire networks as well as larger tunnels for a variety of metal species and substrates has been reported [16–21, 128, 129]. Adelung et al. [128, 129] have reported that Rb deposition onto a variety of TMDCs (WSe₂, HfS₂, TiS₂, VSe₂, TiTe₂, TaS₂), nanostructures (e.g. nanotunnels) of different dimensions (5-250 nm high, mesh size in μ s) can be obtained. Later on they have extended their ideas to other metals (e.g. Cu, Cr, Ag), and found that similar networks can also be obtained [16, 20]. Rainer Kunz in his Phd thesis [20] has shown that, different buckle networks can be observed by Cu deposition onto TaS₂. Two different types of buckles are observed, one with sharp defined edges and the other having a tube like shape and no sharp defined edges (see fig. 8.57). The typical width and mesh size of the former is $\approx 1\mu$ m and 100μ m, and of the latter is $\approx 5\mu$ m and 20μ m, respectively. These structures often are oriented along the close-packed directions of the substrate lattice and were originally attributed to admetal-induced cracking of the dichalcogenide surface layer, followed by metal nucleation and growth in the resulting linear defects [16, 17]. Variation of different deposition parameters has also been demonstrated by Kunz. Increasing Cu film thickness from 5 nm to 20 nm, an increase in number, width as well as density of buckles was observed. The temperature dependence of nanotunnel formation for a 20 nm thick Cu film revealed, the formation of normal nanotunnels at room temperature whereas at 100°C, only a homogeneous Cu film was observed. Decreasing the temperature to -120°C results in the formation of randomly oriented nanotunnels having no sharply defined edge. Annealing has no effect on the existing nanowire networks as observed by Kunz for a 20 nm Cu film deposited onto TaS₂ surface. Performing shadowmask experiments by using a TEM grid, Kunz has also demonstrated the high diffusion length of

Cu on TaS_2 which agreed well with the formation of dendritic structures. However, in all these interpretations, the possibility of a chemical interaction of the metal and the layered crystal was not taken into account. More recently, Spiecker et al. have shown by electron microscopy that all these linear nanostructures corresponds to tunnels formed by folding of the substrate lattice [19,21]. They have explained the formation of nanotunnels via an intercalation induced mechanism, where the impinging metal atoms diffuse into the uppermost layers of the layer crystal and form an intercalation phase. This phase transformation is accompanied by lattice expansion, which is constrained by the rigid substrate, leading to build up of compressive biaxial strain and stress in the intercalation layer. Beyond a certain critical layer thickness, nanofolds form, propagate and branch with high velocity, across the surface, thereby forming the networks. The objective of the present work was to clarify whether similar types of structures also form during electrochemical deposition from electrolyte solutions and to compare the resulting morphology with that found for vapor deposition. Copper on 1T- TaS_2 was chosen for these studies, because it can be easily electrodeposited from aqueous solutions and was already found to exhibit nanotunnel formation in vapor deposition studies [16,20].

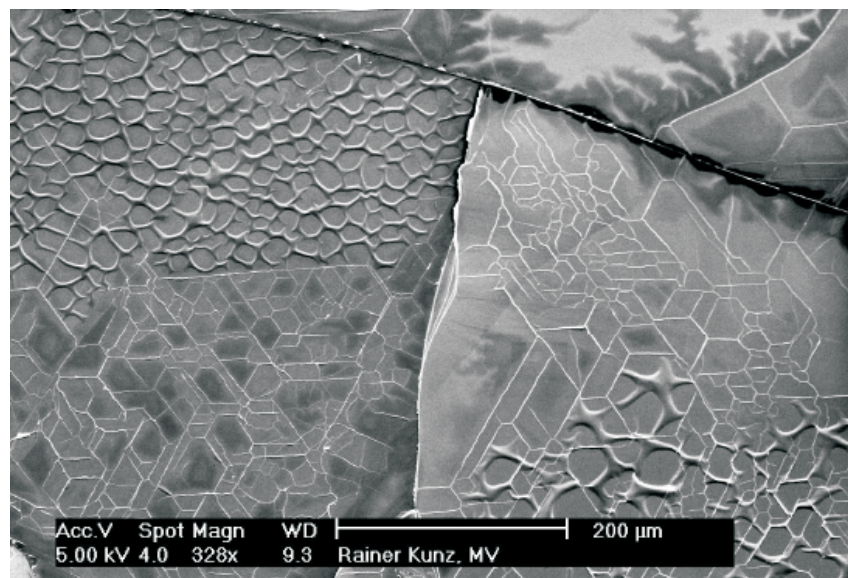


Figure 8.57: Different nanonetworks formed in vacuum deposition of Cu onto TaS_2 [20]

8.2 Electrochemical Characterization of TaS₂ in 0.01 M CuSO₄/H₂SO₄ Electrolyte

Cyclic voltammograms of a 1T-TaS₂ electrode in 0.01 M CuSO₄ + 0.01 M H₂SO₄ are shown in fig. 8.58. The calculated Nernst potential is + 0.022 V vs. SCE. Electrodeposition starts at potentials negative of -0.2 V, i.e. requires substantial overpotentials, as manifest by the emergence of a Cu bulk stripping peak at 0.1 V in the subsequent positive potential scan. At potentials negative of -0.43 V a second reduction process with a corresponding anodic peak at -0.34 V commences. After potential sweeps to even more negative values, where hydrogen evolution occurs, this peak develops into very broad oxidation peaks (from -0.5 to 0.1 V) in the positive scan. These observations are in good agreement with the results of a previous electrochemical and ex-situ spectroscopic study which indicate Cu intercalation at these negative potentials [130]. Also the changes in the voltammograms with time, clearly visible in fig. 8.58, are probably caused by changes in the electrode morphology due to intercalation.

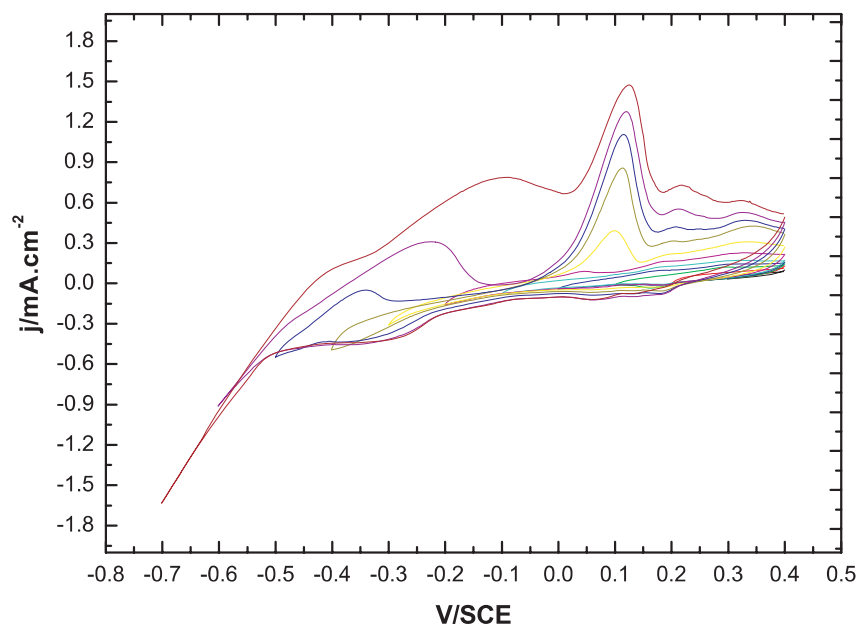


Figure 8.58: Cyclic voltammograms of 1T-TaS₂ in 0.01 M CuSO₄ + 0.01 M H₂SO₄ solution (scan rate 20 mV/sec.)

In most of our experiments copper was deposited galvanostatically, where a constant current was applied for different time intervals in order to get the required coverages of Cu onto TaS₂. Later on the potentiostatic method was also employed, in order to compare the results with those obtained under galvanostatic deposition conditions. The parameters used for different coverages are summarized in

table 3. In fig. 8.59, the galvanostatic curves for different Cu coverages are shown. These curves were

Table 3: Galvanostatic deposition data

# Current Density (mA·cm ⁻²)	# Time (sec.)	# No. of monolayers (ML)
0.5	18	10
	45	25
	54	30
	90	50
	126	70
		1ML = 8.9 μC·mm ⁻²

obtained by applying a constant current density of 0.5 mA·cm⁻² for different time intervals (see table 3) in order to get the desired coverages. The surface area in all the cases was $\approx 16 \text{ mm}^2$. For 10 ML Cu coverage (fig. 8.59a), the potential was terminated at around -0.25 V and no saturated potential was reached. However, for 25 ML, 50 ML and 70 ML at around 40 s a saturation potential of $\approx -0.5 \text{ V}$ was reached. As can be seen from fig. 8.59b, c, d, an overpotential of -0.2 V is needed for bulk copper deposition which is in good agreement with the cyclic voltammetry. The curves are not identical in the same time range. This might be due to the failure to measure the exact surface area of the samples because of their unusual shape as well as presence of defects in crystals.

Similar experiments at different current densities were also performed (see fig. 8.60). The surface area was $\approx 16 \text{ mm}^2$. At a lower current density of 0.3 mA·cm⁻², the potential was terminated at -0.12 V which was above the Cu bulk deposition potential and hence no bulk copper deposition occurred. However, at a current density of 0.4 mA·cm⁻², the potential was terminated at -0.45 V i.e well below the Cu bulk deposition potential. The total charge passed was around 3450 μC which was equivalent to 25 ML of Cu.

In order to find whether similar nanostructures form under different applied conditions (e.g. potentiostatic, galvanostatic), potentiostatic bulk deposition was also carried out. Two different potential values at -0.35 V (lower overpotential) and -0.5 V (higher overpotential) were chosen for this purpose. The current vs. time transients are shown in fig. 8.61. Depending upon the time of applied potential, the total charge in all the cases were 835 μC (at -0.5 V), 4120 μC (at -0.35 V), 4190 μC (at -0.5 V) which were equivalent to $\approx 11 \text{ ML}$ (fig. 8.61a, surface area $\approx 9 \text{ mm}^2$) and ≈ 28 and 29 ML of Cu (8.61b, c, surface

area $\approx 16 \text{ mm}^2$). During the very first few seconds, the current intensity is high due to the transient diffusion phenomenon. When the diffusion layer thickness became constant, a steady state current was achieved in all the case. The steady state current at higher overpotential (-0.5 V) and lower overpotential were $\approx 0.9 \text{ mA} \cdot \text{cm}^{-2}$ (fig. 8.61a, c) and $0.6 \text{ mA} \cdot \text{cm}^{-2}$ (fig. 8.61b), respectively.

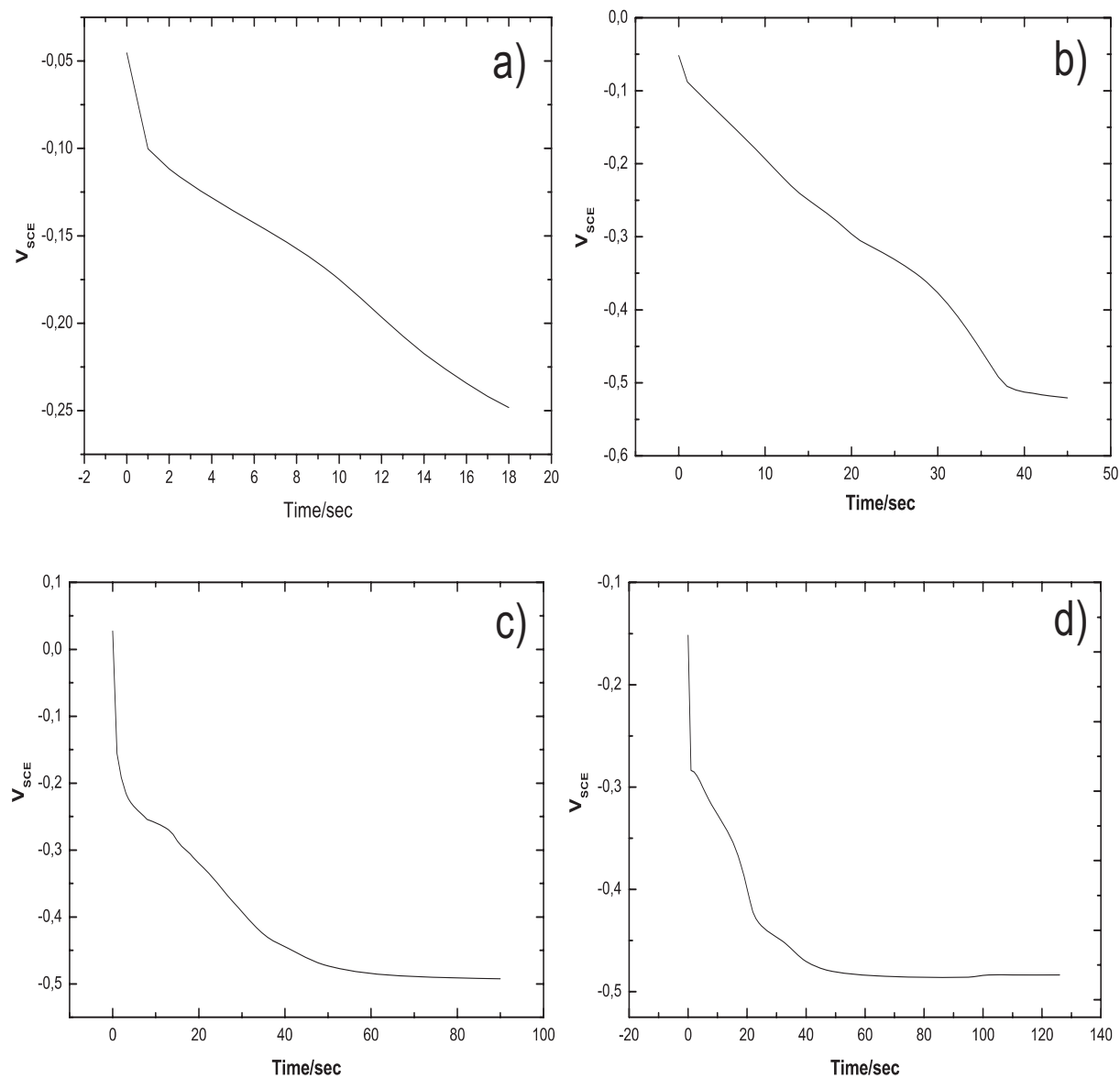


Figure 8.59: Galvanostatic curves obtained for different Cu coverages (a) 10 ML (b) 25 ML (c) 50 ML and (d) 70 ML onto TaS₂ in 0.01 M CuSO₄ + 0.01 M H₂SO₄ solution (current = $0.5 \text{ mA} \cdot \text{cm}^{-2}$, sample area $\approx 16 \text{ mm}^2$).

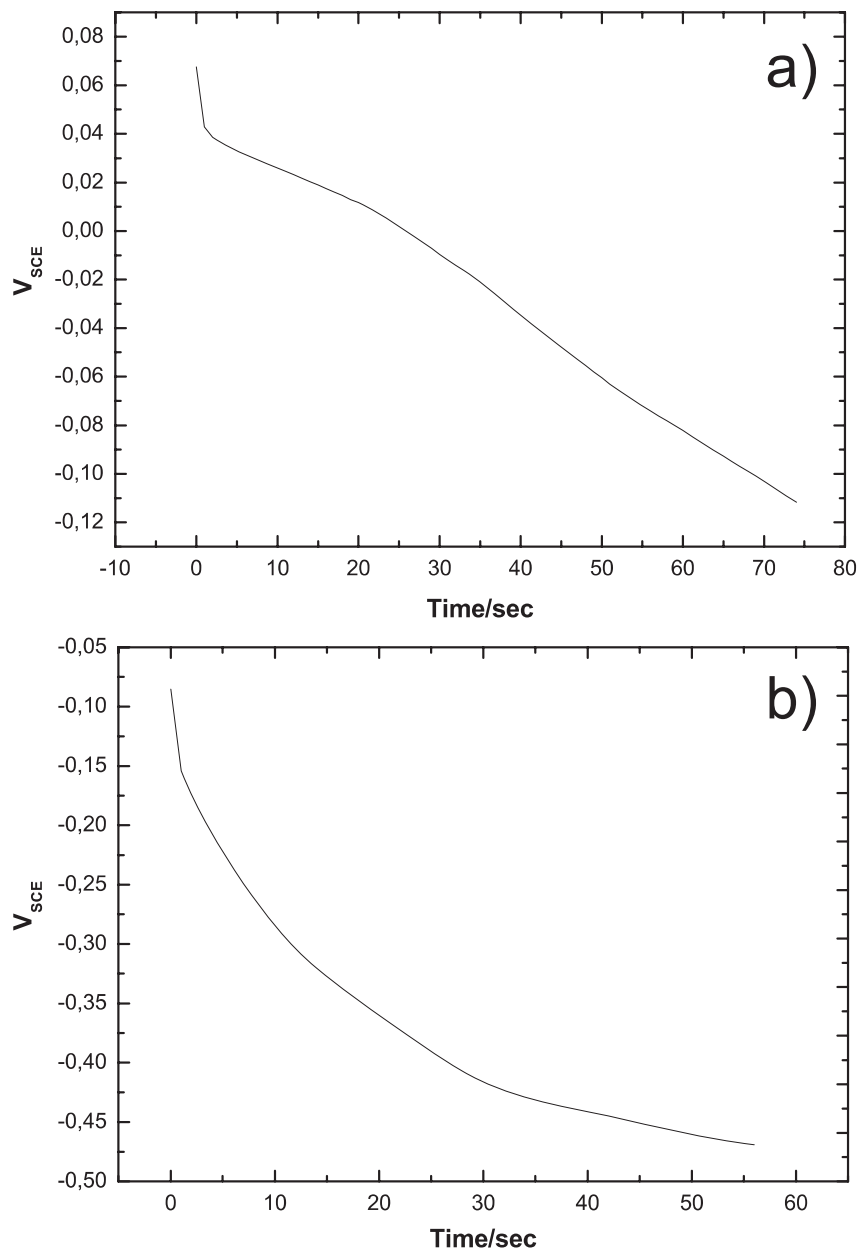


Figure 8.60: Galvanostatic curves at different current densities (a) 0.3 mA·cm⁻² and (b) 0.4 mA·cm⁻² obtained for electrodeposited Cu onto TaS₂ in 0.01 M CuSO₄ + 0.01 M H₂SO₄ solution (total coverage = 25 ML (for fig. 8.60b), sample area ≈ 16 mm²).

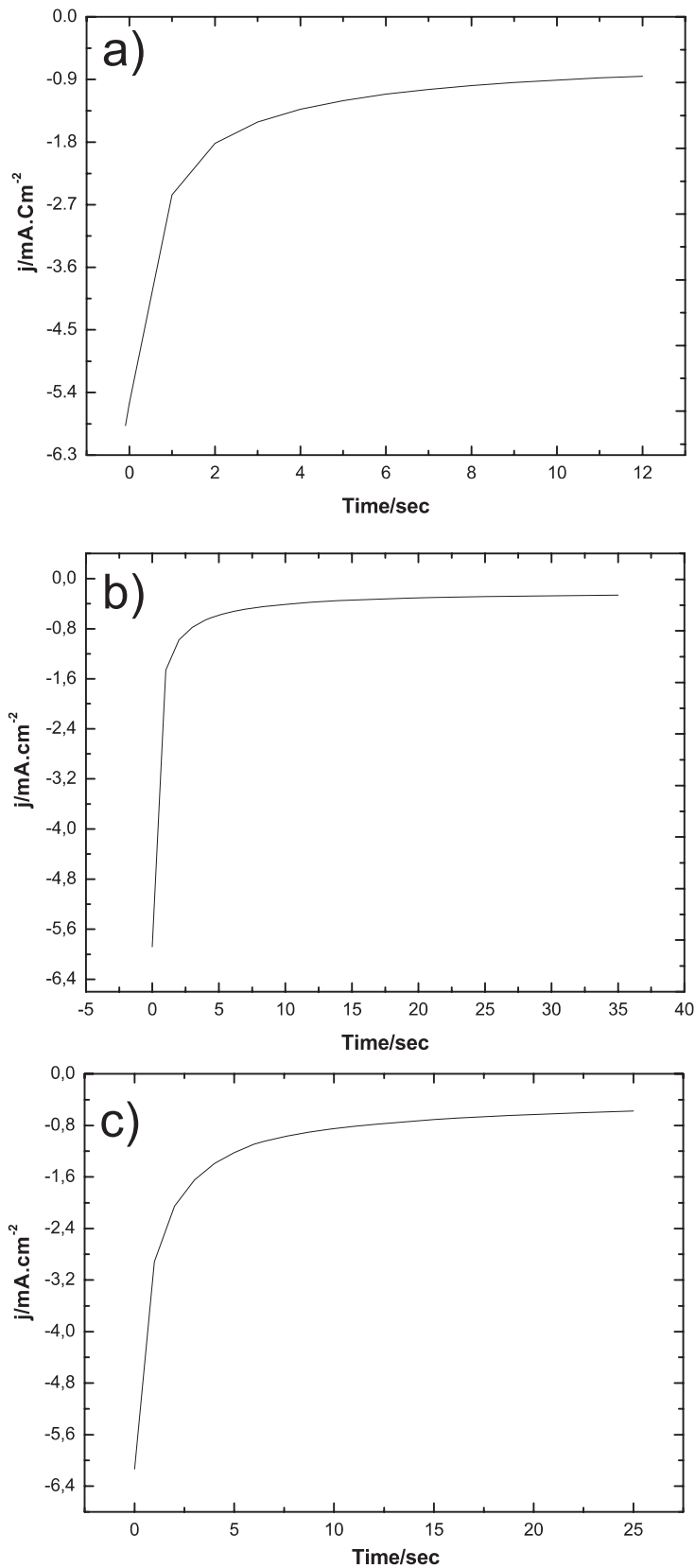


Figure 8.61: Potentiostatic curves at different overpotentials (a), (c) -0.5 V and (b) -0.35 V for electrodeposited Cu onto TaS₂ in 0.01 M CuSO₄ + 0.01 M H₂SO₄ solution.

8.3 Microscopic Characterization of TaS₂ after Cu Deposition

This section summarizes results of a microscopic study of nanostructures formed by deposition of copper onto the basal plane of TaS₂ crystals. Microscopic investigations of the micro- and nanostructure of electrochemical copper deposition (at ambient temperatures and different deposition rate), for different metal coverages onto the TaS₂ surface were carried out using different microscopic techniques such as optical microscopy, scanning electron microscopy (SEM), scanning tunneling microscopy (STM) as well as atomic force microscopy (AFM). The investigations focused on studies of the type, the arrangement and the microstructure of nanostructures over the basal plane of the substrate. For the extremely flat TMDC crystals, one might intuitively expect a simple structure formation after metal deposition like cluster or thin film growth due to the van der Waals termination of the surface. Surprisingly, various different structures varying from buckles in the form of tubes to clusters of micrometer size as well as nanowires, similar to those found under UHV conditions [16, 17] were also observed. All experiments in this chapter were performed on substrates at room temperature. The current chapter is dedicated to the introduction and categorization of the various structures that form during this electrodeposition process. In addition, the effect of the rate of deposition for medium copper coverage on the TaS₂ surface is also presented. Basically we started with a lower coverage of copper (10 ML) and increased the coverage (up to 70 ML) in subsequent experiments. The types of structures formed for different Cu coverages are described in the following section.

8.3.1 Surface Topography of TaS₂ for Lower Cu Coverage (10 ML)

Fig. 8.62a shows a SEM image of a 10ML copper deposited TaS₂ substrate. The deposition is carried out galvanostatically with a current density of $0.5\text{mA}\cdot\text{cm}^{-2}$. Large defect free surface areas (which might also contain small defects not visible with SEM) of several μm^2 separated by macro steps were observed. Along with defects also copper clusters of different sizes were observed on the defect free areas as well as near the macro steps. The large buckling observed on the surface probably formed during sample cleavage by scotch tape. The absence of buckles and nanowires indicates negligible surface stress at a lower (10 ML) copper coverage. The AFM image in fig. 8.62b shows a TaS₂ surface covered with 10 ML of copper. Similar to the SEM images, no nanotunnels or nanowires were observed apart from copper

clusters of different sizes. The average height of these clusters ranges between 10 to 60 nm (fig. 8.62c) whereas average diameters are of the order of μm but might be affected by the AFM tip.

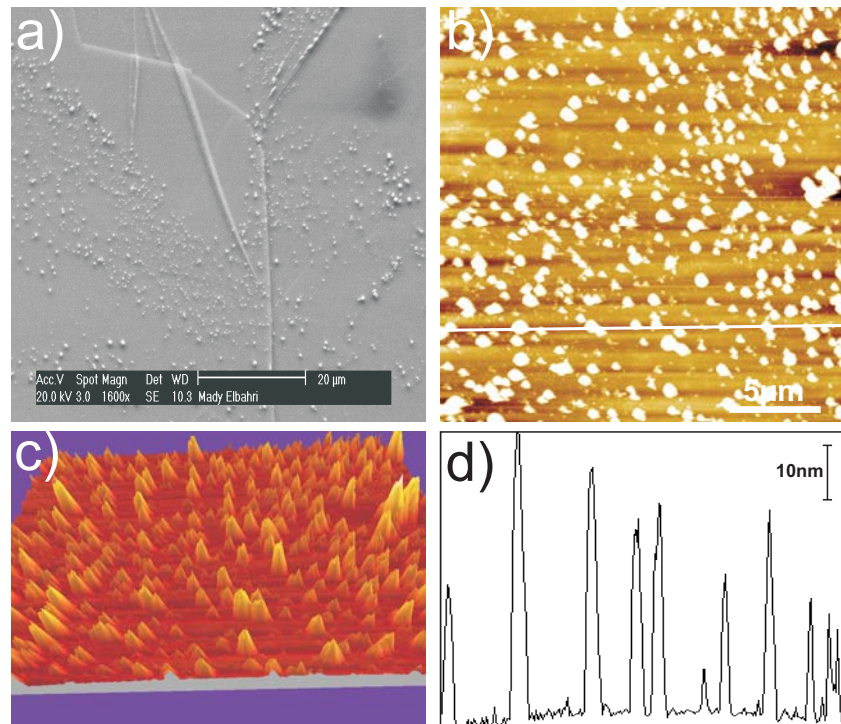


Figure 8.62: Surface morphology of TaS₂, (a) under SEM, (b) under AFM, (c) three dimensional view of fig. 8.62b and (d) heights of nanoclusters along the scan line in fig. 8.62b for 10 ML Cu coverage.

8.3.2 Medium Surface Coverage (>20 ML)

The surface characteristic starts to change with increase in copper coverage. Different structures that formed when the copper coverage increased to > 20 ML are as follows. Fig. 8.63a shows a TaS₂ surface for 30 ML copper coverage. After copper deposition, the surface layers begins to buckle and different networks, i.e. nano tunnels of different sizes (fig. 8.63a) similar to those observed under vacuum deposition (fig. 8.63b) [20] developed. These networks are classified as buckles with sharply defined edges which follows threefold crystal symmetry and buckles having a tube like structure with no sharply defined edge. The formers have widths of about 1-2 μm with a typical mesh size of 50 to 100 μm whereas the widths in case of latter structures varies between 1 to 5 μm with a typical mesh size of 10 to 100 μm . In fig. 8.63c and d, these different buckle networks are schematically represented in order to obtain a better understanding of their structures and differences. The network having sharply defined edges can

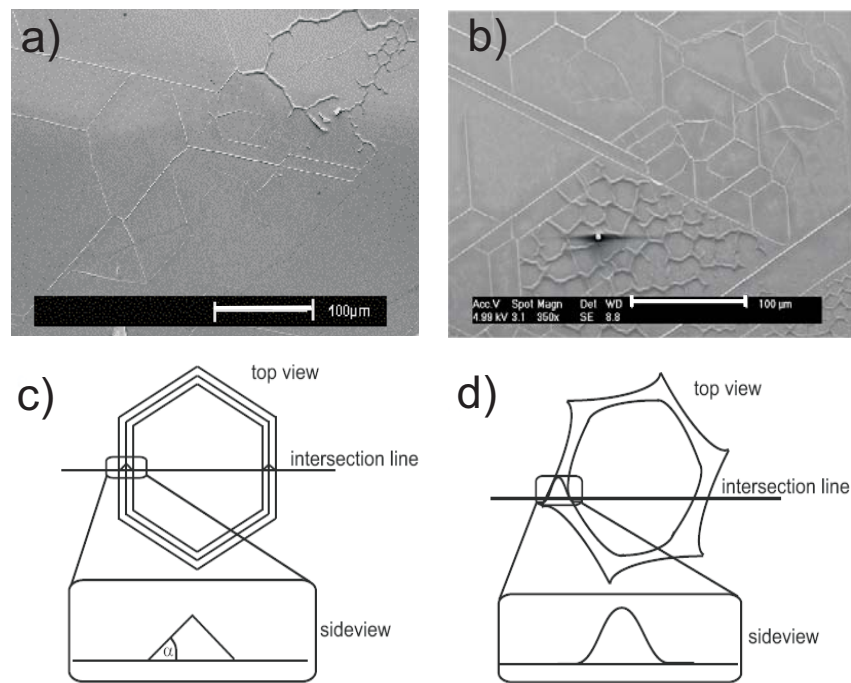


Figure 8.63: Comparison of SEM images of TaS₂ for 30 ML Cu coverage (a) formed by electrodeposition (b) under UHV condition [20], (c) and (d) side view schematics of the two different nano tunnels (taken from [20]).

be considered as unfolded surface layers with straight sides having a certain angle α . Their orientation follows the hexagonal crystal symmetry. The larger tube like network possesses no sharp edges and follows a weak three fold symmetry.

AFM images of TaS₂ surface for 25 and 30 monolayer (ML) copper coverages are shown in fig. 8.64a, b. Large flat areas covered with a homogenous Cu film along with the sharp edged nanotunnels were clearly observed. Fig. 8.64c, d represents three dimensional views of these nanotunnels showing that not only flat surface areas but also the nanotunnels are covered with copper clusters. The average height and width of these nanotunnels are ≈ 600 nm and $2 \mu\text{m}$ for both 25 ML and 30 ML (see fig. 8.64e, f) Cu deposited surface. In addition, the size of copper clusters in the flat areas varies between 20 to 100 nm. Ex-situ STM images (fig. 8.65) show, that these grains are on a smaller scale covered by very small structures, which probably are grains of a Cu-oxide film, formed after emersion of the samples in air.

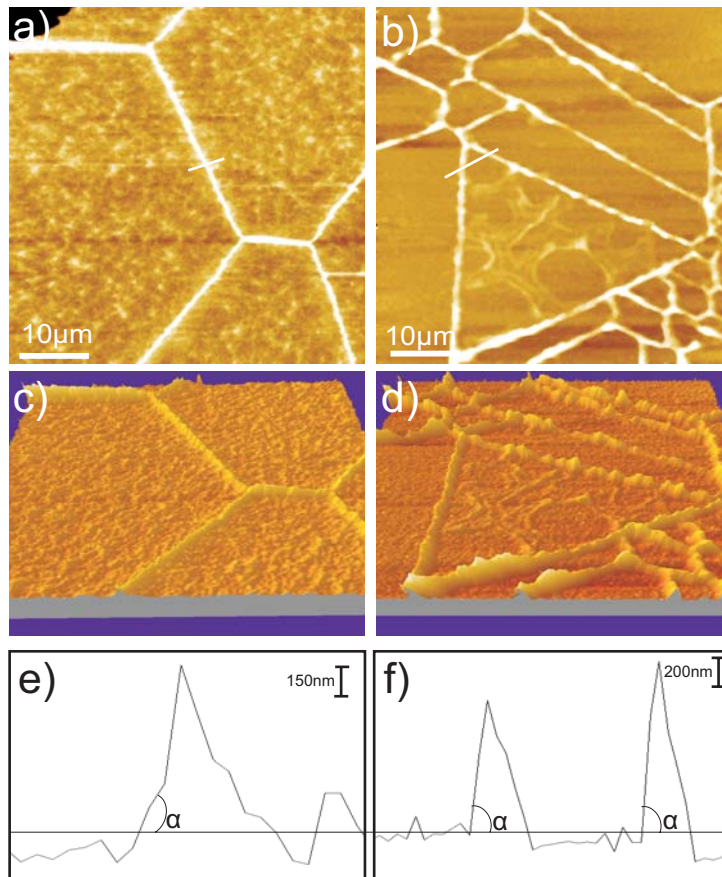


Figure 8.64: AFM images of TaS₂ for different coverages of Cu, (a) 25 ML, (b) 30 ML, (c), (d) three dimensional view and (e),(f) heights of nano tunnels taken along corresponding scan lines.

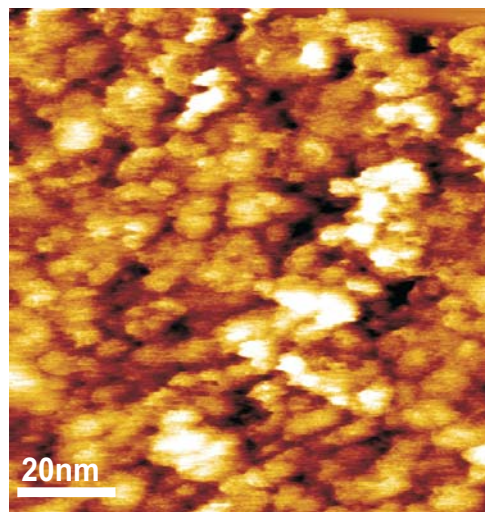


Figure 8.65: STM image showing the flat areas in fig. 8.64a covered with copper oxide film.

Atomic force microscopy images shown in fig. 8.66 for a 30 ML copper coverage were observed in an experiment but its reproducibility can not be guaranteed. Like the nanotunnels, these structures are also hexagonal in nature and seem to terminate as tips. Higher magnification images in fig. 8.66b clearly shows these nanostructures were also covered with copper clusters. The average heights of these nanostructures vary approximately in between 500 nm to 900 nm and the widths are $\approx 4\mu\text{m}$ (fig. 8.66c). The reason of formation of such structures which seem to be formed by the collapse of large tunnels in currently unknown.

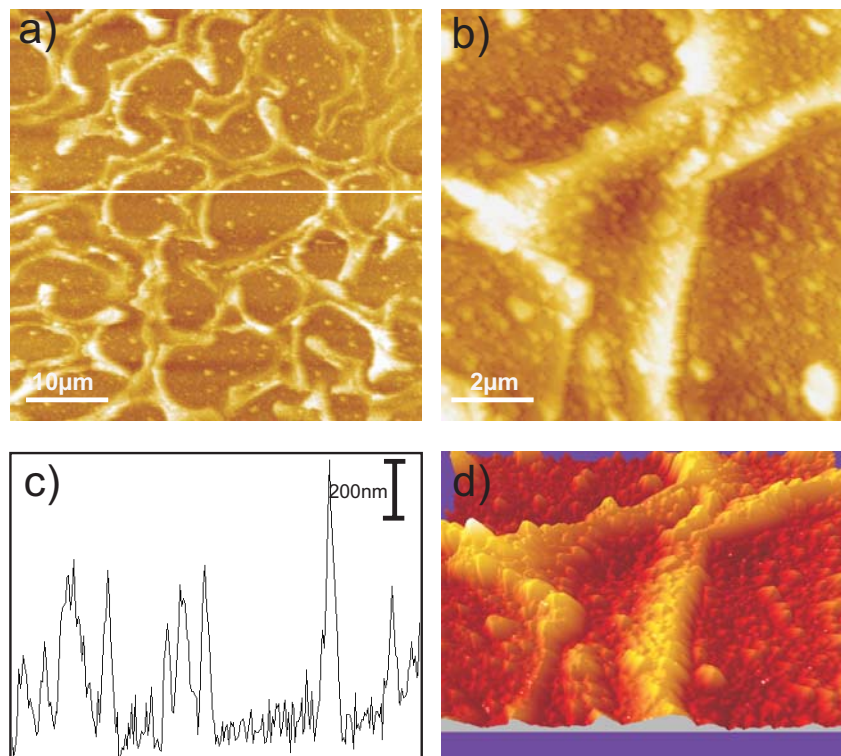


Figure 8.66: AFM image of structures first time observed in TaS₂ for 30 ML Cu coverage. Image (a), (b) showing these hexagonal structures (c) height along the corresponding line in fig. 8.66a and (d) 3 dimensional view of fig. 8.66b.

Fig. 8.67a shows another feature of the substrate for medium Cu coverage. As can be seen here, the individual networks are typically entangled in a complex manner, and it appears that they overlap and grow on top of existing nanostructures. Fig. 8.67a, in particular, can be interpreted as nanotunnels forming under an existing network of other nanotunnels. This observation confirms that such Cu coverages cause a hierarchy of rather independent networks of linear nanostructures. Similar observations were also made by Kunz [20] in vacuum deposition (see fig. 8.67b). In addition, nanoclusters of differ-

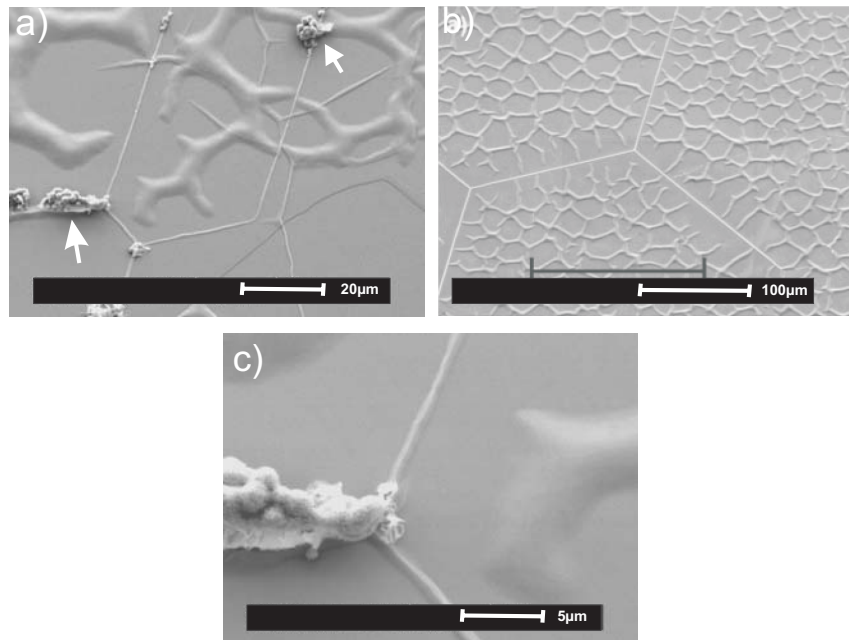


Figure 8.67: SEM images showing the hierarchical nature of nano tunnels. Images (a), (c) formed after electrodeposition and (b) after vacuum deposition (taken from [20]).

ent dimensions were also observed over these nanotunnels (see arrows in 8.67a). Higher magnification image (see fig. 8.67c) indicates the nanoclusters are inhomogeneous and are formed as agglomeration of Cu clusters of different sizes.

Apart from nanotunnels and nanoclusters, Cu wires having width and length of $\approx 1 \mu\text{m}$ and several $100 \mu\text{m}$ were also observed (see fig. 8.68). Taking a closer look at the Cu wires (fig. 8.68b, c), they also seem to form in an inhomogeneous manner where Cu clusters of different sizes agglomerated to form such long range wires. The formation of such long range Cu wires is probably due to nucleation of Cu atoms at the defects, such as macrosteps. The dendritic nature of these deposited copper clusters, are visible in fig. 8.68c. Similar dendritic growth has been reported by Kunz [20] for vacuum deposition of Cu onto TaS₂. An EDX spectra shown in fig. 8.68d indicates the flat area (see red arrow in fig. 8.68c) also covered with Cu clusters.

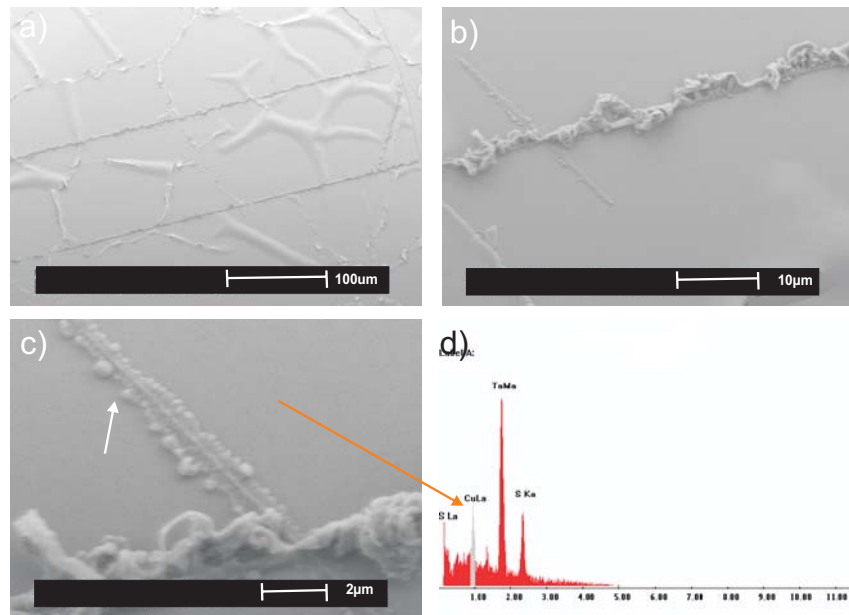


Figure 8.68: SEM images (a), (b), (c) showing long range Cu wires and (d) EDX spectra showing the flat areas also covered with Cu.

8.3.3 Higher Surface Coverage (≥ 50 ML)

At higher coverages there is no other drastic change observed except for the increase in number, height and width of these buckles. Fig. 8.69 shows the surface morphology for a 50 ML copper covered TaS₂ surface. All the different structures e.g. large and small tube shaped buckles as well as nanotunnels having sharply defined edges, were clearly observed. The crossover nature of nanotunnels is also observed in fig. 8.69a. The height and width of the large irregular buckles are between 600 to 800 nm and ≈ 5 μm. Due to their large scale dimensions, it was also possible to observe these structures under the optical microscope. Although it is not possible to resolve nanoscopic details of the structure, the polygonal networks are clearly visible (see fig. 8.70a, b).

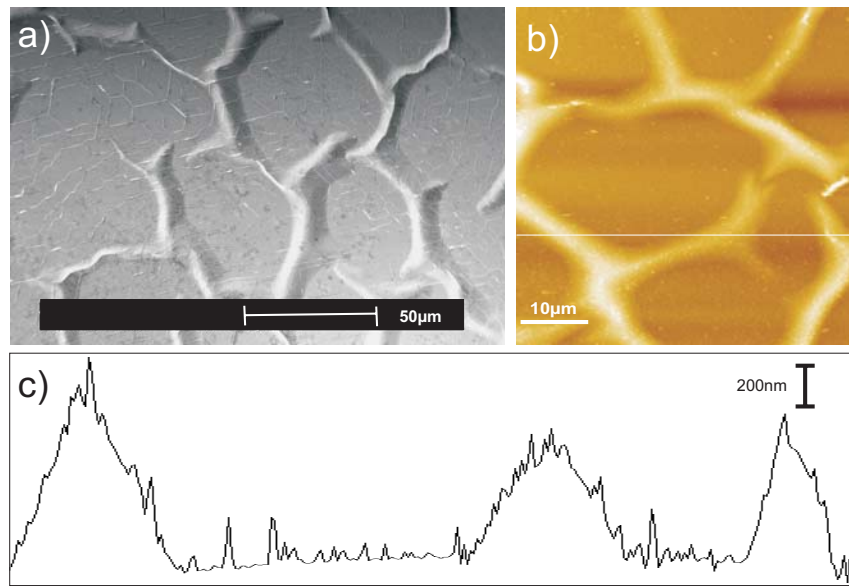


Figure 8.69: SEM and AFM images of TaS₂ for 50 ML Cu coverage. Image (a), (b) showing different nanotunnels and (c) showing height along the corresponding scan line in fig. 8.69b.

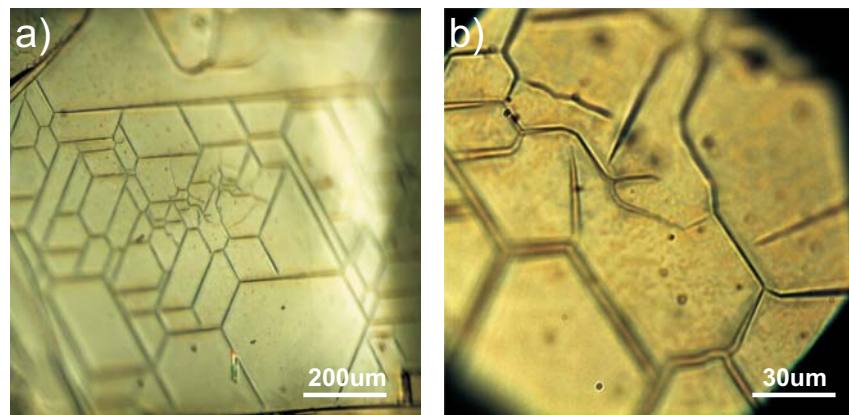


Figure 8.70: Optical microscope images of the TaS₂ surface for 50 ML Cu coverage at different magnification.

Similar structures were also formed for 70 ML Cu coverage (see fig. 8.71), where height and width of nano tunnels are $\approx 1 \mu\text{m}$ and $5 \mu\text{m}$, respectively.

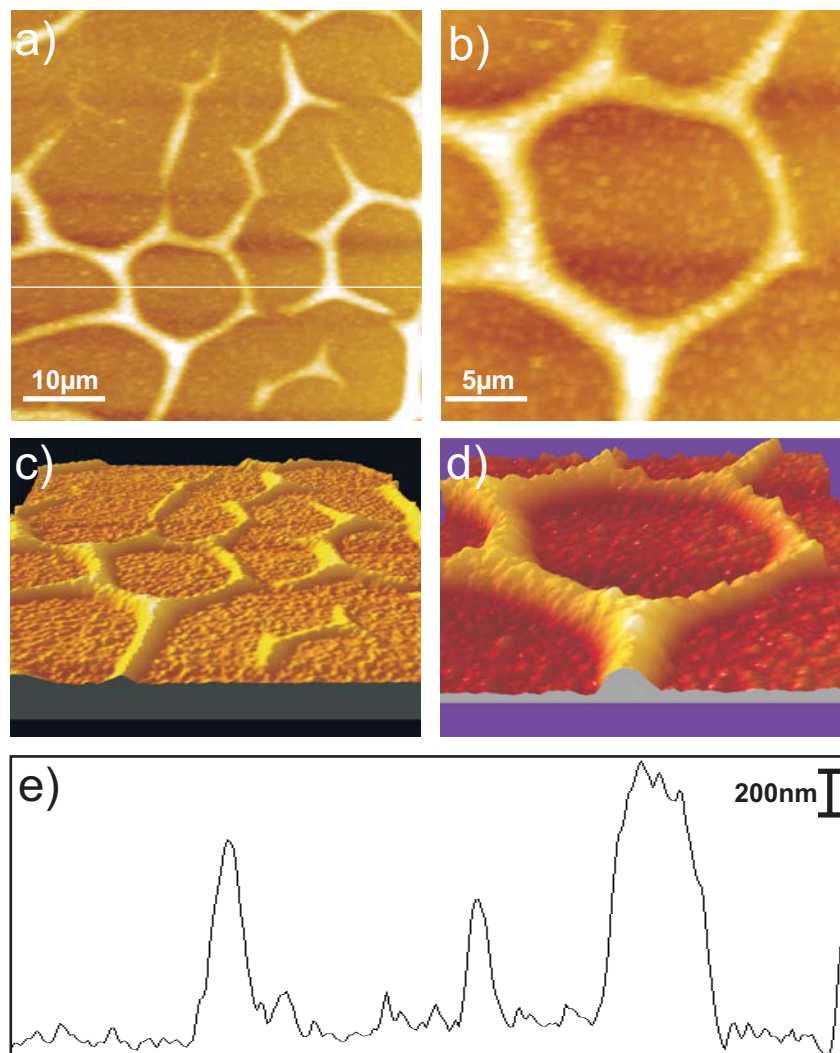


Figure 8.71: AFM images of TaS₂ for 70 ML Cu coverage. Image (a), (b) showing the buckle networks, (c), (d) 3 dimensional views of fig. 8.71a, b and (e) height along the corresponding scan line in fig. 8.71a .

8.3.4 Potentiostatic Bulk Cu Deposition

Potentiostatic bulk deposition experiments at different overpotentials were also carried out for different copper coverages in order to compare the morphology with those formed under galvanostatic condition. Different structures that formed are described below.

Fig. 8.72 shows AFM images of Cu deposited TaS₂ surface after keeping the potential at -0.35 V for 35 sec. The total charge passed during this time was 4120 μC which is equivalent to about 28 ML of copper. As observed in fig. 8.72, the surface is covered with a homogeneous film of Cu and no surface

deformation e.g. nanotunnels were observed. At this point it is important to note that after keeping the sample under ambient conditions for almost a day, nanotunnels were observed on the surface.

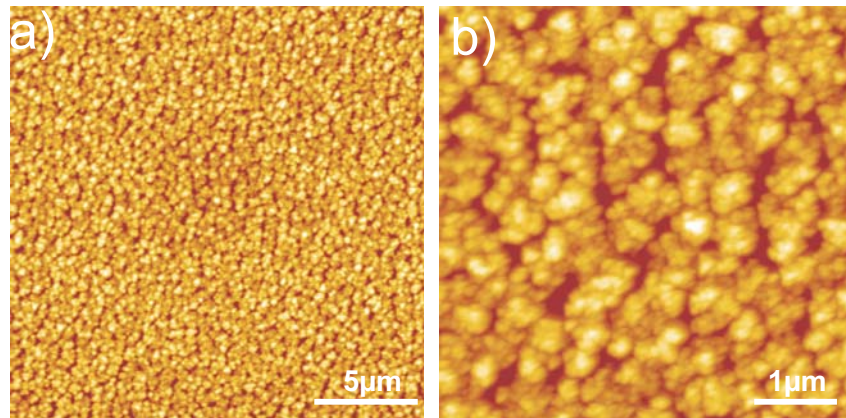


Figure 8.72: Surface morphology of TaS₂ after potentiostatic deposition (potential = -0.35 V) for \approx 28 ML Cu coverage.

Similar experiments were also carried out at a more negative potential (-0.5 V) for different time periods of 12 and 25 sec (see fig. 8.73 and 8.74). The total charges were 835 μ C (surface area \approx 9 mm²), 4190 μ C (surface area \approx 16 mm²) respectively and are equivalent to about 11 ML and 29 ML of Cu. The nanotunnels were formed only after \approx 35 hours for 11 ML copper coverage (fig. 8.73), whereas in case of 29 ML copper coverage (fig. 8.74) nanotunnels were formed within 5 minutes after electrodeposition. In addition, isolated copper clusters and a homogenous copper film for fig. 8.73 and fig. 8.74 are observed in the planar areas.

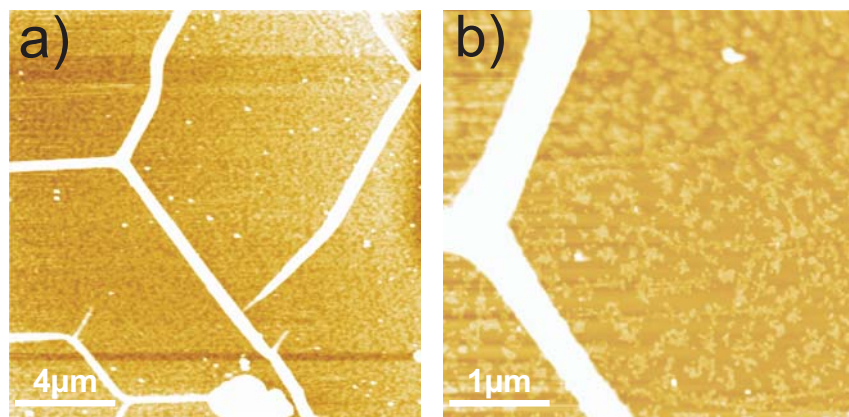


Figure 8.73: Surface morphology of TaS₂ after potentiostatic deposition (potential = -0.5 V) for \approx 11 ML Cu coverage.

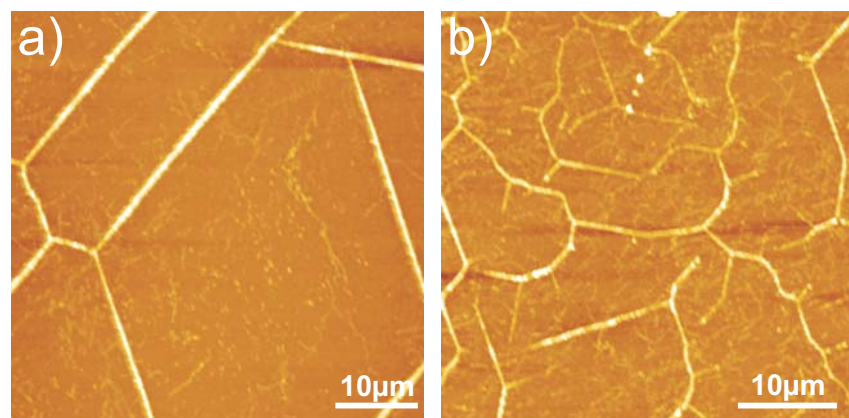


Figure 8.74: Surface morphology of TaS₂ after potentiostatic deposition (potential = -0.5 V) for \approx 29 ML Cu coverage.

In order to observe the nanotunnel formation at higher overpotential (-0.5 V) optical microscopy was performed minutes after depositing copper (see fig. 8.75). The total charge passed during the experiment was 3450 μC , equivalent to \approx 25 monolayers (ML) of Cu. The nanotunnels started to evolve within minutes. The series of images shown in fig. 8.75 clearly demonstrates the evolution of nanotunnels as a function of time. It gives a clear indication that nanotunnel evolution is a progressive process directly after electrodeposition and does not occur during deposition. After waiting for longer time periods (about 30 minutes), the nanotunnel evolution slowly ceases and no further change was observed.

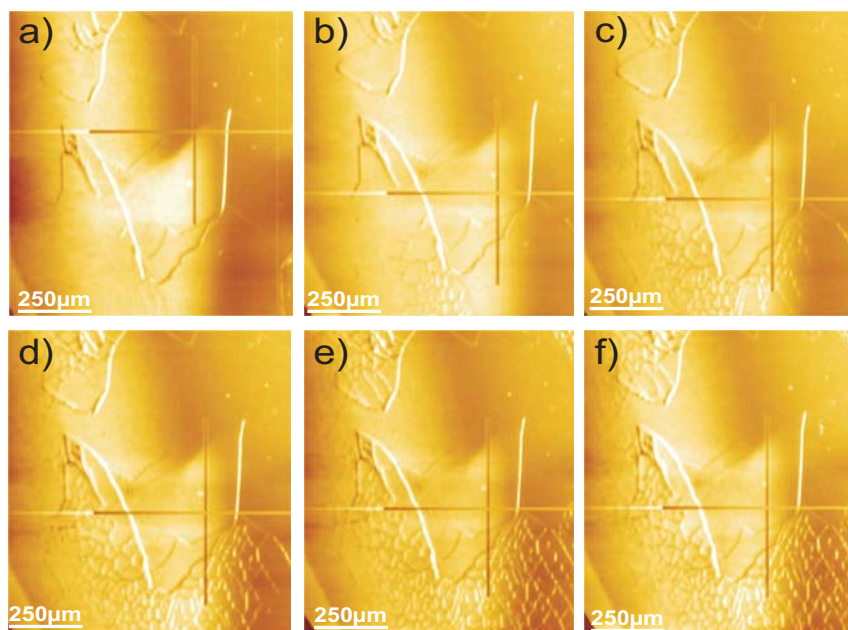


Figure 8.75: Ex-situ optical microscopic images of TaS₂ covered copper at different times (a) 3 min. (b) 7 min. (c) 10 min. (d) 15 min. (e) 30 min. and (f) 90 min. after potentiostatic deposition and emersion from the electrolyte (potential = -0.5 V, total deposited ML \approx 25).

8.3.5 Galvanostatic Deposition at Different Deposition Rates

The previous sections showed various structures formed during galvanostatic as well as potentiostatic bulk deposition of Cu onto TaS₂. In order to have a better understanding of the growth of these nanostructures, galvanostatic Cu deposition was also performed at different current densities.

Fig. 8.76a and 8.76b are AFM images of TaS₂ covered with 25 monolayers (ML) of Cu formed by applying a current density of $0.4 \text{ mA}\cdot\text{cm}^{-2}$ (potential transient see fig. 8.60b). Large copper nuclei whose heights are $\approx 150 \text{ nm}$ were observed (fig. 8.76a). The rather non-uniform distribution of these nuclei might be related to the preferential nucleation at defects present in the substrate (not visible on μm scale). Higher magnification images (see fig. 8.76b) clearly demonstrate the dendritic nature of these nuclei. Fig. 8.77 shows another region of the substrate, where long chain dendritic wires extending over several μm were observed.

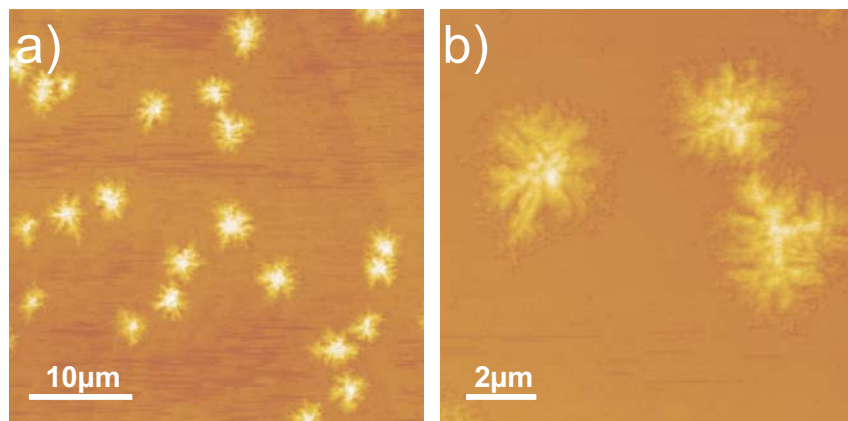


Figure 8.76: AFM images of individual dendritic structures formed at a lower current density ($j = 0.4 \text{ mA}\cdot\text{cm}^{-2}$).

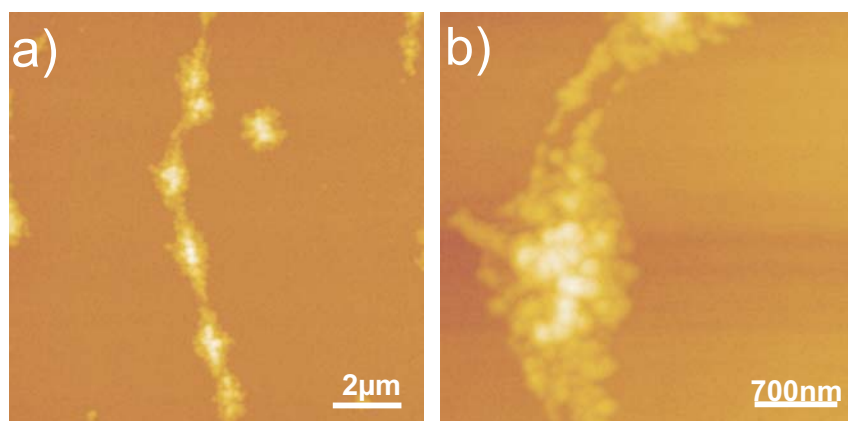


Figure 8.77: AFM images of long chains of dendritic structures formed at a lower current density ($j = 0.4 \text{ mA}\cdot\text{cm}^{-2}$).

By applying a lower current density of $0.3 \text{ mA}\cdot\text{cm}^{-2}$, large number of copper clusters were found on the surface (see fig. 8.78a). The height distribution of these clusters are similar to those observed by galvanostatic deposition of 10 ML Cu onto TaS₂ surface at a current density of $0.5 \text{ mA}\cdot\text{cm}^{-2}$ i.e 10-50 nm. Higher magnification image in fig. 8.78b shows an almost continuous film of small Cu clusters. The potential transient (see fig. 8.60a) which terminates at -0.12 V , gives a clear indication that no bulk Cu deposition occurred in this regime. It is not clear at this point what kind of process leads to the formation of such clusters.

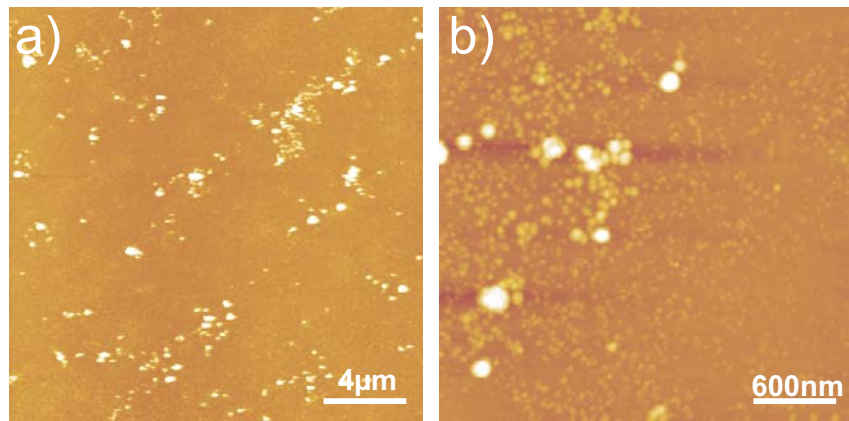


Figure 8.78: AFM images showing only Cu clusters at a lower current density ($j = 0.3 \text{ mA}\cdot\text{cm}^{-2}$). Images were taken directly after electrodeposition

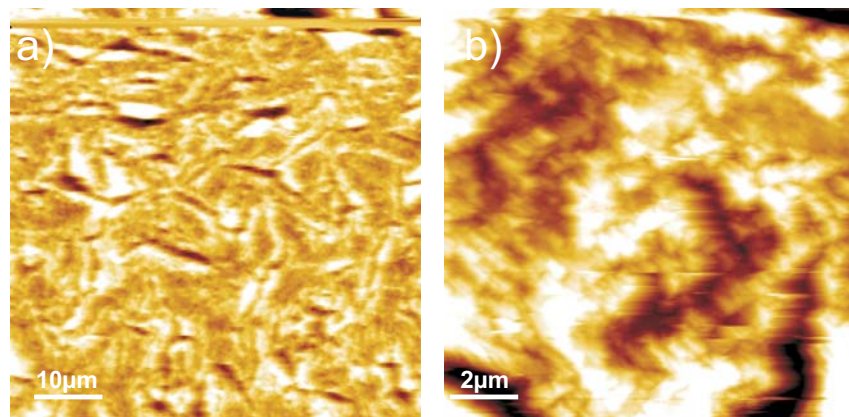


Figure 8.79: AFM images showing surface cracks at higher current density ($j = 3 \text{ mA}\cdot\text{cm}^{-2}$).

Applying a much higher current density of $3 \text{ mA}\cdot\text{cm}^{-2}$ results in surface disintegration and formation of large nanocracks (see fig. 8.79) which might be due to both bulk Cu intercalation as well as hydrogen evolution. The total charge passed during deposition was $2160 \mu\text{C}$ which is equivalent to 27 ML of Cu (surface area $\approx 9 \text{ mm}^2$). The average measured height of these cracks varies between 2 to 3 nm, but this might be due to the large AFM tip curvature resulting in erroneous height measurements. It is important to note that at such high current density, bulk Cu deposition occurs well below hydrogen evolution potential i.e. lower than -0.7 V .

8.4 Discussion

The nanostructures (e.g. nanotunnels, nanowires, nanoclusters) formed on TaS₂ upon Cu electrodeposition strongly resemble those reported in previous studies where Cu was deposited on TaS₂ under UHV conditions [18, 20]. In both cases the resulting structures are of similar shape, i.e. straight nanotunnels with prismatic shape as well as more irregular buckles, have comparable widths and heights, and a mesh size of several micrometer. These structural similarities suggest a similar physical origin of this phenomenon in both environments. The following factors might be responsible for the formation of nanotunnels :

1. Lattice deformation induced by Cu intercalation.
2. Lattice deformation induced by stress relaxation of the Cu thin film after deposition.

In order to rationalize deposition induced nanotunnel formation during vacuum deposition Adelung et al. [17, 18] and Spiecker et al. [21] suggested a deposition-induced expansion of the dichalcogenide surface layers via a mechanism where electron transfer from adsorbates (Cu) alters the equilibrium lattice parameter of the uppermost TaS₂ triple layer. Density functional theory calculations for a similar system (Li/TiSe₂) revealed a significant expansion of the equilibrium lattice parameter after the deposition of 1/3 monolayer [131], thus causing compressive stresses. In a simplified picture, a positively charged metal atom on the surface attracts the chalcogen atoms "S" of the uppermost TaS₂ triple-layer, which are electron receptors, while repelling the transition metal atom X, which is an electron donor, but a weaker one than the metal atom on the surface. This interaction causes an expansion of the equilibrium lattice parameter at the surface, leading to compressive in-plane stresses in the uppermost surface layer under the constraints of an extended TaS₂ crystal resulting in a folding of these layers. The latter is facilitated by the weak van-der-Waals binding between the layers, which permits sliding of the layers with respect to each other. Later on Spiecker et al. [132] have demonstrated that along with the in-plane compressive stress, adsorbate induced intercalation also plays an important role in folding of these layers.

In the case of electrochemical deposition an intercalation-driven lattice expansion seems the most likely explanation for the observed behaviour. In particular, nanotunnel formation seems to require (or at least is strongly enhanced by) deposition potentials close to -0.5 V, where the electrochemical data

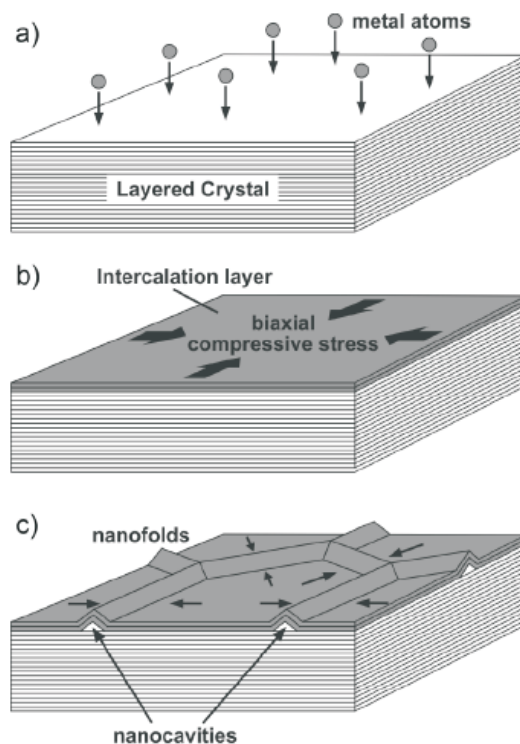


Figure 8.80: Formation of networks of nanofolds with cavities upon vacuum metal intercalation into layered crystal surfaces during continuous metal deposition. For details, see text (taken from [132]).

indicates the onset of Cu intercalation. As already pointed out previously [132], copper intercalation into transition metal dichalcogenides often results in an expansion within the layers on the order of a few percent. Although unfortunately no data on Cu intercalation in 1T-TaS₂ exists, a study on Cu intercalates of 2H-TaS₂ revealed an in-plane layer expansion (from 3.315 Å to 3.34 Å) of 0.75 % as compared to pure 2H-TaS₂ [133].

The surprising observation that the nanotunnels always form not during, but (up to several days) after film deposition and emersion of the samples from the plating solution may be related to the slow kinetics of the intercalation process, which typically occurs at much slower timescales than deposition. However, the pronounced dependence of the postdeposition period over which the nanotunnels emerge on the deposition conditions is more difficult to rationalize. Apparently, Cu predominantly intercalates during this period (i.e. in air) into the TaS₂ lattice and this process can even proceed (albeit slower) if the electrodeposition is performed at potentials, where no electrochemical intercalation occurs. This notion is in accordance with the mechanism proposed by Spiecker et. al. for Cu deposition under vacuum

conditions [132]. The main role of electrochemical intercalation seems to be a pronounced enhancement of the postdeposition intercalation process, potentially via the creation of defects that promote the entry of Cu into the substrate lattice. Evidence for the latter comes from our high-resolution in situ STM study of pyridine intercalation into TaS₂, which clearly demonstrates the formation of nanoscale defects during intercalation /deintercalation process (see chapter 6.4.3.2).

Other mechanisms of Cu-induced lattice expansion seem less likely. A lattice expansion due to electronic interactions with adatoms should occur instantaneously and seems incompatible with the slow postdeposition formation of the tunnels. Several authors have also reported intrinsic stress in electrodeposited thin films of Cu. Haiss et al. [134] reported a low mobility Volmer-Weber growth for electrodeposited Cu on Au from acidic CuSO₄ solution involving tensile stress that varies directly with number of deposited monolayers (upto 25 ML) of Cu. Kongstein [135] extended the idea of Haiss for higher copper coverage and found that maximum tensile stress occurs at about a copper coverage of 75 ML at higher overpotentials (-0.25 V) and it remains tensile for coverages up to 250 ML. At coverages higher than 250 ML, a change in stress from tensile to compressive are observed. Since the copper coverages in our experiments are below 100 ML, the stress generally associated is tensile in nature. The question comes to mind how a system involving tensile stress results in the formation of buckles which are results of compressive stress as demonstrated by Spiecker et al [21]. The answer might be due to a stress relaxation of the deposited film. Kongstein et al. have observed such a stress relaxation of the electrodeposited Cu film on Au [135]. In order to compare, whether the stress associated with such film relaxation would result in the formation of nanotunnels, we have calculated the stress associated with the formation of nanotunnels, in the following way:

For this analysis, images which show only prismatically shaped nanotunnels, for example, fig. 8.64a and b having heights and widths of ≈ 600 nm and $2 \mu\text{m}$, were taken into account. Assuming that, such nanotunnels are combinations of isocoles triangles of height h_i and base width w_i , extending over a distance of length L_i (see fig. 8.81), we have calculated the total increase in surface area by the following formula.

$$\Delta A = \sum_i (2 \sqrt{(h_i^2 + (w_i/2)^2} - w_i) \cdot L_i \quad (8.33)$$

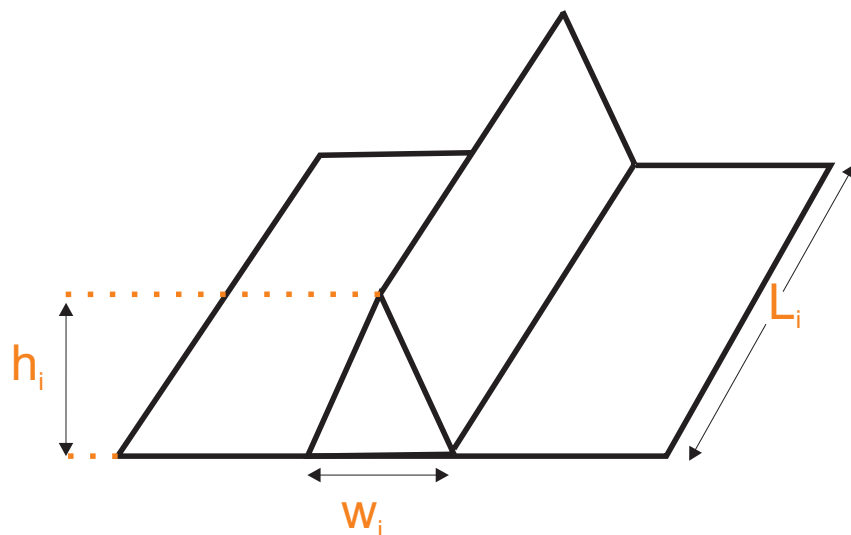


Figure 8.81: Schematics of a nanotunnel used for calculation of surface area change and stress associated with the nanotunnels.

The total increase in surface area was found to be $40.1 \mu\text{m}^2$ and $46.8 \mu\text{m}^2$ for fig. 8.64a and b respectively. By dividing this change in surface area through the AFM scan size (the surface roughness of the bare TaS₂ substrate is negligible), a surface strain of 0.025 and 0.029 is found for fig. 8.64a and b, respectively. A similar order of magnitude in surface strain can be estimated for most of the nanotunnel networks observed in this study. Assuming the Young's modulus as 115 GPa for polycrystalline copper [136], the stress associated with these nanotunnels would be ≈ 2.87 GPa and 3.35 GPa respectively. Kongstein et al. [135] have demonstrated that for electrodeposited Cu on Au, tensile stress reaches a maximum value for ≈ 15 nm Cu film (i.e. ≈ 75 ML of Cu assuming diameter of copper atom = 0.209 nm [137])(see fig. 8.82) when deposited at an overpotential of - 0.25 V. The stress relaxation for this lower Cu coverage is ≈ 100 MPa (insert in fig. 8.82, red arrow) which is $\approx 3\%$, the stress relaxation needed for nanotunnel formation (≈ 2.87 GPa and 3.35 GPa for fig. 8.64a and b) and hence practically negligible.

Scanning electron microscopy (SEM) and Atomic force microscopy (AFM) also revealed, the formation of Cu nanowires and nanoclusters on TaS₂ during electrodeposition (e.g. see fig. 8.68, fig. 8.76 etc.). Adelung et al. demonstrated by scanning tunneling microscopy (STM) and AFM studies, that these nanowires are embedded in the surface cracks of the substrate [16]. In order to rationalize nanowire formation during vacuum deposition, they have proposed a mechanism where the initial compressive stress

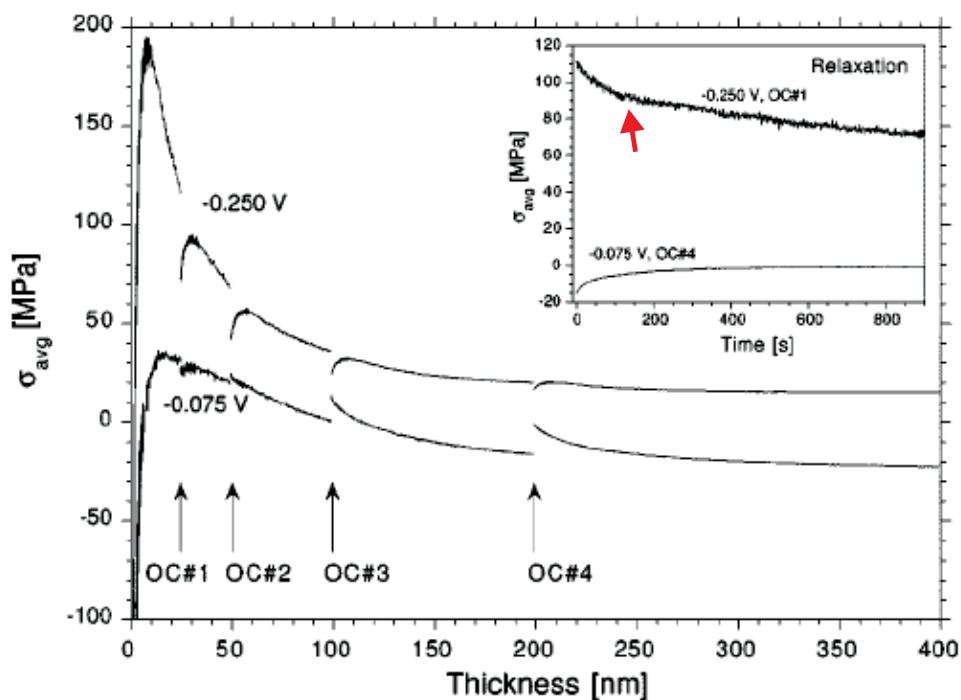


Figure 8.82: Average film stress in copper deposited onto (111) textured Au in $0.1 \text{ mol.L}^{-1} \text{ H}_2\text{SO}_4 + 10 \text{ mmol.L}^{-1} \text{ CuSO}_4$, as a function of deposit thickness up to 400 nm at deposition potentials of -0.075 V and -0.25 V . Deposition was interrupted to open circuit for 15 min at a deposit thickness of 25, 50, 100, and 200 nm. Inset shows stress relaxation for -0.25 V, OC\#1 and -0.075 V, OC\#4 (taken from [135]).

associated with TaS₂ due to the adsorbed Cu atoms undergoes a transition of compressive to tensile stress at a critical thickness of deposited Cu film and thus resulting in the formation of cracks. These cracks are preferential nucleation centers for the further growth of Cu atoms and ultimately growth of copper atoms within these cracks results in the formation of nanowires.

The observation of nanowires and nanoclusters on defect free areas i.e. in the absence of any microcracks (see fig. 8.76, fig. 8.77) during electrodeposition in our studies seems to rule such a process out. However, defects i.e. nanocracks (not visible in μm scale) induced by Cu intercalation on TaS₂ surface might be responsible for the formation of such nanowires and clusters. Defect formation in TaS₂ during intercalation of pyridine molecule are discussed in previous chapter (see chapter 6.4.3.2). Similar defects formed by Cu intercalation might function as the preferential nucleation centers for deposited copper to form nanoclusters and nanowires.

9 Summary on Cu deposition onto TaS₂

To conclude, liquid phase Cu deposition on to TaS₂ also leads to the formation of similar self organised linear nano structures consisting of networks of nanowires and nanotunnels as found under UHV conditions. Specifically following observations were made :

1. Galvanostatic deposition for lower Cu coverages (10 ML), where the potential is terminated at -0.25 V, results in the formation of nanoclusters whereas similar Cu coverages (\approx 11 ML) under potential deposition condition (-0.5 V) results in formation of nanotunnels almost after 35 hours, showing the importance of high overpotentials (where intercalation competes with deposition) for the induced nanotunnel formation.
2. At higher Cu coverages ($>$ 20 ML), nanotunnels were observed both under galvanostatic as well as potential deposition conditions. Increasing the Cu coverage not only increases the width of the nanotunnels but also leads to the formation of more nanotunnels which are arranged in a hierarchical manner.
3. The time dependent evolution of nanotunnels at different overpotentials is an indication of an intercalation driven mechanism, where rate of intercalation which is kinetically driven depends strongly on the applied overpotential. At higher overpotential (- 0.5 V), intercalation is faster thus resulting in the formation of nanowire within minutes whereas at lower overpotential (-0.35 V) where rate of intercalation is slower. the nanotunnel evolution takes almost a day.

10 Conclusion

The aim of the present work was to investigate the nanoscale mechanism of intercalation of organic molecules as well as electrodeposition of copper onto Transition metal dichalcogenides (TMDCs). Different TMDCs e.g., TiSe_2 , NbSe_2 and TaS_2 as well as different organic electrolytes e.g., octylamine and pyridine at pH 3 were employed in our experiments. A number of experimental techniques which includes cyclic voltammetry, in-situ scanning tunneling microscopy (constant current mode), atomic force microscopy (both contact and tapping mode) as well as scanning electron microscopy were used. Experimental problems, e.g. surface oxidation in TiSe_2 in organic electrolyte and failure to clamp NbSe_2 samples inside electrochemical cell due to their small dimensions prevented us doing further experiments. Therefore most of the results were obtained for TaS_2 samples.

TaS_2 in H_2SO_4 :

In H_2SO_4 electrolyte, TaS_2 sample exhibits a stable morphology for the entire potential regime (0 to -0.7 V) demonstrated by in situ scanning tunneling microscopy. The step height also remains constant indicating no intercalation of H^+ ion.

TaS_2 in Octylamine and Pyridine at pH 3 :

At higher tunneling currents 1nA or higher, a stepflow etching of TaS_2 occurs at the double layer regime (-0.22 V) in both octylamine and pyridine electrolyte. However, at lower tunneling current i.e. at 0.2 nA , no surface etching was observed in double layer regime in both electrolytes.

In both octylamine, pyridine electrolyte surface etching at defects (e.g., pits, step edges) starts at a potential of -0.44 V, which is attributed to the adsorption of organic molecules resulting in weakening of atomic bonding and etching by tip interaction.

However, on moving to lower potential (-0.68V) , except for surface etching no other morphology change was observed for octylamine. The step height measurement indicated a constant value ($0.56 \pm 0.03\text{nm}$) for the entire potential regime indicating no octylamine intercalation. Ex-situ AFM measurements at still lower potential (-0.75 V) indicated the formation of islands (0.6 nm and multiples higher) as well as a step height increase of 0.5 nm indicating parallel orientation of octylamine.

In case of Pyridine at -0.68V, two different kinds of islands i.e Phase I (parallel pyridine orientation) and phase II (perpendicular pyridine orientation) were observed. A step height increase from 0.58 nm to

0.9 nm clearly demonstrated pyridine intercalation.

During deintercalation of pyridine, accumulation of pyridine molecules (at -0.44 V) as well as dissolution of islands (at 0.1 V) were clearly observed. In addition, nanocracks which formed during intercalation were also observed. A step height decrease from 0.9 nm to 0.6 nm in TaS₂ clearly demonstrated the deintercalation of pyridine.

Cu deposition onto TaS₂ :

Copper bulk deposition normally starts at a overpotential of -0.2 V followed by intercalation at -0.43 V observed in cyclic voltammetry.

Electrochemical copper deposition onto TaS₂ clearly demonstrated formation of similar nanostructures to those formed under vacuum conditions. Galvanostatic deposition (current density 0.5 mA·cm⁻²) for lower coverage (10 ML) did not show any nanotunnels except for nanoclusters. However increasing coverage to 25 ML and higher clearly demonstrated the formation nanotunnels whose height and width varies with increasing coverage.

Applying lower current density 0.4 mA·cm⁻² and 0.3 mA·cm⁻² resulted in the formation of large nuclei and clusters but no nanotunnels were observed.

Potentiostatic deposition at higher potential (-0.5 V) resulted in the formation of nanotunnels within minutes whereas at lower overpotentials (-0.35V) nanotunnels evolved only after 24 hours.

Postdeposition evolution of nanotunnels clearly indicated a intercalation driven mechanism of formation of nanotunnels where compressive stress due to copper deposition plays a minor role.

References

- [1] F. LEVY, *Intercalated layered materials*, D. Riedel Publishing Company, Holland (1979).
- [2] M. S. WHITTINGHAM and A. J. JACOBSON, *Intercalation Chemistry*, Academic Press inc. New York (1982).
- [3] O. M. MAGNUSSEN *J. Elec. Chem. Soc. (Interface)*, **15**, p23 (2006).
- [4] J. A. Wilson, F. J. DiSalvo and S. Mahajan, *Adv. Phys.*, **24**, 117 (1975).
- [5] J. A. Wilson, F. J. DiSalvo and S. Mahajan, *Phys. Rev. Lett.*, **32**, 882 (1974).
- [6] Y. Nishio, M. Shirai, N. Suzuki and K. Motizuki, *J. Phys. Soc. Jpn.*, **63**, 156 (1994).
- [7] K. Motizuki, Y. Nishio, M. Shirai and N. Suzuki, *J. Phys. Chem. Solids*, **57**, 1091(1996).
- [8] S.R. Cohen, Y. Feldman, H. Cohen and R. Tenne, *Appl. Surf. Sci.*, **145**, 603 (1999).
- [9] R. Tenne, L. Margulis and G. Hodes, *Advanced Materials*, **5**, 386 (1993).
- [10] H. Tributsch, *Z. Naturforsch.*, **32a**, 972 (1977).
- [11] G.A. Somorjai, *Introduction to Surface Chemistry and Catalysis*, John Wiley & Sons, Ltd, New York, 1994.
- [12] K. S. NOVOSELOV, *Science* **306**, 666 (2004).
- [13] M. INABA, Z. SIROMA, A. FUNABIKI and Z. OGUMI, *Langmuir* **12**, 1535 (1996).
- [14] F. P. CAMPANA, R. KOTZ, J. VETTER, P. NOVAK, and H. SIEGENTHALER, *Electrochem. Comm.*, **7**, p107 (2005).
- [15] D. ALLIATA, R. KÖTZ, O. HAAS, and H. SIEGENTHALER, *Langmuir* **15**, p8483 (1999).
- [16] R. Adlung, F. Ernst, A. Scott, M. T. Azar, M. Skibowski, S. Hollensteiner, E. Spiecker, W. Jäger, S. Gunst, A. Klein, V. Zaporojtchenko and F. Faupel, *Adv. Mat.* **14**, 1056 (2002).
- [17] R. Adlung, W. Hartung and F. Ernst, *Acta Mat.*, **50**, 4925 (2002).

- [18] R. Adlung, R. Kunz, F. Ernst, L. Kipp and M. Skibowski, *Adv. Solid State Phys.*, **43**, 463 (2003).
- [19] S. Hollensteiner, E. Spiecker, W. Jäger, R. Adlung, L. Kipp and M. Skibowski, *Materials Science and Engineering C*, **23**, 171 (2003).
- [20] R. Kunz, *Ph.D thesis*, University Kiel (2005).
- [21] S. Hollensteiner, E. Spiecker, W. Jäger, H. Haselier and H. Schröder, *Microscopy and Microanalysis*, **9**, 216 (2003).
- [22] J. WILSON and A. YOFFE, *Adv. Phys.*, **18**, p193 (1969).
- [23] F. R. GAMBLE, J. H. OSIECKI, M. CAIS, R. PISHARODY, F. J. DISALVO and T. H. GEBALLE, *Science*, **174**, p493 (1971).
- [24] R. E. THOMSON, B. BURK, A. ZETTKL and J. CLARKE, *Phys. Rev. B*, **49**, number 23, p16899 (1994).
- [25] M. B. WALKERS and R. L. WITHERS, *Phys. Rev. B*, **28**, p2766 (1983).
- [26] P. BERNUSSET, Y. JEANNIN, *Compt. Rend.*, **255**, p2973 (1962).
- [27] M. CHEVRETON, F. BERTAUT, *Compt. Rend.*, **255**, p1275 (1962).
- [28] S. BRUNIE, M. CHEVRETON, *C. R. Acad. Sci.*, **274**, p278 (1972).
- [29] T. SHIMADA, H. NISHIKAWA, A. KOMA, Y. FURUKAWA, E. ARAKAWA, K. TAKESHITA, T. MATSUSHITA, *Surf. Sc.*, **369**, p379 (1996).
- [30] M. BOEHME *Ph.D thesis*, University of Kiel (1998).
- [31] H. TAGAYA, T. HASHIMOTO, M. KARASU, T. IZUMI and C. CHIBA, *Chemistry Letters*, **2**, p2113 (1991).
- [32] W. M. R. DIVIGALPITIYA, R. F. FRINDT and S. R. MORRISON, *Science*, Vol., **246**, no4928, p369, (October 1989).
- [33] E. FIGUEROA, J. W. BRILL and J. P. SELEGUE, *Journal of Physics and Chemistry of Solids*, **57**, Number 6-8, p1123 (1996).

- [34] A. EGLINTON and W. MURPHY, *Organic Geochemistry*, Springer, Berlin : p737 (1969).
- [35] R. M. BARRER *Nanostoichiometric Compounds*, Academic Press, New York, p268 (1964).
- [36] G. R. HENNIG : *Nanostoichiometric Compounds, Prog. inorg. chem.*, **1**, p125 (1959).
- [37] F. R. GAMBLE and T. H. GEBALLE , *Treatise in Solid State Chemistry* Plenum, New York **3**, p268 (1976).
- [38] A. M. GHORAEB and R. H. FRIEND, *J. Phys. Condens. Matter*, **6**, p3533 (1994).
- [39] OLIVER RIEMENSCHNEIDER, *Phd thesis*, University Kiel (2004).
- [40] N. DAUMAS and A. HEROLD, *C.R. Acad. Sc.*, **268**, p373 (1969).
- [41] S. A. SAFRAN and D. R. HAMANN, *Phys. Rev. Lett.*, **42**, p1410 (1979).
- [42] S. A. SAFRAN and D. R. HAMANN, *Phys. Rev. B*, **23**, p565 (1981).
- [43] A. WEPPNER and R. A. HUGGINS, *J. Electrochem. Soc: Electrochem. Science and Technology*, **125**, number 1, p7 (1978).
- [44] A. WEPPNER and R. A. HUGGINS, *J. Electrochem. Soc : High Ion Oxide Conduction*, **124**, number 10, p1569 (1977).
- [45] A. WEPPNER and R. A. HUGGINS, *Z. Phys. Chem.: Neue Folge*, **108**, p105 (1977).
- [46] A. WEPPNER and R. A. HUGGINS, *Prog. Sympos. Electrode Materials and Processes for Energy Conversion and Storage*, Eds: J. D. E. McIntyre, S. Srinivasan, F. G. Will, Princeton, N. J., (1977).
- [47] A. R. BEAL and J. V. ACRIVOS, *Phil. Mag. B*, **37**, p409 (1978).
- [48] J. V. ACRIVOS and J. R. SALEM, *Philos. Mag.*, **30**, p603 (1974).
- [49] R. R. CHIANELLI, J. C. SCANLON and B. M. L. RAO, *Journal of Solid State Chemistry*, **29**, p323, (1979).
- [50] I. B. RASHKOV and I. GITSOV, *Journal of Polymer Science*, **24**, p155, (1986).

- [51] ANDREW C. CHU, JACK Y. JOSEFOWICZ and GREGORY C. FARRINGTON, *J. Electrochem. Soc.*, **144**, p4161 (1997).
- [52] M. FARADAY, *Phil. Trans. Roy. Soc.*, London, **124**, p77 (1834).
- [53] A. K. HUNTINGTON, *Trans. Faraday Soc.*, London, **1**, p324 (1905).
- [54] W. KOSSEL, *Nachr. Ges. Wiss. Göttingen, Math.-Phys. Kl.* 1927, 135: N. Stranski, *Z. Phys. Chem. (Leipzig)*, **136**, p269 (1928).
- [55] T. ERDEY-GRUZ and M. VOLMER, *Z. Phys. Chem. (Leipzig)*, **157**, p165 (1931).
- [56] KOHLSCHUTTER and TORICELLI, *Z. Elektrochem.*, **38**, p213 (1932).
- [57] H. FISCHER, *Electrolytic Separation and Electrolytic Crystallization of Metals*, Springer-Verlag, Berlin (1954).
- [58] D. SCHWARTZ, *The Electrochemical Society*, Interface (Spring 2006).
- [59] L. T. ROMANKIW, *Electrochim. Acta*, **42**, p2985 (1997).
- [60] M. SARIKAYA, C. TAMERLER, D. T. SCHWARTZ, and F. O. BANEYX, *Ann. Rev. Mater. Res.*, **34**, p373 (2004).
- [61] D. M. KOLB, R. ULLMANN, and T. WILL, *Science*, **275**, p1097 (1997).
- [62] J. D. WHITAKER, J. B. NELSON, and D. T. SCHWARTZ, *J. Micromech. Microeng.*, **15**, p1498 (2005).
- [63] M. SCHLESINGER and M. PAUNOVIC, *Modern Electroplating*, Wiley, New York (2000).
- [64] M. PAUNOVIC and M. SCHLESINGER *Fundamentals of Electrochemical Deposition*, Wiley, New York (1998).
- [65] D. M. KOLB, *Angew. Chem.*, **113**, p1198 (2001).
- [66] H. BRUNE, *Surface Science Reports (Netherland)*, **31**(4), p121 (1998).
- [67] K. KRUG, J. STETTNER and O. M. MAGNUSSEN, *Phys. Rev. Lett.*, **96**(24), p206101 (2006).

- [68] FREDRIK GOLKS, *Diploma thesis*, University of Kiel (2007).
- [69] JOHN VENABLES, *Introduction to Surface and Thin Film Processes*. Cambridge, Cambridge University Press (2000).
- [70] ALBERTO PIMPINELLI, *Physics of Crystal Growth*. Cambridge, Cambridge University Press (1998).
- [71] K. OURA, V. G. LIFSHITS, A. A. SARANIN, A. V. ZOTOV, and M. KATAYAMA *Surface Science: An Introduction.*, Berlin: Springer (2003).
- [72] J. E. B. RANGLES, *Trans. Faraday Soc.*, **48**, p828 (1952).
- [73] R. S. NICHOLSON and I. SHAIN, *Anal. Chem.*, **36**, p706 (1964).
- [74] R. S. NICHOLSON, *Anal. Chem.*, **37**, p1351 (1965).
- [75] DAVID K. GOSSER JR., *Cyclic Voltammetry*, VCH publishers, Inc. (1993).
- [76] G. V. SUBBA RAO and J. C. TSANG, *Mat. Res. Bull.*, **9**, p921 (1974).
- [77] K. ITAYA, *Prog. Surf. Sc.*, **58**, p121 (1998).
- [78] H. J. GÜNTHERODT and R. WIESENDANGER, *Topic by Siegenthaler p-7*, Springer Series in Surface Sciences (1992).
- [79] G. BINNIG, H. ROHRER and C. GERBER, *Phys. Rev. Lett.*, **56**, p930 (1986).
- [80] F. J. GIESSBL, *Materials Today*, **8**, Issue 5, p32 (2005).
- [81] O. MARTI, H. O. RIBI, B. DRAKE, T. R. ALBRECHT, C. F. QUATE and P. K. HANSMA, *Science*, **239**, p50 (1988).
- [82] G. FRIEDBACHER and M. GRASSERBAUER, *J. Anal. Chem.*, **346**, p58 (1993).
- [83] S. MORITA, *AFM measurement in liquid*, NanoScience and Technology, Springer Berlin Heidelberg, p101 (2007).
- [84] S. A. SAYED ASIF, K. J. WAHL and R. J. KOLTON, Materials Research Society Symposium Proceedings : Thin Films; Stresses and Mechanical Properties VIII, Nov. (1999).

- [85] G. M. McCLELLAND, R. ERLANDSSON, and C. CHIANG, *Rev. Prog. Quant. Nondestr. Eval.*, , p1307 (1987).
- [86] ANIL GANNEPALLI, *Ph.D thesis*, University of Iowa (2004).
- [87] M.KNOLL, *Z. Tech. Phys.*, **11**, p467 (1935).
- [88] J. I. GOLDSTEIN, *Scanning Electron Microscopy and X-Ray Microanalysis*, New York, Kluwer Academic / Plenum Publishers (2003).
- [89] M. OATLY, *Scanning Electron Microscopy*, Cambridge University Press (1972).
- [90] L. E. CONROY and K. R. PISHARODY, *J. Sol. Stat. Chem.*, **4**, p345 (1972).
- [91] W. YAMAGUCHI, O. SHINO , H. H. SUGAWARA, T. HASEGAWA and K..KITAZAWA, *Appl. Surf. Sci.*, **119**, p67 (1997).
- [92] Y. KIM, J. L. HUANG and C. M. LIEBER, *Appl. Phys. Lett.*, **59**, Number 26, p3404 (1991).
- [93] M. S. WHITTINGHAM, *J.C.S Chem. Comm.*, p328 (1974).
- [94] D. W. MURPHY, F. J. DI SALVO, G. W. HALL JR. and J. V. WASZCZAK, *J. Chem. Phys.*, **62**, number 3, p967 (1975).
- [95] C. RIEKEL, H. G. REZNIK, R. SCHÖLLHORN and C. J .WRIGHT, *J. Chem. Phys.*, **70**, number 11, p5203 (1979).
- [96] R. SCHÖLLHORN, *Physica*, **99B**, p89 (1980).
- [97] R. SCHÖLLHORN, H. D. ZAGEFKA, T. BUTZ and A. LERF, *Mat. Res. Bull.*, **14**, p369 (1979).
- [98] F. R. GAMBLE, J. M. OSIECKI and F. J. DI SALVO, *J.Chem. Phys.*, **55**, p3525 (1971).
- [99] Z. WAQAR, A. DESINOV, T. N. KOMPANIETS, I. V. MAKARENO, A. N. TITKOV, *Physica Scripta.*, **T94**, p132 (2001).
- [100] Y. A. HONG, J. R. HAHN and H. KANG, *J. Chem. Phys.*, **108**, Number 11, p4367 (1998).

- [101] A. WEISS and R. RUTHARD, *Z. Natur Forschung* , **B28**, p249 (1973).
- [102] A. WEISS and R. RUTHARD, *Z. Natur Forschung* , **B28**, p522 (1973).
- [103] A. WEISS, E. SICK and R. SCHÖLLHORN, *Z. Natur Forschung* , **B28**, p168 (1973).
- [104] F. WYPYCH, M. A. B. GOMES, I. DENICOLO and L. B. ADAD, *J. Electrochem. Soc.* **143**, 2522 (1996).
- [105] E. D. BRANDNER, A. MUNIER, J. M. ZHU, B. A. AVERILL and B. S. SHIVARAM, *J. Mat. Sc.*, **33**, Number 7, p1949 (1998).
- [106] A. WEISS, R. SCHÖLLHORN and E. SICK, *Z. Naturforsch. B*, **28**, p168 (1973).
- [107] T. OHMORI and R. J. CASTRO and C. R. CABRERA, *Langmuir* , **14**, p6755 (1998).
- [108] B. PARKINSON, *J. Am. Chem. Soc.*, **112**, p7498 (1990).
- [109] C. ENSS, R. WINTERS, M. REINERMANN, G. WEISS, S. HUNKLINGER and M. LUX-STEINER, *Z. Phys. B*, **99**, p561 (1996).
- [110] J. W. JOHNSON, *Physica B+C (Amsterdam)*, **99**, p141 (1980).
- [111] A. H. THOMPSON, *Nature (London)*, **251**, p492 (1974).
- [112] R. SCHÖLLHORN and A. WEISS, *Z. Natur Forschung*, **27b**, p1277 (1972).
- [113] S. F. MEYER, R. E. HOWARD, G. R. STEWART and T. H. GEBALLE, *J. Chem. Phys.*, **62**, p4411 (1975).
- [114] F. R. GAMBLE, J. H. OSEICKI and F. J. DI SALVO, *J. Chem. Phys.*, **55**, p3525 (1975).
- [115] T. K. KIM, V. P. BABENKO, B. N. NOVGORODOV, D. I. KOCHUBEY and SH. K. SHAIKHUTDINOV, *Nucl. Inst. Meth. in Phys. Res. Sec. A*, **405**, Issue 2-3, p348 (1998).
- [116] H. F. MORAN, M. OHSTUKI, M. CAIS, A. HIBINO and C. HOUGH, *Science*, **174**, p498 (1971).
- [117] J. M. THOMAS, E. L. EVANS, B. BACH and J. W. JENKINS, *Nature (London), Phys. Sci.*, **235**, p126 (1972).
- [118] S. WADA, H. ALLOUL and P. MOLINIE, *J. Phys. Lett.*, **39**, pL243 (1978).

- [119] C. RIEKEL and C. O. FISCHER, *J. Sol. Stat. Chem.*, **29**, p181 (1979).
- [120] E. EHRENFREUND, A. C. GOSSARD and F. R. GAMBLE, *Phy. Rev. B*, **5**, p1708 (1972).
- [121] B. C. TOFIELD and C. J. WRIGHT, *Solid State Commun.*, **22**, p715 (1977).
- [122] G. SCHOLZ, P. JOENSEN, J. M. REYES and R. F. FRINDT, *Physica B*, **105**, p225 (1981).
- [123] A. R. BEAL and J. V. ACRIVOS, *Phil. Mag. B*, **37**, p409 (1978).
- [124] T. OHMORI, R. J. CASTRO and C. R. CABRERA, *Langmuir*, **14**, p6287 (1998).
- [125] H. D. ZAGEFKA: *Ph.D Thesis, University of Münster*, (1980).
- [126] R. SCHÖLLHORN, *Pure and Appl. Chem.*, **56**, p1379 (1984).
- [127] S. SHUSHI, O. HIROSHI, F. KEN-ICHI and I. YASUHIRO, *Chem. Phys. Lett.*, **304**, Issues 3-4, p225 (1999).
- [128] R. ADELUNG, L. KIPP, J. BRANDT, L. TARCAK, M. TRAVING, C. KREIS and M. SKIBOWSKI, *Appl. Phys. Lett.*, **74**, p3053 (1999).
- [129] R. ADELUNG, J. BRANDT, K. ROSSNAGEL, O. SEIFARTH, L. KIPP, M. SKIBOWSKI, C. RAMIREZ, T. STRASSER and W. SCHATTKER, *Phys. Rev. Lett.*, **86**, p1303 (2001).
- [130] S. L. SULB, L. R. FAULKNER and G. D. STUCKY, *Anal. Chem.*, **51**, p1060 (1979).
- [131] C. RAMIREZ and W. SCHATTKER, *Surf. Sci.*, **482**, p424 (2001).
- [132] E. SPIECKER, A. K. SCHIMD, A. M. MINOR, U. DAHMEN, S. HOLLENSTEINER and W. JÄGER, *Phys. Rev. Lett.*, **96**, p086401 (2006).
- [133] F. J. Di Salvo, G. W. Hull jr., L. H. Schwartz, J. M. Voorhoeve and J. V. Waszczak, *J. Chem. Phys.*, **59**, p1922 (1973).
- [134] W. HAISS, R. J. NICHOLS and J. K. SASS, *Surf. Sci.*, **388**, p141 (1997).
- [135] O. E. KONGSTEIN, U. BERTOCCHI and G. D. STUCKY, *J. Electrochem. Soc.*, **152**, c116 (2005).

- [136] Y. ZHOU, C. S. YANG, J. CHEN, G. DING, W. DING, L. WANG, M. WANG, Y. ZHANG and T. ZHANG *Thin solid films*, **460**, p175 (2004).
- [137] R. KOCH *J. Phys. Conden. Matter*, **6**, p9519 (1994).

Curriculum Vitae

Personal details

Name : Sujit Kumar Dora
Date of birth : 28.05.1977
Place of birth : Athgarh, India
Marital Status : Single
Private Address : Hindenburgufer 81, 24105 Kiel

Education

1993 : School degree (B. N. Bidyapitha), Orissa, India.
1994-1997 : Bachelor in Chemistry, Utkal University, India.
1998-2000 : Master in Chemistry, Utkal University, India.
2002-present : Ph.D at the University of Kiel, Institut für Experimentelle und Angewandte physik. *Thesis title : Study of In-Situ Intercalation of Organic Molecules and Electrodeposition of Cu into Transition Metal Chalcogenides by Scanning Probe techniques.*

Research Experience

Project fellow 2001-2002 : IIT Bombay, India. *Project title : Preparation of 'Ti' nano particles by chemical method.*

Publications

1. 'In situ electrode processes of 1T-TaS₂ in pyridine and octylamine electrolytes': Sujit K. Dora, and O. M. Magnussen, *J. Electrochem. Soc.*, **155**, F132 (2008).
2. 'Nanotunnel formation During Cu Electrodeposition on TaS₂': Sujit K. Dora, X. Bai, Mady Elbahri, R. Adelung and O. M. Magnussen, *J. Electrochem. Soc.*, **155**(10), D666-D670 (2008) .

Eidesstattliche Erklärung

Hiermit erkläre ich an Eides Statt, da ich diese Arbeit selbständig unter der Beratung meiner wissenschaftlichen Lehrer und nur mit den angegebenen Hilfsmitteln erstellt habe. Diese Arbeit wurde weder ganz noch in Teilen an anderer Stelle im Rahmen eines Prüfungsverfahrens vorgelegt. Frühere Promotionsversuche wurden von mir nicht vorgenommen.

Kiel, den

.....

Sujit kumar Dora

Acknowledgments

My foremost thank goes to my thesis adviser Prof. Dr. Olaf Magnussen. Without him, this dissertation would not have been possible. I thank him for his patience and encouragement that carried me on through difficult times, and for his insights and suggestions that helped to shape my research skills. His valuable feedback contributed greatly to this dissertation.

I would also like to thank Dr. Rainer Adelung and his group specially Mady Elbahri in Materials Science department for the fruitful discussion and help in carrying out my experiments.

I thank all my colleagues and staffs in physics department, whose presences and fun-loving spirits made the otherwise grueling experience tolerable. They are: Mr. Yinxiang Bai, Dr. Koji Suto, Christian Haak, Belinda Baisch, Tunay Tansel, Ulrich Jung, Daniel Kaminski, Klaus Krug, Hisayoshi Matshushima, Frederik Golks, Andriy Taranovskyy, Yaiza G. Gonazalez, Annika Elsen, Dr. Bridget Murphy. Diego Raffa, Mr. Arnd Seeger, Mrs. Monica Seeger, Mrs Rosamerie Müller Puffe, Matthias Greve and Dr. Jochim Stettner. I enjoyed all the vivid discussions we had on various topics and had lots of fun being a member of this fantastic group.

Special thanks to the people in mechanical workshop for preparing those nicely designed electrochemical cells for experiments.

Last but not least, I thank my parents and my sisters for always being there when I needed them most, and for supporting me through all these years.